Received 17 June 2025; accepted 20 July 2025. Date of publication 23 July 2025; date of current version 23 September 2025.

Digital Object Identifier 10.1109/OJCOMS.2025.3591836

Sub-THz Communications: Perspective and Results From the Hexa-X-II Project

ITALO ATZENI [1] (Senior Member, IEEE), GUSTAVO RODRIGUES DE LIMA TEJERINA [1], RAFAEL BERKVENS [2], HUI CHEN [3] (Member, IEEE), JEAN-MARC CONRAT [4], MAR FRANCIS DE GUZMAN [5] (Graduate Student Member, IEEE), CLAUDE DESSET [2] (Member, IEEE), MEIK DÖRPINGHAUS [6] (Member, IEEE), HAMED FARHADI [7], GERHARD FETTWEIS [6] (Fellow, IEEE), FLORIAN GAST [6] (Graduate Student Member, IEEE), HARDY HALBAUER [8] (Associate Member, IEEE), RREZE HALILI [2], KATSUYUKI HANEDA [5] (Member, IEEE), ILKKA HARJULA [9], BRUNO JAHAN [4], RAMIN KHAYATZADEH [10], PEKKA KYÖSTI [1], RODOLPHE LEGOUABLE [4], ARTO LEHTI [11], DILEEPA MARASINGHE [1] (Graduate Student Member, IEEE), LE HANG NGUYEN [8] (Member, IEEE), SHARIEF SALEH [3] (Member, IEEE), KAAN SENPARLAK [10], NUUTTI TERVO [1] (Member, IEEE), OSKARI TERVO [9], HENK WYMEERSCH [3] (Fellow, IEEE), BO XU [7] (Member, IEEE), AND PEIZE ZHANG [1] (Member, IEEE)

[1]Centre for Wireless Communications, University of Oulu, 90014 Oulu, Finland
[2]Imec, 3001 Leuven, Belgium
[3]Department of Electrical Engineering, Chalmers University of Technology, 412 96 Gothenburg, Sweden
[4]Orange Innovation, 92320 Châtillon, France
[5]School of Electrical Engineering, Aalto University, 00076 Espoo, Finland
[6]Vodafone Chair Mobile Communications Systems, Technical University of Dresden, 01062 Dresden, Germany
[7]Ericsson, 164 83 Stockholm, Sweden
[8]Nokia Bell Labs, 70469 Stuttgart, Germany
[9]Nokia, 90590 Oulu, Finland
[10]Apple, 80335 Munich, Germany
[11]Nokia, 91620 Nozay, France

CORRESPONDING AUTHOR: I. ATZENI (e-mail: italo.atzeni@ieee.org)

This work was supported by the Hexa-X-II Project, which has received funding from the Smart Networks and Services Joint Undertaking (SNS JU) through the European Union's Horizon Europe Research and Innovation Programme under Grant 101095759.

ABSTRACT Sub-THz communications are envisioned to unlock ultra-high data rates, ultra-low latencies, and massive connectivity in future wireless systems by utilizing bandwidths of up to tens of GHz. This paper presents the holistic perspective on sub-THz communications developed within the European sixth-generation (6G) flagship project *Hexa-X-II*. According to this perspective, successfully deploying sub-THz systems will require addressing several physical-layer (PHY) challenges associated with the harsh signal propagation and hardware limitations. In addition, sub-THz systems will drive advancements in essential wireless applications beyond communications, such as joint communications and sensing (JCAS). In this context, we present a collection of technical contributions and key findings from the Hexa-X-II project that have shaped this perspective. In contrast to existing works, these efforts collectively tackle the fundamental PHY challenges of sub-THz communications, i.e., understanding and modeling of radio propagation, radio-frequency (RF) power consumption and complexity, and hardware impairments. To achieve this, we present several results across three core areas, i.e., signal propagation and channel modeling, RF transceiver design, and PHY enablers, offering useful insights into the development of sub-THz systems. Lastly, we provide an overview of sub-THz JCAS, emphasizing it as one of the most promising applications in the sub-THz range.

INDEX TERMS Sub-THz communications, 6G, sub-THz channel modeling, sub-THz RF transceiver design, sub-THz PHY enablers, sub-THz JCAS.

I. INTRODUCTION

FIFTH-GENERATION (5G) wireless systems currently operate in the sub-6 GHz band, referred to in Third-Generation Partnership Project (3GPP) as FR1 and extending up to 7.125 GHz [1], as well as in the low millimeter-wave (mmWave) band, referred to in 3GPP as

FR2 and ranging from 24.25 to 71 GHz [2]. Future 5G releases are expected to cover the upper mid-band, referred to in 3GPP as FR3 and spanning the 7.125–24.25 GHz range [3]. FR3 provides an appealing trade-off between coverage and bandwidth, and features milder propagation conditions than FR2. However, future wireless applications such as autonomous systems, extended reality, massive Internet of Things (IoT), high-capacity fronthaul/backhaul, and wireless sensing/imaging will demand unprecedented bandwidths that neither FR3 nor FR2 can provide [4], [5]. This motivates exploring the sub-THz range between 100 and 300 GHz.

Sub-THz communications are envisioned to enable ultra-high data rates, ultra-low latencies, and massive connectivity in future wireless systems [4], [6]. Sub-THz communications have attracted a great deal of research attention during the past few years, with early optimism surrounding their potential to be a cornerstone of the initial rollout of sixth-generation (6G) wireless systems [7]. However, as the research progressed, it became clear that the practical deployment of sub-THz systems is far more complex than initially anticipated due to factors such as the harsh signal propagation and hardware limitations. Consequently, it is now recognized that sub-THz communications will likely be introduced in the long-term evolution of 6G rather than in its initial implementation. This shift in expectations has not discouraged research in the field or diminished its significance; instead, it has served as an even greater incentive to continue advancing research and innovation in overcoming these hurdles, ultimately realizing the promise of sub-THz frequencies in future wireless technologies.

Sub-THz systems will offer vast bandwidths of up to tens of GHz, which have the potential to unlock data rates up to 1 Tbps and latencies as low as 100 μs [4]. However, these large bandwidths come at the cost of more challenging signal propagation, higher radio-frequency (RF) power consumption and complexity, and more significant hardware impairments. On the one hand, the free-space path loss (for isotropic antennas) increases proportionally to the square of the wavelength, requiring large antenna arrays to properly focusing the signal power. Additionally, propagation phenomena such as scattering, diffraction, and reflection behave differently than at lower frequencies. In this regard, the penetration loss and roughness of the materials with respect to the wavelength grow, which generally diminishes the impact of the non-line-of-sight (NLoS) paths. On the other hand, as the bandwidth (and thus the sampling frequency) as well as the carrier frequency increase, RF components typically become more power-hungry and complex, while also suffering more from impairments. For example, the power consumption of the analog-to-digital converters (ADCs) increases quadratically with the bandwidth above 330 MHz, impacting the energy efficiency and heat dissipation. Large bandwidths also cause detrimental hardware impairments such as distortion in the power amplifiers (PAs), high noise level in the low-noise amplifiers (LNAs) and local oscillators (LOs), and phase noise (PN). At the same time, implementing the components with circuit technologies that are suitable for mass production is of utmost importance in order to enable commercially feasible systems. These issues are exacerbated by the need for a large number of RF components due to the increased number of antennas required. Furthermore, while the small wavelength allows packing many antenna elements with sub-wavelength spacing into a very small area, the associated RF hardware cannot be miniaturized accordingly, calling for solutions with a high integration rate. All these factors interact in complex ways, influencing the overall system's design and performance.

In December 2023, the International Telecommunication Union (ITU) World Radiocommunication Conference addressed the sub-THz spectrum through several key resolutions [8]. For instance, ITU has recognized specific frequency bands within the 102–275 GHz range as suitable for cellular communications, marking a crucial first step toward International Mobile Telecommunications standardization. Furthermore, ITU has proposed additional allocations for sensing and imaging services in the 231.5–700 GHz range. These resolutions highlight the growing interest in standardizing sub-THz frequencies for communication and sensing in future wireless systems.

A. LITERATURE REVIEW

In recent years, numerous studies have explored sub-THz communications, especially in the context of 6G. However, most of these works address specific topics or applications rather than providing a holistic perspective on sub-THz systems. To illustrate this trend, we narrowed down 33 publications among surveys, tutorials, and magazine papers on sub-THz and THz communications issued between 2020 and 2025 [9], [10], [11], [12], [13], [14], [15], [16], [17], [18], [19], [20], [21], [22], [23], [24], [25], [26], [27], [28], [29], [30], [31], [32], [33], [34], [35], [36], [37], [38], [39], [40], [41]. These publications address various aspects of sub-THz systems, which we categorize into four key topics: i) channel modeling, ii) RF design, iii) physical-layer (PHY) enablers, and iv) 6G applications. Table 1 lists the selected publications, where each topic is further assessed at three levels: not mentioned (blank space), briefly mentioned (○), and discussed in detail (●).

i) Channel modeling is the first recurrent topic in the literature of sub-THz communications. The peculiarities arising in the sub-THz band call for a thorough investigation of the channel and propagation characteristics. For instance, [14] surveyed a sub-THz channel model considering molecular absorption loss, multipath fading, misalignment, and hardware impairments. References [21] and [22] provided an in-depth survey on recent measurement campaigns, propagation characteristics, and modeling techniques, relating them to 6G applications and scenarios. Reference [37] provided a historical overview of sub-THz measurements,

TABLE 1. Summary of the literature review. The publications are categorized by topic (channel modeling, RF design, PHY enablers, and 6G applications) in three levels: not mentioned (blank space), briefly mentioned (○), and discussed in detail (●).

Ref.	Year	Title	Key topics			
			Channel modeling	RF design	PHY enablers	6G applications
[9]	2020	THz radio communication: Link budget analysis toward 6G	○	●		●
[10]	2020	IEEE 802.15.3d: First standardization efforts for sub-terahertz band communications toward 6G			●	●
[11]	2020	Ultramassive MIMO systems at terahertz bands: Prospects and challenges	●	●	●	○
[12]	2020	Experimental demonstrations of high-capacity THz-wireless transmission systems for beyond 5G		●		●
[13]	2021	Key technologies in 6G terahertz wireless communications systems: A survey	●	●	●	○
[14]	2021	THz channel modeling: Consolidating the road to THz communications	●	○		○
[15]	2021	Terahertz wireless communications for 2030 and beyond: A cutting-edge frontier		○	●	●
[16]	2021	Fundamental limits of high-efficiency silicon and compound semiconductor power amplifiers in 100-300 GHz bands		●	●	
[17]	2021	An overview of signal processing techniques for terahertz communications	●	●	●	●
[18]	2021	Machine learning: A catalyst for THz wireless networks			●	○
[19]	2022	A biomedical perspective in terahertz nano-communications – A review	●	●		●
[20]	2022	Terahertz communications: Challenges in the next decade		●	●	
[21]	2022	Terahertz channel propagation phenomena, measurement techniques and modeling for 6G wireless communication applications: A survey, open challenges and future research directions	●		○	●
[22]	2022	Terahertz wireless channels: A holistic survey on measurement, modeling, and analysis	●		○	●
[23]	2022	A tutorial on terahertz-band localization for 6G communication systems	●	●	○	●
[24]	2021	Signal processing and machine learning techniques for terahertz sensing: An overview			○	●
[25]	2022	Seven defining features of terahertz (THz) wireless systems: A fellowship of communication and sensing	●		●	●
[26]	2022	THz-empowered UAVs in 6G: Opportunities, challenges, and trade-offs	●	○	○	●
[27]	2022	Terahertz band communication: An old problem revisited and research directions for the next decade	●	●	●	○
[28]	2023	THz-enabled UAV communications: Motivations, results, applications, challenges, and future considerations	○	○	●	●
[29]	2023	THz systems exploiting photonics and communications technologies		○	●	●
[30]	2023	From terahertz imaging to terahertz wireless communications	●	●		●
[31]	2023	Machine learning for millimeter wave and terahertz beam management: A survey and open challenges			●	○
[32]	2023	Terahertz meets AI: The state of the art			●	
[33]	2023	Hardware aspects of sub-THz antennas and reconfigurable intelligent surfaces for 6G communications		●	●	○
[34]	2023	THz communications: A key enabler for future cellular networks	●	●	●	○
[35]	2023	Terahertz communications for 6G and beyond wireless networks: Challenges, key advancements, and opportunities		●	●	○
[36]	2023	Spectrum options and allocations for 6G: A regulatory and standardization review				●
[37]	2023	THz measurements, antennas, and simulations: From the past to the future	●	●		○
[38]	2024	Terahertz communications and sensing for 6G and beyond: A comprehensive view	●	●	●	●
[39]	2024	The evolution of applications, hardware design, and channel modeling for terahertz (THz) band communications and sensing: Ready for 6G?	●	●	●	●
[40]	2024	Technical advancements toward RIS-assisted NTN-based THz communication for 6G and beyond	○		●	●
[41]	2025	A survey on advancements in THz technology for 6G: Systems, circuits, antennas, and experiments	●	●	○	●
–	2025	**This paper**	●	●	●	●

antennas, and simulations, highlighting recent results in indoor and outdoor channel modeling, chip design, and ray-tracing simulations. More recently, [39] reviewed the latest studies in the field of THz communications, focusing on mobility use cases, transceiver and antenna design, and scenario-oriented channel modeling.

ii) Sub-THz RF design generally addresses chip design, RF components, and transceiver architectures. Increasing the carrier frequency to sub-THz levels adds a huge toll to RF design. In this setting, the complexity and power consumption of RF components raises considerably, impacting circuit integration, PAs, and LNAs, just to name a few. In this regard, [9] evaluated the link budget of a sub-THz system to support extremely high rates considering hardware constraints such as noise figure (NF), transmit power, and antenna gain. Reference [12] explored the concept of wireless fiber extender with sub-THz RF front ends designed for long-range transmissions. Reference [16] reviewed the requirements and circuit design of power amplifiers in terms of energy efficiency for massive multiple-input multiple-output (MIMO) systems operating in the sub-THz band. Reference [20] surveyed existing chip designs and discussed the challenges to achieve Tbps rates and to deploy beamforming transceivers. Reference [33] reviewed antenna and reflective surface technologies to identify promising approaches for commercial sub-THz deployments. Lastly, [41] surveyed the state of the art of circuit, antenna, and transceiver design, focusing on practical solutions for commercial 6G systems.

iii) Sub-THz PHY enablers broadly include massive MIMO and its variants, reconfigurable intelligent surfaces (RISs), beamforming, waveforms, modulations, coding schemes, and related optimization. Reference [10] detailed the specifications of modulation and coding scheme of the IEEE 802.15.3d standard to improve data rates for consumer wireless sub-THz systems. Reference [11] focused on ultra-massive MIMO architectures, linking to recent advancements in transceiver design, channel modeling, waveforms, and spatial modulations. Reference [15] investigated joint communications and sensing (JCAS) applications and promising concepts such as dynamic hybrid beamforming, ultra-massive MIMO, RISs, and machine learning (ML) paradigms to enable higher data rates and spectral efficiency of sub-THz systems. Reference [17] overviewed THz-specific signal processing techniques focusing on MIMO, RISs, waveform design and modulation, beamforming and precoding, channel estimation, channel coding, and data detection. Reference [18] explored the potential and limitations of ML-based

methods to address key challenges across PHY and higher layers of THz wireless systems. Reference [25] defined key features of sub-THz systems such as cell-free massive MIMO and the use of artificial intelligence to predict channel state information and optimize network functions, as well as use cases such as extended reality and digital twins. Reference [31] provided an in-depth review of ML-based solutions for beam management in mmWave and sub-THz systems. Lastly, [32] provided a comprehensive survey of the use of artificial intelligence across PHY and higher layers, also reviewing existing THz testbeds and simulators.

iv) 6G applications enabled by sub-THz systems include extended reality, wireless sensing/imaging, and unmanned aerial vehicles (UAVs), also covering healthcare and biomedical fields. For instance, [19] surveyed channel models and RF design applied specifically to nano-scale devices to enable in vivo molecular communication. Reference [30] investigated sub-THz imaging and the possibility to integrate it to wireless systems. Reference [23] detailed system modeling, performance analysis, and optimization formulations to address localization in the sub-THz band. Reference [24] reviewed signal processing techniques for THz JCAS, covering preprocessing, feature extraction, and classification methods while analyzing their performance-complexity trade-offs. References [26] and [28] investigated UAV-empowered sub-THz systems to enable reliable connectivity, sensing, localization, and monitoring. Reference [29] highlighted advancements in high-resolution spectroscopy and imaging, as well as the potential of THz frequencies in the contexts of wireless communications and indoor localization. Reference [36] surveyed spectrum management techniques for high-frequency bands and discussed the need for re-evaluating the regulation and standardization policies to attend the unique requirements of 6G. Reference [38] presented a comprehensive survey of THz communications discussing channel modeling, RF design, PHY enablers (e.g., antennas and beamforming), and sensing applications. Lastly, [40] reviewed recent advancements in RIS-aided communications emphasizing their potential for 6G non-terrestrial networks.

While these works collectively offer a broad overview of all the key topics, they do not provide a holistic perspective that integrates sub-THz system challenges and detailed technical solutions.

B. CONTRIBUTION

The sub-THz spectrum is highly significant for the long-term evolution of 6G and future wireless generations. Consequently, it continues to be a crucial area of research for both industry and academia. This paper presents the holistic perspective on sub-THz communications developed within the European 6G flagship project *Hexa-X-II* (2023–2025), which brings together leading industrial stakeholders and universities. While existing works mostly focus on isolated technical aspects or provide broad high-level overviews of sub-THz communications, this paper bridges the gap by combining a structured overview of key challenges and enablers, representative technical results from the project, and an integrative perspective that highlights open research directions and system-level challenges. The overview component is not intended to be exhaustive; rather, its purpose is to frame the technical contributions within the broader sub-THz research landscape and highlight the specific challenges that drive ongoing and future investigations.

According to our perspective, summarized in Figure 1, achieving successful sub-THz deployments will require overcoming a series of PHY challenges related to the harsh signal propagation and hardware limitations. Moreover, sub-THz systems will drive advancements in essential wireless applications beyond communications, such as JCAS. In this context, we present a collection of technical contributions and key findings from the Hexa-X-II project that have shaped this perspective. Unlike existing works, these efforts collectively tackle the fundamental PHY challenges of sub-THz communications: i) understanding and modeling of radio propagation, ii) RF power consumption and complexity, and iii) hardware impairments. To this end, we present several results across three core areas: i) signal propagation and channel modeling, ii) RF transceiver design, and iii) PHY enablers, offering valuable insights into the development of sub-THz systems. Lastly, we present an overview of sub-THz JCAS, highlighting it as one of the most promising applications in the sub-THz range.

Our results indicate that sub-THz channel measurements and modeling should be tailored to suit the specific characteristics of each use case and deployment scenario. Furthermore, heterogeneous integration, which combines multiple integrated circuit technologies within the same package, can strike a promising techno-economical balance for addressing RF power consumption and hardware impairments in sub-THz RF transceiver design. Regarding the PHY enablers, both evolutionary and revolutionary waveforms and modulations can be effective at sub-THz frequencies, whereas low-complexity massive MIMO and energy-efficient network deployments are needed to reduce RF power consumption, complexity, and cost. In addition, ML-based techniques hold significant potential for mitigating sub-THz hardware impairments. Lastly, leveraging sub-THz frequencies in JCAS enables both high-precision sensing and high-quality communications, which can further benefit from capitalizing on near-field and beam squint effects.

The structure of the paper is outlined in Figure 2 and its contributions are summarized as follows.

- In Section II, we present the main PHY *challenges arising at sub-THz frequencies*, i.e., understanding and modeling of radio propagation, RF power consumption and complexity, and hardware impairments, linking

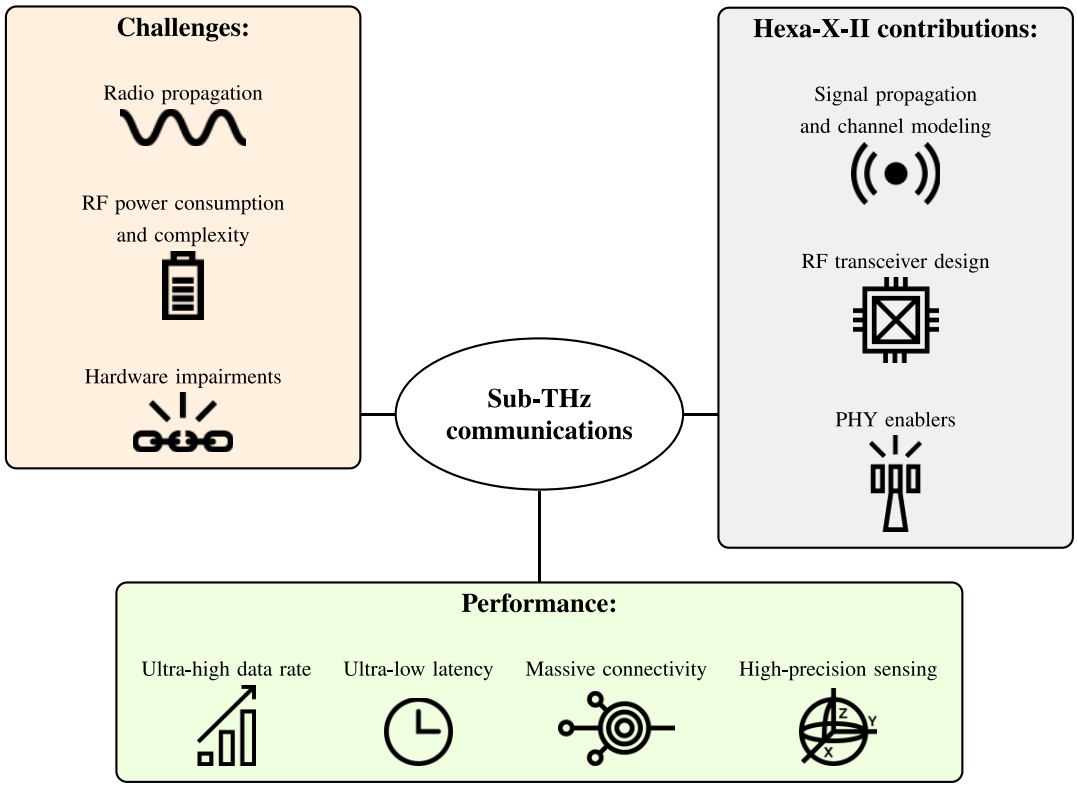

FIGURE 1. Perspective on sub-THz communications developed within the Hexa-X-II project.

these challenges to our contributions in the following sections.

- In Section III, we provide an extensive analysis of sub-THz *signal propagation and channel modeling*. First, we present the state-of-the-art channel sounders used to collect site-specific and cellular-type data across different sub-THz bands. Using the site-specific data, we characterize the signal reflection over rough surfaces and patterned glass, and also analyze the effects of diffraction and blockage caused by human body and small objects. Furthermore, we detail the setting of the measurement campaigns (e.g., environments, frequencies, and number of links) performed to obtain the cellular-type data, which is used to propose a sub-THz stored channel model. Then, we present a ray-tracing simulator for modeling sub-THz propagation and reflection. Moreover, we propose a refined 3GPP-like stochastic channel model that considers random cluster angular offset. Lastly, we discuss a generalized stochastic channel model, namely the κ-μ model, applied to sub-THz massive MIMO systems.
- In Section IV, we address sub-THz *RF transceiver design* focusing on the energy efficiency of MIMO architectures and RF electromagnetic field (EMF) exposure. We provide a review of the expected performance of four circuit technologies, namely complementary metal-oxide-semiconductor (CMOS), silicon-germanium (SiGe), gallium nitride (GaN), gallium arsenide (GaAs), and indium phosphide (InP), and examine the achievable output power and NF of the resulting PAs and LNAs, respectively. Then, we analyze three MIMO architectures, i.e., fully digital, hybrid partially connected, and hybrid fully connected, and optimize the energy efficiency in terms of the number of antennas, output power, and modulation. We show that a meticulous optimization over these parameters improves the energy efficiency by a factor of 10. Lastly, we discuss the requirements and implications of RF EMF exposure of sub-THz base station (BS) and user equipment (UE) based on the International Commission on Non-Ionizing Radiation Protection (ICNIRP) guidelines [42].
- In Section V, we address different sub-THz *PHY enablers*, namely waveforms and modulations, massive MIMO architectures, ML-based demapping, and energy-efficient network deployments. Regarding waveforms and modulations, we discuss the changes needed in the 5G New Radio (NR) numerology to support operations at sub-THz frequencies. In this regard, we show that increasing the subcarrier spacing (SCS) mitigates the PN, whereas using discrete Fourier transform-spread-orthogonal frequency-division multiplexing (DFT-s-OFDM) improves the coverage. Furthermore, we present a single-carrier (SC) waveform to mitigate the PN and PA inefficiencies by incorporating peak-to-average power ratio (PAPR) constraints into its geometric constellation shaping. Then, we analyze zero-crossing modulation (ZXM) applied to

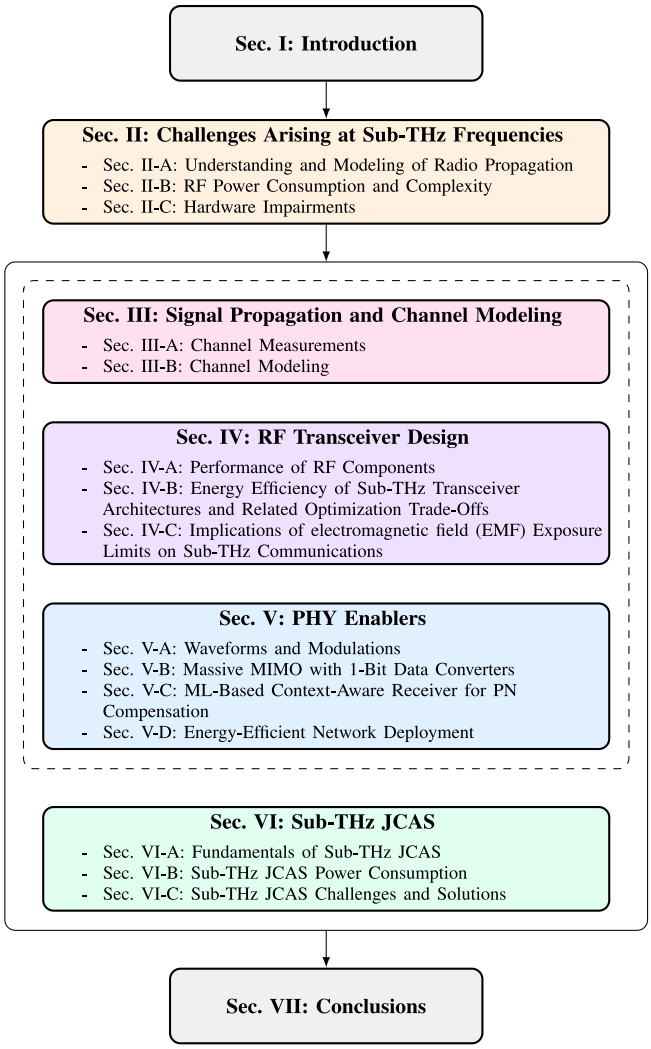

FIGURE 2. Outline of the paper.

1-bit ADC receivers, which is shown to achieve higher energy efficiency compared with quadrature amplitude modulation (QAM) across most data rate requirements. Additionally, we propose a new modulation scheme, referred to as polar constellation (PC), that is more robust to phase rotation induced by the Doppler shift than classical QAM. Regarding massive MIMO architectures, we consider the extreme scenario where both the transmitter and receiver are equipped with fully digital massive MIMO arrays and 1-bit ADCs/digital-to-analog converters (DACs), which minimizes the RF cost, power consumption, and complexity. Moreover, we discuss PN compensation using ML-based context-aware receivers for DFT-s-OFDM transmissions. Lastly, we provide an outlook on energy efficiency, BS beamforming architecture, and network deployment to achieve target throughput and coverage.

- In Section VI, we explore the concept of *sub-THz JCAS*. JCAS is envisioned as a key technology for 6G networks, and extensions to the sub-THz range are expected to further enhance its potential. We discuss the convergence of communication and sensing, the benefits and integration levels of JCAS, and the unique features of sub-THz frequencies. The geometric and channel models essential for sub-THz JCAS are established, along with the challenges posed by hardware limitations and signal attenuation, and potential solutions are presented. Additionally, the future outlook for JCAS is highlighted, with an emphasis on advancements in channel modeling, estimation algorithms, and optimization strategies.
- In Section VII, we highlight additional topics beyond the scope of this work and summarize our contribution, providing some key insights into the development of sub-THz systems. The acronyms used throughout the paper are listed after Section VII.

II. CHALLENGES ARISING AT SUB-THZ FREQUENCIES

In this section, we describe the main PHY challenges that arise at sub-THz frequencies: i) understanding and modeling of radio propagation, ii) RF power consumption and complexity, and iii) hardware impairments. Then, we link these three challenges with our contributions in Sections III–V. The links between the challenges and contributions are summarized in Table 2.

A. UNDERSTANDING AND MODELING OF RADIO PROPAGATION

Wireless channels are the core of sub-THz communication systems. Understanding their properties is essential to properly assess the potential and limitations of sub-THz systems, and also to provide guidelines for optimal system design. While radio propagation is well understood at sub-6 GHz and 5G mmWave frequencies [43], [44], our knowledge remains limited in the sub-THz band [22]. This is largely due to distinct propagation mechanisms, such as increased susceptibility to blockage and more pronounced effects of surface roughness, which may alter the multipath channel structure compared with lower frequencies. Existing standardized channel models, such as the 3GPP TR 38.901 model [45] and the ITU Radiocommunication Sector (ITU-R) P2040 model [46], support frequencies only up to 100 GHz and very specific sub-THz bands. Thus, expanding these standard models is essential to characterize sub-THz channels through dedicated measurements and new modeling approaches. However, extending current models to sub-THz frequencies is not straightforward due to substantial differences in multipath characteristics. Moreover, these standard channel models were proposed purely for communication services. With growing interest in integrating sensing and communication capabilities, there is an urgent need to develop a unified

TABLE 2. Main PHY challenges arising at sub-THz frequencies.

Challenge	Contribution	Section
Understanding and modeling of radio propagation	Channel Measurements	III-A
	Channel Modeling	III-B
RF power consumption and complexity	Performance of RF Components	IV-A
	Energy Efficiency of Sub-THz Transceiver Architectures and Related Optimization Trade-Offs	IV-B
	Implications of EMF Exposure Limits on Sub-THz Communications	IV-C
	Evolution of 5G NR Waveforms and Numerology	V-A-1
	PN-Robust Constellations Under PAPR Constraints	V-A-2
	Zero-Crossing Modulation	V-A-3
	Massive MIMO with 1-Bit Data Converters	V-B
	Energy-Efficient Network Deployment	V-D
Hardware impairments	Evolution of 5G NR Waveforms and Numerology	V-A-1
	PN-Robust Constellations Under PAPR Constraints	V-A-2
	Polar Constellations	V-A-4
	ML-Based Context-Aware Receiver for PN Compensation	V-C

channel model that bridges the stochastic and geometric approaches used by the two domains.

B. RF POWER CONSUMPTION AND COMPLEXITY

Sub-THz links suffer from a higher path loss when considering single-antenna systems compared with lower frequencies. This means that, in order to fulfill link budget requirements, either high-gain antennas (which are only suitable for static infrastructure links) or large antenna arrays (which allow flexible beamforming toward moving UEs) are needed. However, large antenna arrays may lead to prohibitive RF power consumption and complexity. First, the maximum PA output power decreases with the frequency due to technology limitations. Second, increasing the frequency also increases the NF of the receivers, while the wide bandwidth makes the impact of noise more severe, both affecting the link budget significantly. The expected performance of PAs and LNAs are analyzed briefly in Section IV-A. Second, the wide bandwidths—larger than 1 GHz—that motivate the use of the sub-THz band come with a substantial increase in the ADC/DAC and digital signal processing (DSP) power consumption. In order to optimize the network energy efficiency, the corresponding impact is investigated in Section IV-B, which also illustrates the role of proper dimensioning of MIMO architectures.

1) DATA CONVERTERS

A major issue arising when operating with wide bandwidths is related to the power consumption of the data converters. Specifically, the power consumption of each ADC/DAC scales at least linearly with the sampling rate and exponentially with the number of resolution bits [47], [48]. Regarding the ADCs, this scaling is linear with the bandwidth until about 330 MHz and subsequently becomes quadratic [49], severely affecting the energy efficiency and heat dissipation. This problem is exacerbated when massive antenna arrays are required. In this setting, reducing the power consumption and complexity associated with the data conversion imposes a drastic reduction in either the number of RF front ends or the resolution of the data converters in each RF front end (even down to 1 bit). The first approach, leading to hybrid analog-digital architectures, does not scale well at sub-THz frequencies due to the complexity of the additional analog circuitry required. The second approach introduces nonlinear quantization distortion, which degrades the spectral efficiency, but still allows to achieve remarkable energy efficiency [50], [51].

2) ENERGY-EFFICIENT NETWORK DEPLOYMENT

When looking at typically discussed use cases as, e.g., airport halls, shopping malls, or large office areas [52], it becomes clear that they cannot be covered by one BS only. Multiple BSs need to be deployed, with each of them equipped with large antenna arrays and multi-stream capabilities. Hence, even with optimized RF transceiver architectures, a further dimension of optimizing energy efficiency and an additional trade-off can be exploited: the impact of deployment and MIMO configuration on throughput and energy efficiency [53]. There are degrees of freedom and various possibilities to deploy a sufficient number of BSs, define transmit power, and optimize MIMO architecture to achieve a target coverage and throughput. These various options can be very different in terms of power consumption. A denser placement of BSs usually requires less transmit power and fewer streams per BS for a similar overall performance, leading to lower total power consumption. An example is analyzed in Section V-D. On the other hand, the number of baseband processing units and streams within the system may increase, consuming more power. To find the trade-off for an optimum deployment in combination with an appropriate MIMO architecture, an accurate power consumption model is needed, comprising not only the PAs, but all the parts in the system.

C. HARDWARE IMPAIRMENTS

Implementing sub-THz wideband RF transceivers challenges modern circuit technologies in many ways. The form factor of the transceivers decreases, making it challenging to fit all

the electronics under a small antenna area. The power delivery capabilities of the transistor technologies decrease, while the gain per amplifier stage also decreases, deteriorating the efficiency of the amplifiers [54]. The dissipated power needs to be cooled in a small physical area, making PA efficiency very relevant from the reliability perspective in addition to energy efficiency. In addition to traditional narrowband amplitude and phase distortion, extremely wide bandwidth at sub-THz frequencies may cause severe memory effects. However, the nature and strength of these effects are highly dependent on the specific PA topology and technology. To the best of our knowledge, no conclusive evidence has been established proving whether memory effects are inherently more severe in sub-THz transmitters compared to those operating at lower frequencies.

One challenge in mmWave and sub-THz arrays arises from the limited antenna isolation combined with circulator-free transmitters [55]. Circulators in general are bulky and, with the current state of technology, have not been implemented at sub-THz frequencies. The circulator-free approach causes the PAs to experience a load that varies with the beamforming, tightly coupling the PA nonlinear distortion with the beamforming behavior. While this challenge is well understood at the lower end of the mmWave spectrum, it is expected to become even more significant in the sub-THz range. In addition, wideband responses increase the need for frequency-dependent compensation of in-phase and quadrature (IQ) imbalance and other RF impairments [56].

The NF of the LNAs increases and the wide bandwidth further increases the impact of thermal noise [52]. The quantization distortion of the data converters becomes relevant due to the reduced resolution mandated by the need for feasible power consumption.Moreover, the form factor and impact of hardware impairments require integrating more components under a single integrated circuit, making the choice of technology crucial to minimize cost and power consumption. To realize the best compromise, heterogeneous integration to combine multiple integrated circuit technologies within the same package becomes crucial [57]. On the signal processing side, enablers for tolerating the increased effect of the hardware impairments are different compensation techniques in different levels in time and spatial domains. In this context, understanding the effect of hardware impairments in different waveforms and RF transceiver architectures is essential.

Lastly, a key hardware impairment arising in the sub-THz band is the increased PN stemming from the imperfect LOs. The PN of the LOs increases 20 dB/decade when increasing the carrier frequency and 10 dB/decade when increasing the bandwidth [52]. Moreover, wide bandwidth makes also the effect of the LO noise floor dominant in the overall PN performance, while the effect of slow phase drift decreases due to the reduced symbol lengths in the waveforms [58]. Since improving the spectral purity of the LOs is expensive and thus infeasible for consumer-level hardware, signal processing techniques at the baseband level need to be developed. The PN can be characterized as the superposition of a correlated low-frequency component and an uncorrelated high-frequency component. These are typically modeled as a Wiener and Gaussian processes, respectively. The correlated Wiener PN can be mitigated with the help of the phase tracking reference signals (PTRS), which allows tracking the phase of the LO. However, the uncorrelated Gaussian PN poses significant challenges due to its inherent randomness, particularly in wideband transmissions such as those occurring in sub-THz scenarios.

III. SIGNAL PROPAGATION AND CHANNEL MODELING

The design of highly efficient and reliable sub-THz communication systems requires to understand how the signal propagates and interacts with the physical objects in the environment. A number of channel measurements at sub-THz frequencies exist [59], [60], [61], but they still do not provide sufficient channel data of different environments and frequency bands for statistical channel characterization. Most of the recently proposed models still follow the 3GPP cluster-based modeling framework without considering the internal structure of sub-THz propagation channel [22], [62]. In this section, we provide a detailed perspective on sub-THz radio propagation based on extensive channel measurement results and, accordingly, develop new channel models for sub-THz communications. All the contributions in this section address the challenge of *understanding and modeling of radio propagation* described in Section II-A.

A. CHANNEL MEASUREMENTS

Recently developed frequency-domain and time-domain sub-THz channel sounders are briefly introduced. These sounders are used to perform both site-specific propagation measurements, such as reflection in Section III-A.2 and diffraction in Section III-A.3, and cellular-type channel measurements in Section III-A.4, together with detailed analysis results.

1) SUB-THZ CHANNEL MEASUREMENT SYSTEMS

The measurement-based characterization of the sub-THz propagation channels requires a large amount of channel data spanning multiple frequencies and scenarios. In this way, new findings can be derived from the statistical analysis of extracted channel parameters regarding time, frequency, space, and polarization. Several measurements exist for sub-THz channels. However, they provide some restrictions, such as limited dynamic range, resulting in the reduction of detectable multipath components (MPCs) and the limited measurement distance between the transmitter and receiver. In addition, the data available is not enough to support stochastic channel modeling and ML training. Therefore, highly efficient channel sounders are urgently required for channel data collection.

A simple way to perform sub-THz channel sounding is to employ vector network analyzer (VNA), where the channel transfer functions are measured directly in frequency domain

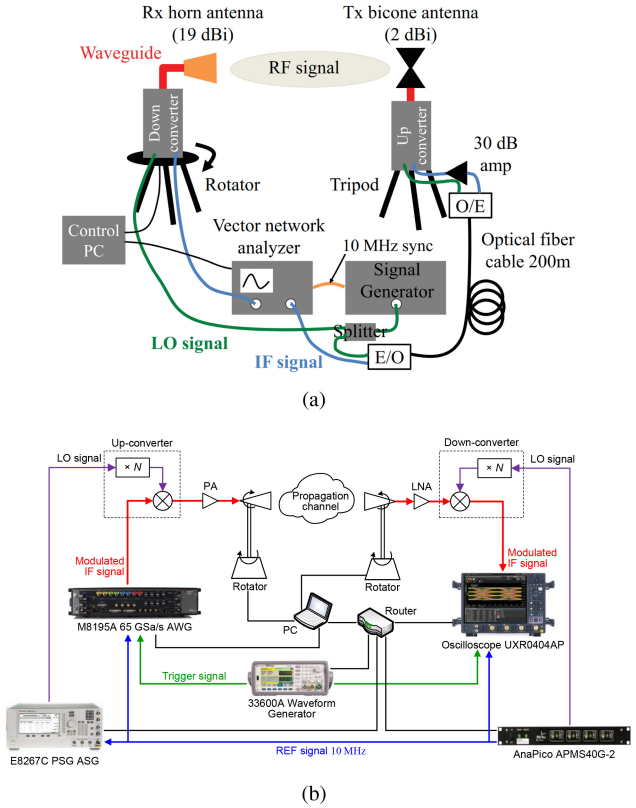

FIGURE 3. [Section III-A1] Sub-THz channel sounders: (a) VNA-based channel sounder [63]; (b) correlation-based channel sounder using COTS instruments [65].

via frequency sweeping over a specific range (bandwidth). In this setup, both transmit and receive antennas are connected to the VNA ports, reducing significantly the dynamic range of the system due to the cables' high transmission loss. To address this issue, the radio-over-fiber (RoF) technique is introduced to the existing VNA-based channel sounding solution, as depicted in Figure 3(a) [63]. The intermediate frequency (IF) signals transmitted and received at the VNA are translated to RF signals through up- and down-converters. The signal generator supplies the LO signal needed for frequency conversion. These IF and LO signals are shared to the transmitter side of the sounder through the RoF. The sounder is also equipped with a rotator at the receiver side to scan the channel in different directions. A personal computer is used to automate and synchronize the operation of the VNA and the rotator. The calibration, characterization, and additional information on this VNA-based channel sounder are elaborated in [64].

Because of the extended measurement duration, especially when using a larger number of frequency points in the sweep and lower IF bandwidth, the VNA-based sub-THz channel sounder is not suitable for real-time measurements, leading to a reduction of measurement locations for statistical channel modeling. Consequently, an efficient correlation-based channel is developed using COTS instruments, as shown in Figure 3(b) [65]. At the transmitter side, a Golay complementary sequence pair (generated by the personal computer) is downloaded to the arbitrary waveform generator (AWG) after the process of zero-insertion and pulse shaping. The modulated IF signal is mixed with the LO signal in the up-converter and then the output RF signal is amplified by the PA before being radiated by the transmit antenna. At the receiver side, the received signal is first amplified by the LNA and then mixed with the LO signal (from a dedicated signal generator) in the down-converter. The IF signal is captured and digitized by a real-time oscilloscope. To improve the signal-to-noise ratio (SNR) and reduce the size of the data set, the oscilloscope is tuned to the carrier frequency of the input IF signal for resampling within the bandwidth of interest. Then, the resulting digitally down-converted baseband signal is transferred to the personal computer for further processing. The main instruments, including AWG, oscilloscope, and two LO signal generators, share the same 10 MHz reference clock signal for frequency synchronization. To enable time alignment between the transmitter and receiver, an external waveform generator is employed to provide 1 pulse per second (PPS) trigger signal. Furthermore, using frequency extenders can upgrade this channel sounder to measure other sub-THz frequencies and bands under consideration for 6G.

Due to the increasing interest in sub-THz channel modeling with measurement-based evaluation, several groups have also developed measurement capability for such research following RoF-enabled VNA-based sounding method [66], [67], correlation-based sounding method [68], [69], and digital chirp sounding method [70].

2) REFLECTION MEASUREMENTS FROM ROUGH SURFACES

Sub-THz communications are envisioned to work mainly in line-of-sight (LoS), but the transmit-receive visibility line might be temporarily blocked by an object. In this context, the transmission can be maintained through reflected paths. However, these paths degrade the system's link budget by adding a new reflection loss. Hence, the characterization of reflection loss is necessary to accurately assess the radio performance at sub-THz bands. The reflection coefficient is theoretically given by the Fresnel equations for a planar smooth surface. It indicates the reflection gain experienced by a path when reflected by a surface, which depends on the material permittivity, the incidence angle, and the electromagnetic (EM) wave polarization. For instance, the reflection coefficient r for the air to material interface and a normal incidence is equal to $(1-\sqrt{\epsilon_r})/(1+\sqrt{\epsilon_r})$, where ϵ_r is the material permittivity. Many studies used the relative permittivity proposed by the ITU-R P2040 model [46], where the permittivity was considered constant regardless of the frequency. This model was mainly defined up to 100 GHz, although recent work [71], [72] showed that the model could be extended up to 300 GHz with homogeneous and flat surface materials such as glass or plexiglass. When the surface is rough, as illustrated in Figure 4, scattering occurs and the wave power reflected in the specular direction

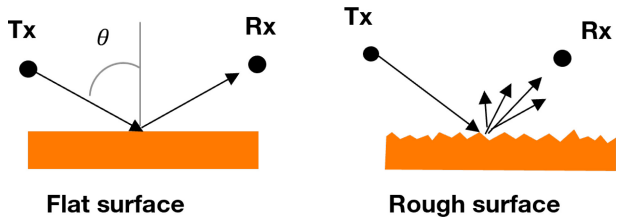

FIGURE 4. [Section III-A2] EM scattering on flat and rough surfaces.

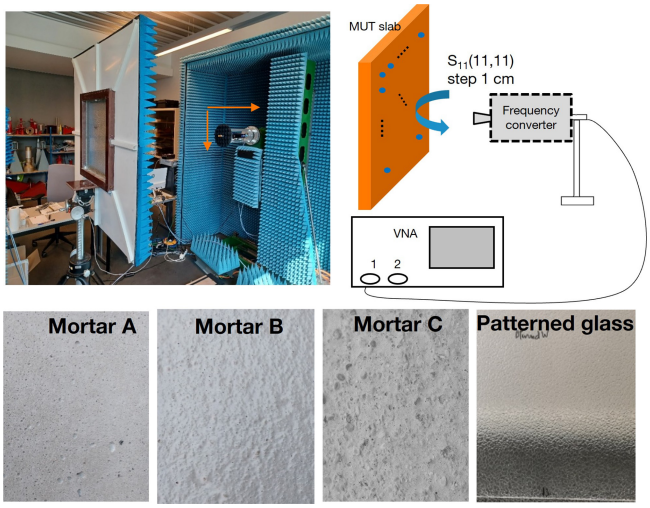

FIGURE 5. [Section III-A2] Measuring system used for material reflection loss estimation [80].

is diminished as a portion of the incident wave is re-radiated in various scattered directions. In this case, the Fresnel equations overestimate the reflection coefficients in the specular direction. This section analyzes the reflection measurements on rough surfaces at a normal incidence and the reflection gain variation depending on the reflection point. It complements the state of the art in EM scattering, where the main focus is the power angular distribution of the scattered component [73], [74], [75], [76], [77], [78], [79].

The measuring equipments consist on a VNA and frequency extenders. The measurements are divided into three sub-bands, i.e., 5–40 GHz, 110–170 GHz, and 170–260 GHz, according to the frequency limits of the VNA, frequency extenders, and antennas. For frequencies below 40 GHz, we employ a dual-ridge ultra-wideband antenna, and above 50 GHz, we use a standard horn pyramidal antennas. Figure 5 illustrates the measuring system used to obtain the reflection coefficients of the mortars of different roughness and the patterned glass. The material under test (MUT) is placed at normal incidence in front of the transmit and receive antennas. The measuring antennas of the transmitter and receiver can move along a vertical plane, enabling the scanning of the material by performing an $M \times N$ measurement matrix. An 11×11 measurement matrix (i.e., $M = N = 11$) with a spacing of 1 cm between points is conducted. The measurement matrix analyzes the impact of the reflection point location on the reflection coefficient. The intrinsic reflection frequency response of the MUT is denoted by $H^{\mathrm{MUT}}(f, m, n)$, with $m \in [1, M]$ and $n \in [1, N]$. This response is derived from raw S_{11} parameters collected by the VNA. The data processing applied to raw measurements includes normalization using reference measurements and time gating to eliminate undesired components such as wall reflection or material edge diffraction. The time gating operator is also configured to retain only the reflection from the illuminated side of the material facing the transmitter while rejecting the reflection from the opposite side. More information on the data processing is provided in [81]. The average power profiles of $H^{\mathrm{MUT}}(f, m, n)$ are given in dB and expressed as

$$\mathrm{ppH}^{\mathrm{MUT}}_{\mathrm{mean}}(f) = 10\log_{10}\left(\frac{1}{MN}\sum_{m,n}\left|H^{\mathrm{MUT}}(f, m, n)\right|^2\right). \quad (1)$$

Furthermore, $\sigma^{\mathrm{MUT}}(f)$ is defined as the standard deviation of $10\log_{10}(|H^{\mathrm{MUT}}(f, m, n)|^2)$ at frequency f calculated on the $m \times n$ measurement point matrix. In addition, $\sigma^{\mathrm{MUT}}(f)$ characterizes the reflection gain variation due to the different reflection point location.

Figure 6(a) depicts the average power profiles of different rough mortars and patterned glass. The average power profiles are compared with the theoretical power reflection coefficient $|r|^2$ using the permittivity of concrete ($\epsilon_r = 5.3$) and glass ($\epsilon_r = 6.3$) provided in [71]. The theoretical power reflection is equal to $10\log_{10}|r|^2$ in dB. The mortars A, B, and C are characterized respectively by low, medium, and high roughness. These illustrate the surface roughness impact on the reflection coefficient due to scattering. When the frequency and/or the surface roughness increase, the average power profiles decrease. For frequencies below 40 GHz, the average power profiles are close to the theoretical power reflection for mortars A, B, and C, indicating that scattering is negligible. However, at frequencies above 100 GHz, the average power profiles are reduced compared with the theoretical power reflection by around 5 dB for mortar B and 10 dB for mortar C. The reflection gain strongly depends on the reflection point location. For instance, the reflection gain variance for mortar A is always lower than 1 dB but reaches 5 dB for mortars B and C above 100 GHz as indicated in Figure 6(b). The scattering effect may erase the specular reflected path at some points as the reflection gain may be lower than −20 dB for frequencies above 100 GHz. We conclude that rough surfaces such as mortar surfaces can be extended to any smooth but non-flat surface such as patterned glass, as illustrated in Figure 6(a) and 6(b).

3) DIFFRACTION MEASUREMENTS OVER MULTIPLE BLOCKERS

As sub-THz signals are highly susceptible to blockage by physical objects, one of the primary components to understand sub-THz radio propagation is analyzing the fundamental propagation effects. Based on short-range LoS

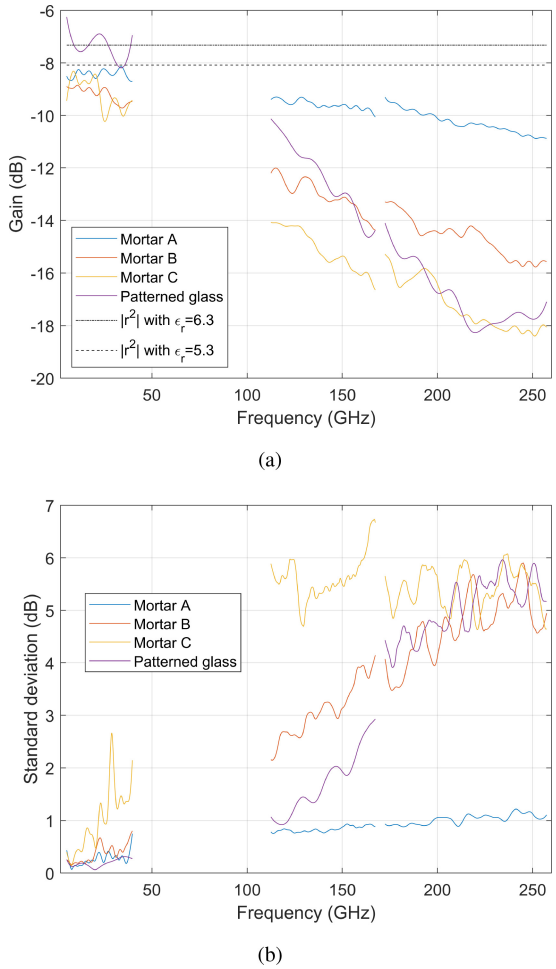

FIGURE 6. [Section III-A.2] Reflection measurements for different mortars and patterned glass: (a) $ppH^{MUT}_{mean}(f)$; (b) $\sigma^{MUT}(f)$.

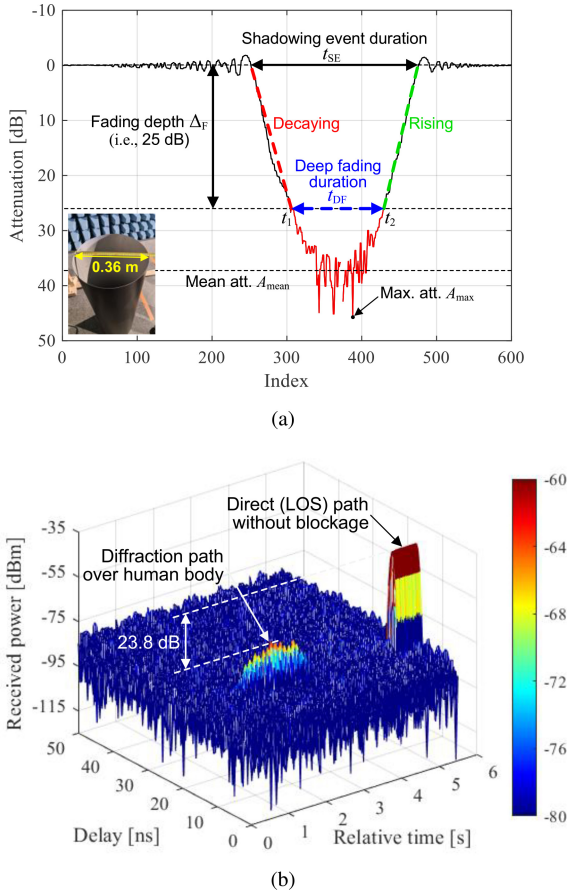

FIGURE 7. [Section III-A.3] Characterization of human blockage effect in the D-band: (a) reference measurement results with cylinder moving across the LoS link [82]; (b) human blockage attenuation with human blocker moving along the LoS link.

measurement data, the blockage effect caused by human body and small objects, e.g., finger, are analyzed in [82] and [83], respectively. Example with a standard cylinder moving across the LoS link in the middle of transmitter-receiver line is given in Figure 7(a). As the obstacle moves closer to the direct path between the transmitter and receiver, significant attenuation can be observed within the deep fading duration. Here, the deep fading duration t_{DF} is defined as the time difference between the beginning and end of attenuation pattern crossing the threshold Δ_F with negative and positive slopes. Such fading behavior determines how fast the handover protocol should be to establish a stable communication links. Figure 7(b) shows the time-delay power delay profile (PDP) with the human blocker frontally moving along the LoS link. As the blocker moves to the middle of the transmit-receive link, diffraction paths over double edges of human body can be detected leading to the reduction of human blockage attenuation. Moreover, dual-polarized diffraction measurement results as reported in [84] show that knife edge diffraction (KED) model provides a good agreement with the diffraction losses caused by a thin metal and laminated board. Meanwhile, our measurements show over 26 dB cross-polarization ratio between co- and cross-polarization channels.

4) CELLULAR-TYPE CHANNEL MEASUREMENT CAMPAIGNS

Channel measurements from 140–144 GHz using the VNA-based channel sounder presented in Section III-A.1 are performed in an indoor entrance hall environment and outdoor sites such as suburban, residential, and city center. The numbers of LoS and NLoS links together with the link distance ranges are listed in Table 3. The receiver, which is placed at a corner of the building, acts as the BS and is equipped with a 19 dBi directional horn antenna, while the transmitter is the UE with a 2 dBi omnidirectional bicone antenna and is placed in different locations. The layout of the antenna locations and map of each environment are shown in [85], [86, Figs. 3–4]. The transmit and receive antennas are both vertically polarized. The power-angular delay profile (PADP), containing the received signal intensity as a function of the propagation delay and the horn antenna's pointing direction, of each measured link is obtained from these single-directional measurements. Then, a local peak search and de-embedding of the antenna gains are applied

TABLE 3. [Section III-A.4] measurement campaign details.

Environment	LoS links	NLoS links	Link distance range
Entrance hall	28	47	3–65 m
Suburban	35	4	2–162 m
Residential	23	38	20–175 m
City center	12	23	10–178 m

to the PADPs to derive the discrete single-directional MPC parameters. A measurement-based ray-launcher [86] is then applied using these MPC parameters and a laser-scanned point cloud map of the environment as inputs to estimate the discrete double-directional MPC parameters, which can be accessed in [85].

B. CHANNEL MODELING

The development of sub-THz geometry-based stochastic channel models relies heavily on a sufficient amount of measured channel data, which requires a collective effort from our community. A sub-THz stored channel model and a ray-based channel model are presented in Sections III-B.1 and III-B.2, respectively. Based on the initial channel measurement results in Section III-A.4, a refined stochastic model is developed following the 3GPP channel modeling framework. Moreover, statistical models are introduced for the purpose of theoretical analysis as described in Section III-B.4.

1) STORED CHANNEL MODEL

The lack of measurements in the sub-THz bands challenges the development of stochastic channel models that can be used for the design and evaluation of sub-THz systems. An alternative in this regard is the playback of measured sub-THz channels, i.e., generating channel responses based on the stored multipath channel data collected in Section III-A.4. The time-variant frequency response of the refined stored radio channel model can be expressed as

$$H(t,f) = \sum_{l=1}^{\mathcal{L}} G_{\mathrm{Rx}}(\Omega_l^{\mathrm{Rx}}) G_{\mathrm{Tx}}(\Omega_l^{\mathrm{Tx}})^{\mathrm{T}} \sqrt{\alpha_l(t) p_l} \times \frac{\exp(j\varphi_l)\exp(j2\pi\upsilon_l t)}{\exp(j2\pi f \tau_l)} \in \mathbb{C}^{N_{\mathrm{Rx}} \times N_{\mathrm{Tx}}}, \quad (2)$$

where $\mathcal{L}$ represents the total number of paths, N_{Tx} and N_{Rx} indicate the number of transmit and receive antennas, respectively, $G_{\mathrm{Rx}}(\Omega_l^{\mathrm{Rx}}) \in \mathbb{C}^{N_{\mathrm{Rx}} \times 1}$ and $G_{\mathrm{Tx}}(\Omega_l^{\mathrm{Tx}}) \in \mathbb{C}^{N_{\mathrm{Tx}} \times 1}$ denote the complex radiation patterns at the receive and transmit antennas, respectively, Ω_l^{Rx} and Ω_l^{Tx} denote the angle of arrival (AoA) and angle of departure (AoD) of the l-th path, respectively, and p_l, φ_l, τ_l, and υ_l denote the path gain, random initial phase, propagation delay, and Doppler frequency of the l-th path, respectively. The phase φ_l is uniformly distributed in $[0, 2\pi]$. Furthermore, the temporal dimension and time variability are included in the Doppler frequency υ_l, where only the phase of the l-path changes over time while the other propagation parameters remain constant. To include the blockage effect in (2), a time-varying attenuation term $\alpha_l(t)$ is added, which can be obtained, e.g., from the human blockage measurement results in Section III-A.3. The proposed sub-THz stored channel model is openly available in [85], which can support D-band channel generation in multiple measured environments with arbitrary transmit and receive antenna configurations. Moreover, molecular absorption (e.g., modeled as in [87]), can be readily integrated.

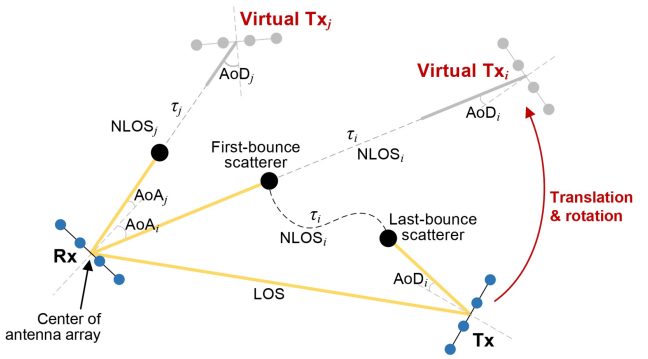

FIGURE 8. [Section III-B.1] Illustration of the near-field extension of the proposed sub-THz stored channel model [89].

The proposed sub-THz stored channel model replays the MPCs measured under far-field channel conditions. However, the deployment of extremely large-scale antenna arrays and the use of sub-THz bands significantly extend the near-field region of the transmitter and/or receiver, potentially up to several hundred meters. To incorporate near-field effects into the sub-THz stored channel model, a simple method was developed to determine the propagation distance between each transmit and receive antenna element based on the path parameters specified by the original model. This procedure is straightforward for the LoS path, as the locations of the individual antenna elements are known. For the NLoS paths, modeling the wave curvature is not trivial, as it depends on the type of wave-object interaction and the distance between interacting objects. In this context, a simplified approach inspired by image theory can be employed when the propagation is dominated by specular reflections [87]. This involves rotating the transmit antenna array within the global Cartesian coordinate system, as illustrated in Figure 8, so that the arrival and departure angles are aligned and the distance between the centers of the arrays matches the original path length. Per-element distances can then be calculated in the same way as for the LoS path, using the original receive element coordinates and the derived virtual transmit coordinates. This operation is performed independently for each path. The underlying assumption is that each interaction is a reflection, which is the most common and highest-gain propagation mechanism at sub-THz frequencies. A detailed mathematical description of the proposed method is provided in [88].

2) RAY-BASED CHANNEL MODEL

One of the main techniques to model and study the wireless propagation of the waves is ray tracing technique. In ray

tracing, the propagation of EM waves is modeled with approximations of Maxwell's equations, instead of employing the equations directly. Two main methods to implement ray tracing are ray launching or shooting bouncing rays method and image method [90]. These methods mainly differ in the way how they simulate the propagation paths from the transmitter to the receiver. In ray launching method, a certain number of rays are transmitted through random paths in the 3-dimensional (3D) environment, and followed through their paths until the power of the signal that is represented by the ray is below a predetermined threshold. By employing the image method, the exact number of propagation paths can be produced for a given maximum reflection order. In this section a ray-tracing technique based on image method is developed in order to model some indoor propagation scenarios under assumption that a directive pencil beam is required for sub-THz communications in order to overcome high propagation loss. The model is further compared with some measurement results.

Ray tracing is implemented using the image method to ensure the simulation of all of the possible paths between the transmitter and receiver. In the image method, pseudo transmitters are created for every reflective object to model reflections. A path from the transmitter to the receiver can be defined as an p-th order reflection path, if there are exactly p reflections in the path from the transmitter to the receiver. In order to simulate an p-th order reflection path, p pseudo transmitters are required, which leads to total of 2^p possible paths that should be processed, resulting in exponential computational complexity with the number of reflections. By employing the image method, the exact number of propagation paths can be produced for a given maximum reflection order.

The ray-tracing simulator showcased enables the simulation of indoor scenarios involving sub-THz frequency wireless transmission and reception, providing deterministic channel characterization. Through ray tracing, it becomes possible to derive the PDP of the channel, determine the AoAs, and extract the phase of the output signals. Employing ray tracing with the image method allows for the characterization of the PDP of the channel, which is crucial in wireless communication, across diverse indoor scenarios. This involves calculating the received power and travel duration for each ray using the free-space path loss model.

To incorporate the contribution of NLoS paths into the PDP, it is essential to model and incorporate reflections. This process consists of two subtasks:

1) Identify all the reflections up to the third order that delineates a path connecting the transmitter and receiver. Higher-order reflections have a minimal impact on channel characterization and hence are not considered.
2) Calculate the reflection losses for each reflection path.

TABLE 4. [Section III-B.2] default configuration for ray tracing.

Parameter	Default value
Carrier frequency	252 GHz
Signal polarization	Vertical
Transmit directivity	25.5 dBi
Receive directivity	25.5 dBi
Transmit power	0 dBm
Max number of reflections	3

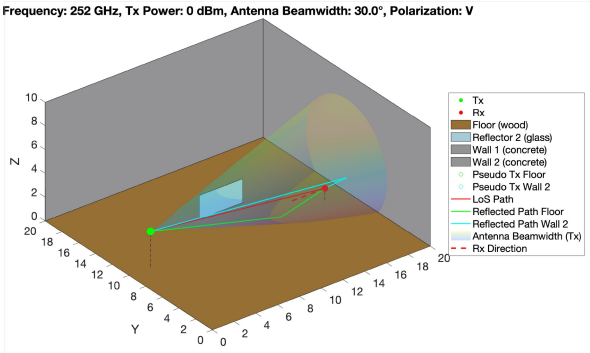

FIGURE 9. [Section III-B.2] Floor and wall reflections setup.

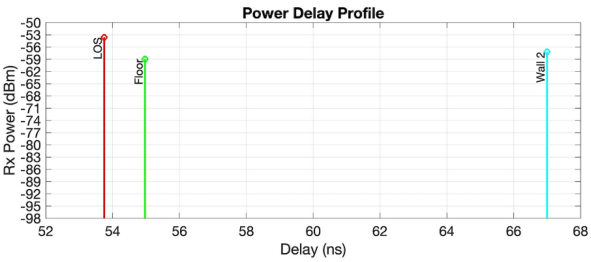

FIGURE 10. [Section III-B.2] Floor and wall reflections output.

The initial subtask is accomplished by employing the image method, which facilitates the calculation of deterministic paths and ensures no paths are overlooked. For the second subtask, the reflection loss is obtained through the Fresnel equations.

The ray tracing simulator is used to explore two scenarios. The first scenario consist of two first order reflections with LoS, and the second scenario incorporates reflections with multiple orders. Table 4 summarizes the default configurations used in the simulations. Figure 9 illustrates the first scenario. It can be seen that there is one reflection from the floor and the back wall. Moreover, there is no reflection from the glass reflector, as it is outside the antenna beam width. The resulting output is depicted in Figure 10. In this regard, despite having traveled a longer path, the reflection from the wall has higher received power than the reflection from the floor due to the polarization of the signal. Vertically polarized signal has significantly more reflection loss in vertical surfaces than horizontal surfaces.

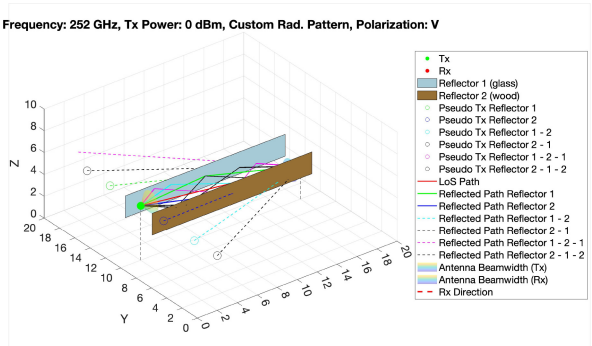

FIGURE 11. [Section III-B.2] Higher-order reflections setup.

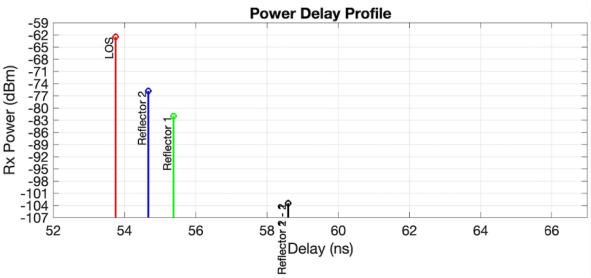

FIGURE 12. [Section III-B.2] Higher-order reflections setup output.

FIGURE 13. [Section III-B.2] Reflection testing setup with receiver (left) and transmitter (right). The anti-reflection foam can be seen on the antennas.

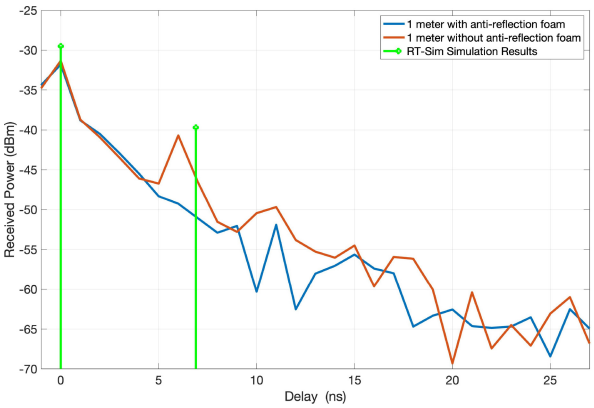

FIGURE 14. [Section III-B.2] Estimated channel amplitude.

Figure 11 illustrates the setup of the second scenario with LoS path and first and second order reflections. The output for this scenario is depicted in Figure 12. In the PDP, it is evident that the second-order reflection exhibits minimal power at the receiver. This observation aligns with the assumptions, as the second-order reflection experiences lower power due to its longer path length, resulting in higher propagation loss, as well as more significant reflection loss due to the experience of two reflections compared with just one. This example illustrates that multiple-order reflections have a negligible effect in our setup in the sub-THz range. The antenna beam-width is fixed to 30° in both examples.

To compare the ray-tracing simulation and channel measurement results, a very simple scenario is setup as shown in Figure 13. Due to the geometry of the up-converter and the down-converter, when these two devices are directed at each other with no other object in their proximity, a ping-pong effect is detected, where the input signals are reflected back and forth from the front surfaces of the converters and detected at the receiver side. In order to do mitigate this effect and get a LoS only channel, absorption foams are placed around the antennas. This setup is presented in Figure 13. Figure 14 compares the channel measurements with and without the anti-reflective foam, alongside simulation results. There is a peak observed at around 6 ns in the setup without foams. This peak arises due to the ping-pong effect that occurs in the absence of foams. Following these measurements, the objective is to replicate the same setup within a ray-tracing simulator environment and simulate the system. Upon examining Figure 14, it is evident that the simulation results closely resemble the scenario where no anti-reflection foam is employed. The LoS path is estimated with a margin of error of 2 dB, while the delay of the reflective path is estimated with a margin of error of less than 1 ns (considering the measurement resolution of 1 ns). This confirms the accuracy of the developed simulator in estimating channel responses across indoor scenarios.

In summary, we develop a ray-tracing simulator based on the image method to analyze the propagation of sub-THz waves in indoor settings, which can effectively models propagation effects, including propagation loss and reflections from various materials. The simulation results are compared with channel measurements conducted in a laboratory environment, revealing a strong correlation between the measurements and the ray-tracing outcomes

3) REFINED 3GPP-LIKE STOCHASTIC CHANNEL MODEL

In existing stochastic channel models, the cluster angle offsets relative to the reference direction, i.e., the direction of the other link end, monotonically increases as the cluster power decreases, as shown in a sample MPC distribution in Figure 15(b). While straightforward, this original approach fails to accurately reproduce the measured channels in that strong clusters can be in random directions with varying angular separation to the reference direction, as shown in Figure 15(a). This method was adopted for the standardized stochastic channel model 3GPP TR 38.901 [45] and other popular cluster-based models, such as the ITU-R M.2412 [91], METIS [92], and WINNER II [43]. Addressing

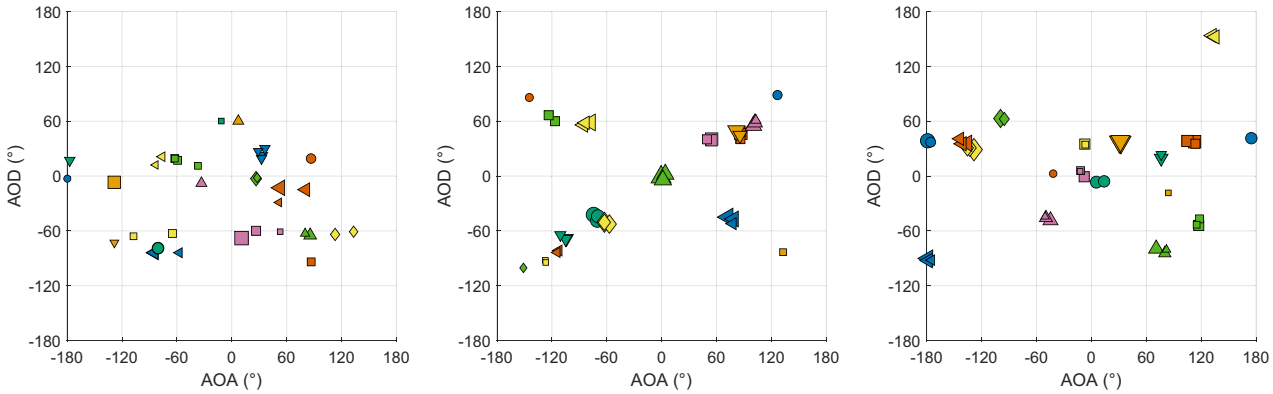

FIGURE 15. [Section III-B.3] Exemplary plots of MPC distribution of: (a) measured channel; (b) generated channel using the original approach; (c) generated channel using the proposed approach. The angles shown are the offset azimuth AoA and AoD with respect to the reference direction. The MPCs belonging to the same cluster have a unique marker color and style. A larger marker size means higher MPC power.

this simplified distribution of cluster angles may be more relevant at higher (e.g., sub-THz) frequencies, where the MPC distribution is more defined due to the use of more directional antennas. Our proposed approach allows strong clusters to appear randomly at any offset angle while satisfying the randomly drawn angular spread based on the distribution consistent with the measurements. The steps shown here are for azimuth AoA, but they can also be applied to azimuth AoD and zenith AoA/AoD by using their corresponding parameters.

The vector of cluster AoA offsets $\mathbf{\Phi} = [\Phi_s, \Phi_w]$ to be determined are first grouped into a vector of N_s strongest clusters Φ_s comprising $\mathcal{R}\%$ of the total power and a vector of the remaining clusters Φ_w. The *weak* clusters Φ_w are randomly drawn from a Gaussian distribution with zero mean and a standard deviation equal to the randomly drawn azimuth spread of arrival angle (ASA) as $\Phi_w \sim \mathcal{N}(0, \text{ASA}^2)$. The *strong* clusters Φ_s are determined using a direct search method called Nelder-Mead [93], which minimizes the objective function iteratively as

$$f(\Phi_s) = |\text{AS}(\mathbf{\Phi}, \mathbf{P}) - \text{ASA}|, \tag{3}$$

where $\text{AS}(\mathbf{\Phi}, \mathbf{P})$ is the angular spread of the resulting cluster angles in each iteration and $\mathbf{P}$ is the vector of cluster powers. The angular spread $\text{AS}(\mathbf{\Phi}, \mathbf{P})$ is given by

$$\text{AS}(\mathbf{\Phi}, \mathbf{P}) = \frac{180}{\pi} \sqrt{\sum_{n=1}^{N_c} |e^{j\phi'_{n,\text{AoA}}(\pi/180)} - \mu_{\phi,\text{AoA}}|^2 P_n}, \tag{4}$$

where $\phi'_{n,\text{AoA}}$ and P_n are the AoA offset and sum-normalized power of the n-th cluster, N_c is the number of clusters, $\mu_{\phi,\text{AoA}}$ is the mean AoA calculated as $\mu_{\phi,\text{AoA}} = \sum_{i=1}^{N_c} e^{j\phi'_{n,\text{AoA}}(\pi/180)} P_n$. The AoA of the n-th cluster is then obtained as

$$\phi_{n,\text{AoA}} = \phi'_{n,\text{AoA}} + \phi_{\text{LoS,AoA}}, \tag{5}$$

where $\phi_{\text{LoS,AoA}}$ is the direction of the transmitter relative to the receiver.

The proposed angle generation approach is verified by comparing the generated channels with the channels from 140 GHz measurements in an entrance hall scenario presented in Section III-A.4. The channels are generated using the 3GPP TR 38.901 channel modeling framework with the original and proposed approaches. Only the results for NLoS links and large antenna case are presented here. More results, as well as the simulation parameters and the channel model parameter values used, are presented in [94].

Figure 15(c) shows that the MPC of a generated channel using the proposed approach is randomly distributed similar to the measured channel shown in Figure 15(a). As the proposed approach optimizes the cluster angles such that the difference between the resulting angular spread and the randomly drawn angular spread is minimized, its angular spread distribution agrees well with the measured channels and performs slightly better than the original approach, as shown in Figure 16(a). This accurate reproduction of the angular characteristics of the channel resulted in improved agreement of the eigenvalue statistics between the generated channels using the proposed approach and the measured channels as illustrated in Figure 16(b).

4) STATISTICAL SMALL-SCALE FADING CHARACTERIZATION OF SUB-THZ CHANNELS

Channel characterization is fundamental for the successful deployment of sub-THz communication systems. As the frequency increases, the transmitted signal becomes more susceptible to singular propagation phenomena, such as atmospheric absorption, dynamic shadowing, and diffuse particle scattering, which can lead to higher path loss and decreased gains [95]. Of course, known techniques can be employed to circumvent some of these phenomena, however, by modeling their nature one can design a more efficient communication system. In the literature, multiple deterministic and stochastic models (Rayleigh, Rice, and Nakagami-*m*) have been proposed and standardized to characterize fading and other propagation phenomena over

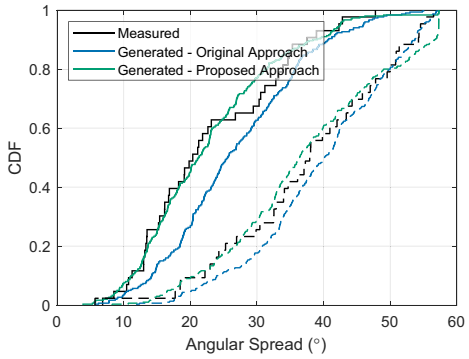

(a)

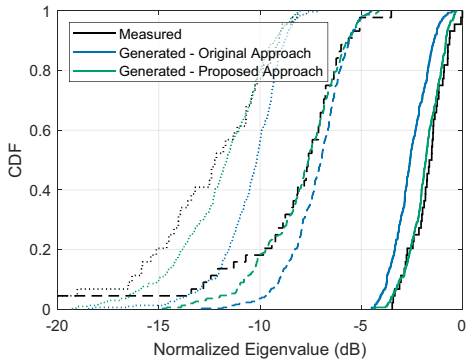

(b)

FIGURE 16. [Section III-B.3] Comparison of measured and generated NLoS links [87]: (a) CDFs of the azimuth angular spread of departure (solid line) and arrival (dashed line); (b) CDF of first (solid line), second (dashed line), and third (dotted line) highest normalized eigenvalues.

lower-frequency channels. In the sub-THz range, however, these classical models may not provide a good fit due to the new intricacies of the wireless channel.

To this end, recent works have resorted to more generalized and flexible stochastic models for sub-THz characterization, such as Saleh-Valenzuela (S-V) [96], fluctuating two-ray (FTR) [97], α-μ [98], α-η-κ-μ [99], and mixture of gamma and Gaussian mixture [100]. The work in [96] proposed and validated a modified S-V model to represent the multipath components of a sub-THz link inside a computer desktop environment. Furthermore, [97] employed the FTR distribution to model RIS-aided communications with frequencies ranging from 300 to 380 GHz. Reference [98] investigated channel characterization of indoor LoS and NLoS scenarios at 143.1 GHz employing multiple fading models, i.e., Rayleigh, lognormal, Rice, Nakagami-m, and α-μ models. The results indicated an almost excellent fit to the more flexible α-μ model. Reference [99] provided a new framework to evaluate the outage probability and bit error rate (BER) performance of α-η-κ-μ fading using a single-input single-output scheme at 275 GHz. Lastly, [100] employed mixture of gammas and Gaussian mixture models to accurately fit the multiple peaks that occur in the fading amplitude of outdoor sub-THz channels. This section adopts the κ-μ model, which offers remarkable flexibility to represent small-scale fading with dominant LoS components [101]. Specifically, the κ-μ model is well suited for characterizing the propagation in outdoor sub-THz links over long distances enabled by massive antenna arrays. Based on this, we present a preliminary performance analysis of a downlink system where a single-antenna UE is served by a multi-antenna BS employing maximum ratio transmission (MRT).

The κ-μ model is defined by the shaping parameters $\kappa > 0$ and $\mu > 0$ [102], which respectively indicate: i) the ratio between the total power of the dominant components and the total power of the scattered waves, and ii) the number of multipath clusters. The envelope probability density function and CDF of the κ-μ distribution are promptly available as mathematically tractable expressions in [102] and it encompasses other well-known fading models such as Nakagami-m, Rice, and Rayleigh. In multi-antenna systems, the power of the received signal can be expressed as a sum of squared random variables. In this context, [103] and [104] respectively proposed expressions for the CDF of the sum of independent and identically distributed (i.i.d.) and independent and non-identically distributed κ-μ random variables, which employ special functions such as the modified Bessel function, Marcum Q-function, and Laguerre polynomials. Furthermore, when spatial correlation is considered, the resulting expressions are likely to involve more intricate special functions such as the Meijer G-function, or may not even have a closed form, as observed for the Rice [105] and κ-μ shadowed [106], [107] correlated models. Thus, when considering massive numbers of antennas, existing analytical frameworks for the considered models become unsuitable due to their inherent computational complexity. In this work, we present an easy-to-evaluate framework for the sum of i.i.d. squared κ-μ variables, based on the results of [108]. This approach results in a new CDF expression, which allows the analysis of the coverage probability of sub-THz systems with MRT [109].

Considering a BS equipped with N_{Tx} antennas serving a single-antenna UE, the sum of i.i.d. squared random variables can be used to express the instantaneous downlink SNR when the BS adopts MRT. Hence, after tedious derivations, the CDF of the sum of N_{Tx} squared κ-μ variables can be expressed as [109]

$$F_W(w) = \left(\frac{(1+\kappa)\mu}{\exp(\kappa)}\right)^{\mu N_{\mathrm{Rx}}} \sum_{m=0}^{\infty} \frac{\left(w/\hat{w}\right)^{\mu N_{\mathrm{Rx}}+m} k_m}{\Gamma(\mu N_{\mathrm{Rx}}+m+1)}, \quad (6)$$

with k_m defined as

$$k_0 = 1, \quad (7a)$$

$$k_m = \frac{1}{m}\sum_{i=1}^{m}(i-m+iN_{\mathrm{Rx}})\Gamma(i+\mu)k_{m-i} \times \sum_{l=0}^{i}\frac{(-\kappa\mu)^{-l}\left(\kappa(1+\kappa)\mu^2\right)^i}{l!(i-l)!\Gamma(i-l+\mu)}, \quad m \geq 1, \quad (7b)$$

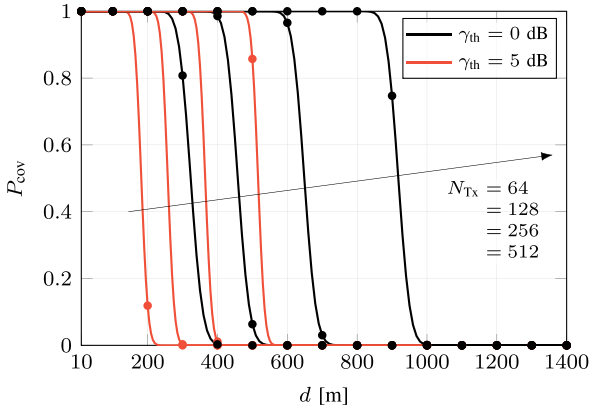

FIGURE 17. [Section III-B.4] Downlink coverage probability against distance, with $\kappa = 0.5$, $\mu = 0.5$, $f_c = 140$ GHz, $P_T = 30$ dBm, $\gamma_{th} \in \{0, 5\}$ dB, and $N_{Tx} = \{64, 128, 256, 512\}$ [109].

where $\hat{w} > 0$ is the scaling parameter and $\Gamma(\cdot)$ is gamma function [110, eq. (06).05.02.0001.01]. With (6), the coverage probability can be calculated as $P_{\text{cov}} = 1 - F_W(\gamma_{\text{th}})$, with γ_{th} being the SNR threshold.

Figure 17 shows the coverage probability against the distance between the BS and the UE with threshold $\gamma_{\text{th}} \in \{0, 5\}$ dB. We assume a log-distance path loss model with $\hat{w} = P_T \varphi / (\sigma^2 d^2)$, where P_T is the transmit power, σ^2 is the noise power, φ represents the frequency-dependent path loss factor referenced at 1 m, and d represents the distance between the BS and the UE. The path loss factor is given by $\varphi = (c/(4\pi f_c))^2$, where c is the speed of light and f_c represents the carrier frequency. The noise power is given by $\sigma^2 = -174 + 10 \log_{10} \Omega + \nu$ [dBm], where $\Omega = 0.01 f_c$ is the transmission bandwidth and $\nu = 5$ dB denotes the NF of the UE. We fix $P_T = 30$ dBm and assume $f_c = 140$ GHz. The severe fading conditions are reinforced with $\kappa = 0.5$ and $\mu = 0.5$. We set the number of antennas to $N_{\text{Tx}} \in \{64, 128, 256, 512\}$. The solid curves indicate the numerical evaluation whereas the markers depict the Monte Carlo simulation. In this scenario, using $N_{\text{Tx}} = 512$ compensates for the severe path loss at 140 GHz, ensuring excellent coverage up to approximately 450 m and 800 m for $\gamma_{\text{th}} = 5$ dB and $\gamma_{\text{th}} = 0$ dB, respectively. This impressive coverage performance predominantly results from the combination of the truly massive number of antennas and the LoS-dominated propagation. In [109], we consider other performance metrics, i.e., BER for coherent binary modulations and symbol error rate (SER) for M-ary phase-shift keying (PSK) and QAM, and provide a more extensive performance evaluation.

C. SECTION SUMMARY

Understanding radio propagation and channel characteristics is essential for developing reliable sub-THz wireless systems. In this section, we presented measurement-based evidence of sub-THz radio propagation characteristics, which has been incorporated into the development of sub-THz channel models. Using the advanced channel sounders described in Section III-A, extensive channel measurement campaigns were conducted to characterize reflection and diffraction across various materials, as well as to analyze cellular-type sub-THz channels in real-world settings. The site-specific measurement data enables precise characterization of NLoS path gains, providing insights into whether NLoS paths can support communication and localization at sub-THz frequencies. Additionally, the material-specific permittivity extracted from these measurements improves the accuracy of ray-based channel model. Furthermore, space-time channel parameters extracted from cellular-type measurements facilitate the statistical characterization of sub-THz propagation in diverse environments.

To develop a universal sub-THz channel model with high accuracy, collaborative efforts to share measurement-based insights are crucial. However, this remains challenging due to the limited availability of statistically significant measurement data in sub-THz bands. To address this, a sub-THz stored channel model in Section III-B.1 was developed to support the primary design and evaluation of sub-THz wireless systems. This model not only replays the propagation paths between transmitter and receiver, but also identifies major wave-interacting objects, including the types and coordinates of the first- and last-bounce scatterers. Since only measured channels can be stored and played back in the stored channel model, a ray-based model was developed as an alternative in Section III-B.2, which was calibrated and validated against field measurements. Furthermore, based on the statistical analysis of sub-THz channel parameters derived from our cellular-type measurements, existing geometric channel models were refined in Section III-B.3 for channel simulations up to 330 GHz. To account for the interplay between propagation channels and antenna systems (particularly in sub-THz massive MIMO systems) a generalized stochastic model, namely the κ-μ model, was presented in Section III-B.4 to facilitate the theoretical analysis of the system's performance. The sub-THz channel models developed within the Hexa-X-II project serve as a key enabler for the design, development, and implementation of sub-THz systems, contributing to the standardization of future 6G channel models.

A key aspect of sub-THz channel modeling not discussed in this section is molecular absorption, which increases path loss and noise at specific frequencies. Unlike large-scale path loss characterization, understanding molecular absorption above 100 GHz requires extensive collaborative efforts and long-term measurement campaigns. For instance, [111] presented line-by-line calculations of gaseous attenuation due to oxygen and water vapor between 1 and 1000 GHz. While accurate, such models rely on comprehensive databases that are not suitable for standardization purposes. On the other hand, [87] presented a simplified yet effective approach to model molecular absorption loss in wideband channels above 100 GHz, using exponential fitting to approximate the frequency-dependent absorption coefficient under specific environmental conditions. Despite some minor deviations around the absorption peaks, this model is well-suited for

practical use. Notably, it is worth pointing out that most sub-THz systems operating at carefully selected frequencies and over short distances experience minimal attenuation from molecular absorption.

The channel models discussed in this section primarily characterize sub-THz propagation channels between the transmit and receive antennas, which exhibit distinct properties compared with lower-frequency channels. However, wireless systems operate over the radio channel, which consists of antennas and RF front ends in addition to the propagation channel. Therefore, system design should be guided by a radio channel perspective, e.g., by accounting for the impact of beamforming on sub-THz wireless transmission [89], [112]. The accurate modeling of the radio channel, including the hardware impairments described in Section II-C, is essential for realistic evaluation and design of sub-THz systems, and thus constitutes a meaningful research direction.

IV. RF TRANSCEIVER DESIGN

Analog RF design becomes extremely challenging at sub-THz frequencies. The challenges arise from the capabilities of the circuit technologies with respect to their power efficiency, size, and cost, all critical for making sub-THz transceivers feasible for mass production and commercial use. Moreover, the EMF exposure from sub-THz devices needs to be compliant with relevant requirements. For the UE, the time-averaged power and effective isotropic radiated power (EIRP) are constrained due to the EMF exposure limits.

In recent years, numerous sub-THz links have been deployed and demonstrated across a range of frequencies. An extensive survey including a comparison of experimental testbeds can be found in [41], where link distances typically range from a few centimeters to 10–20 meters (with higher data rates achieved over short distances). For instance, [113] demonstrated a 110 Gbps link over 2 m using CMOS-compatible devices. At the opposite end, [114] demonstrated a 2-km link at 220 GHz using more specialized technologies, achieving a data rate of 2 Gps. Additional demonstrations of sub-THz systems are listed in [7]. The majority of the existing implementations consists of fixed links without active beam steering capabilities. One of the most advanced demonstrations of beam steering using commercially feasible circuit technologies is presented in [115]. As links with very high data rates have so far been realized over limited distances of only a few meters, it is clear that NF, PA output power, and beamforming play an important role in improving the link budget.

This section combines selected sub-THz RF transceiver design-related aspects, spanning from the realistic performance of key RF components in Section IV-A and the realistic energy efficiency of different beamforming architectures when selecting the components for different scenarios in Section IV-B, to the implications of EMF exposure limits on sub-THz communications in Section IV-C.

TABLE 5. [Section IV-A.1] estimated P_{sat} of different PA technologies in different frequencies.

f \ Technology	CMOS	SiGe	GaN	InP
40 GHz	27 dBm	30 dBm	46 dBm	30 dBm
140 GHz	14 dBm	20 dBm	24 dBm	29 dBm
240 GHz	0.6 dBm	10 dBm	2 dBm	26 dBm

The analog front-end components considered in the following mainly consist of ADCs/DACs, up-/down-conversion mixers, phase-locked loops (PLLs) and LO distribution, and power amplifiers (PAs, LNAs, and baseband amplifiers). All the contributions in this section address the challenge of *RF power consumption and complexity* described in Section II-B.

A. PERFORMANCE OF RF COMPONENTS

Link budget calculations and coarse performance evaluations of wireless radio links are usually based on a few basic radio parameters, namely transmit power (P_T), antenna gains, and receiver NF [116]. In more advanced link budget calculations, RF impairments such as nonlinear distortion, LO/PLL PN, quantization distortion of the ADC/DAC, IQ imbalance, and many others can also be included [117]. In the following, we review the expected performance of different circuit technologies by focusing on the achievable output power of PAs in Section IV-A.1 and NF of LNAs in Section IV-A.2. The performance estimates are derived based on existing references at three frequencies, i.e., 40 GHz, 140 GHz, and 240 GHz, in order to highlight the scalability of existing technologies.

1) PA OUTPUT POWER

A broad survey on the performance of different PAs realized in different technologies can be found in [54]. In [52] models of saturated power (P_{sat}) of different PAs were further combined for frequency-dependent analysis with some coarse trends. Note that with RF waveforms for PAPR of several dB, the overall transmit power is at least the amount of PAPR less than the P_{sat}. The main trend the literature shows is that, when going higher in frequency, the power delivery capabilities decrease. There are multiple reasons for that, rising from the capabilities of the transistor technologies often measured in terms of maximum power gain and oscillation frequencies, f_T and f_{max} [54], as well as the limitations of the physical size of the circuits that need to be fitted under a limited antenna area. Moreover, with a large number of antennas, the power generation can be divided into multiple paths, thus reducing the required power per PA. Based on the analysis performed in [52], the estimated P_{sat} of four different circuit technologies, i.e., CMOS, SiGe, GaN, and InP, are collected in Table 5 for three different frequencies: 40 GHz, 140 GHz, and 240 GHz. The main observation is that the power delivery capabilities depend highly on the technology, which leads to a trade-off between cost, reliability, and performance. For example, we can see

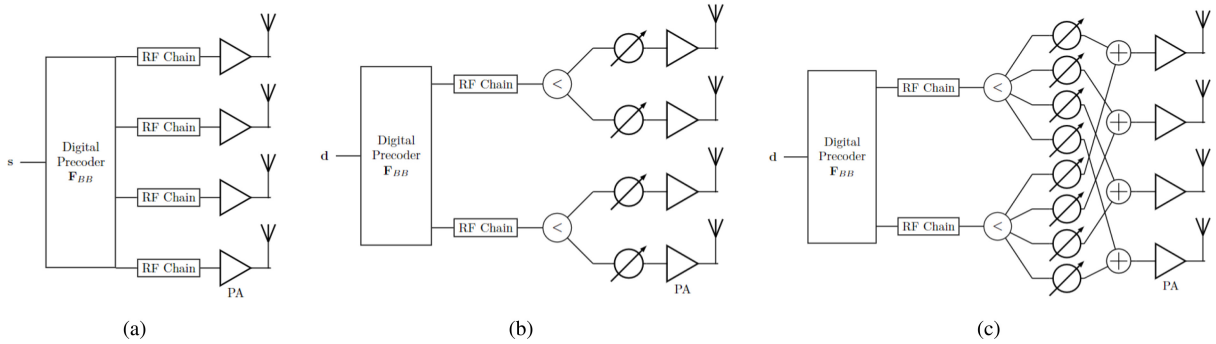

FIGURE 18. [Section IV-B] MIMO architecture options: (a) fully digital; (b) hybrid partially connected; (c) hybrid fully connected. RF chains refer to front-end components generating RF signals before their distribution to the different antennas.

TABLE 6. [Section IV-A.2] estimated minimum NF of different LNA technologies in different frequencies.

f \ Technology	CMOS	SiGe	GaAs	InP
40 GHz	2.4 dB	2.4 dB	1 dB	1.9 dB
140 GHz	5.2 dB	5.1 dB	2.1 dB	3.1 dB
240 GHz	12.6 dB	11.0 dB	4.4 dB	5.4 dB

that, by using the best technology (InP) to realize the PAs at 140 GHz, the output power can be even 9 dB better than using silicon-based technologies such as SiGe. On the contrary, InP can be roughly said to be two to three times more expensive than SiGe and has a lower integration rate. Such observations give significant motivation for merging multiple different technologies within the same package by using heterogeneous integration [57].

2) LNA NOISE FIGURE

The LNA's task in the wireless receiver is to amplify the signal to the next stages with minimal degradation in the SNR. In addition to good NF, the gain is important in order to minimize the SNR degradation in the subsequent RF components in the chain. At higher carrier frequencies, both of these are challenging to achieve. The main reasons for that are the smaller gain per stage of the circuit technologies combined with the high losses, especially in interfacing the components and amplifier stages. In addition to these, the circuit needs to be realized in a small form factor similar to PAs, in order to fit the circuits in a footprint with a size comparable to the antenna elements.

Models for frequency scalable LNA NF of different circuit technologies are derived in [118]. The estimated NF of CMOS, SiGe, GaAs, and InP at 40 GHz, 140 GHz, and 240 GHz are collected in Table 6. The clear trend is the increased NF as a function of the carrier frequency. The difference of best circuit technologies becomes clear when going toward 140 GHz and further. To the overall receiver NF, one should add even 1–3 dB from the RF front-end losses, in addition to a few more dB from the post-LNA components. This easily leads to realized NFs close to 10 dB at 140 GHz.

B. ENERGY EFFICIENCY OF SUB-THZ TRANSCEIVER ARCHITECTURES AND RELATED OPTIMIZATION TRADE-OFFS

Sub-THz communication systems rely on architectures containing a large number of antennas to compensate for the limited aperture of individual antenna elements. This is also easier to integrate within small dimensions as antennas scale with the wavelength. However, more antennas means more RF front ends and more PAs, which can both increase the system's power consumption [53], [119]. Additionally, the large bandwidth exploited at these frequencies can lead to a large DSP complexity and hence power consumption. In order to optimize the overall energy efficiency, it is thus necessary to optimize the architecture by carefully selecting the number of antennas and the related PA output power level based on the required link budget. It is also essential to select the proper hybrid architecture in order to jointly consider analog and digital power consumption for a given system's performance.

Figure 18 illustrates three architecture templates for the transmitter side; similar options exist for the receiver side. The fully digital offers the most flexibility and highest performance, but requires as many ADCs/DACs and digital signal processing chains as the number of antennas. The hybrid partially connected is the simplest but offers a more reduced array gain as individual streams are not connected to all the antennas. Lastly, the hybrid fully connected offers the full array gain with reduced digital complexity, but requires more phase shifters and splitters/combiners.

The optimization starts from the link budget determining the feasible configurations for the target scenario. It considers various QAM constellations with different low-density parity check (LDPC) coding rates, considering a PA back-off of 0 dB for binary/quadrature PSK, 3 dB for 16-QAM, and 6 dB for 64-QAM. These values are found to give an acceptable distortion (limited SNR increase needed) even using orthogonal frequency-division multiplexing (OFDM). Extra implementation losses of 5 dB are included to account for, e.g., imperfect channel estimation, hardware impairments, distortion, and interference. 12.5% of the available

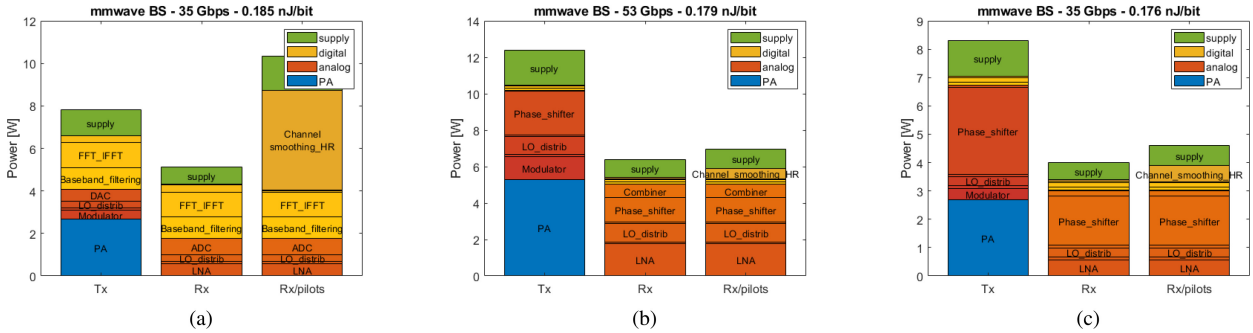

FIGURE 19. [Section IV-B] Power consumption of optimized medium hotspot architectures: (a) fully digital; (b) hybrid partially connected; (c) hybrid fully connected.

time/frequency resources are reserved for guard band and cyclic prefix (CP). After checking the link budget, the power consumption of all the configurations providing a sufficient throughput is estimated, using a power model including digital, analog, PA and power supply consumption based on [120] and [121]. Whenever the available throughput is larger than the application requirements, duty-cycling is assumed in order to maintain an optimum energy efficiency by deactivating the system between data bursts.

Results are simulated for three hotspot scenarios, i.e., small, medium, and large, respectively with a range of 10 m, 30 m, or 100 m, a BS height of 3 m, 5 m, or 10 m, a number of simultaneously served UEs of 10, 32, or 120 (in the last case, the UEs are split into three sectors with 40 UEs each), and with 2, 4, or 8 UEs spatially multiplexed (time/frequency multiple access is used additionally for extra UEs). The maximum number of antennas is 64, 256, or 1024, respectively, and the element gain is 2 dBi except for the largest hotspot where 4 dBi gain elements are used thanks to sectorization. The UEs are located at 1 m height and are equipped with a maximum of 16 antennas with 2 dBi element gain. A bandwidth of 5 GHz at 140 GHz is assumed along with a maximum PA output power of 18 dBm considering InP PA technology. Based on [121] output power levels above 15 dBm lead to reduced efficiency. Digital technology is extrapolated to a 2-nm CMOS node. The required throughput is 1 Gbps per UE. Lastly, LoS propagation is assumed, which is realistic at the considered frequencies.

For the small and the medium hotspots, all three architectures can provide a similar energy efficiency when properly dimensioned, i.e., 0.03 nJ/bit for the small hotspot and 0.18 nJ/bit for the medium one. However, they use different parameters. For the small hotspot, they always achieve 26 Gbps and use 4 antennas only, with 12 dBm PA for fully digital and hybrid fully connected architectures, and 14 dBm in the hybrid partially connected case. For the medium hotspot, the fully digital achieves 35 Gbps with 32 antennas and 14 dBm, the hybrid partially connected 53 Gbps with 100 antennas and 12 dBm, and the hybrid fully connected 35 Gbps with 64 antennas and 14 dBm.

Figure 19 illustrates the power consumption of the three optimized architectures in three communication states: transmit, receive and receive pilots (for uplink channel estimation, performed less frequently). Fully digital architectures are logically dominated by digital power consumption, while they benefit from a reduced number of front-end and PA components. The other two architectures are dominated by front-end and PA components, with a more prominent role of phase shifters for the hybrid fully connected architecture.

For the case of large hotspots spatially multiplexing 8 UEs per sector, the optimized fully-digital architecture is the best, achieving 0.24 nJ/bit (using 64 antennas) while the two hybrid architectures consume 0.32 nJ/bit (with 160 antennas for the partially connected and 64 antennas but a large penalty from phase shifters for the fully connected). All three optimal architectures use 14 dBm PA output power and achieve 57 Gbps/sector.

Although all three architectures achieve similar energy efficiency, each of them is more than 10 times more efficient than the baseline setup considering the maximum number of antenna allowed for the considered hotspot and the maximum 18 dBm PA output power (not shown here). Proper dimensioning is hence crucial and needs to be adapted to the target scenario in order to prevent both insufficient performance and overdesign. Power consumption modeling enables architecture optimization in energy efficiency and also gives insights into which components dominate the power (digital, analog, or PA).

C. IMPLICATIONS OF EMF EXPOSURE LIMITS ON SUB-THZ COMMUNICATIONS

Science-based RF EMF exposure limits up to 300 GHz have been developed by the ICNIRP, which is formally recognized by the World Health Organization. These limits are based on reviews of the relevant scientific literature and are set with large margins to protect against substantiated health effects, which are related to excessive tissue heating. The ICNIRP guidelines from 1998 [122] are adopted in most countries and form the basis of both the European Council Recommendation [123], which provides recommended EMF limits for the general public, and the EU Directive [124], which specifies EMF limits for workers. In 2020, the ICNIRP published updated guidelines [42] that consider the latest available scientific information and data. The limits in the

TABLE 7. [Section IV-C] EMF exposure limits between 6 and 300 GHz for the general public according to the 2020 ICNIRP guidelines [42]. The EMF exposure limits for occupational exposure is five times those for the general public. For brief exposure with averaging time less than 6 min, additional limits are applicable in the 2020 ICNIRP guidelines [42]. S_{ab}: absorbed power density. S_{inc}: incident power density. SAR_{WB}: whole-body specific absorption rate (SAR).

	Limit value	Averaging time	Notes
Basic restriction (local exposure)	$S_{\mathrm{ab}} = 20$ W/m^2	6 min	S_{ab} must be averaged over a square 4 cm^2 surface body area. A further constraint is imposed above 30 GHz such that the exposure averaged over a square 1 cm^2 surface body area cannot exceed twice that of the 4 cm^2 restriction.
Reference level (local exposure)	$S_{\mathrm{inc}} = 55/f_{\mathrm{G}}^{0.177}$ W/m^2	6 min	f_{G} is the frequency in GHz. S_{inc} must be averaged over a square 4 cm^2 area. For frequencies between 30 and 300 GHz, the exposure averaged over a square 1 cm^2 projected body surface space must not exceed twice that of the square 4 cm^2 restriction.
Basic restriction (whole body exposure)	$SAR_{\mathrm{WB}} = 0.08$ W/kg	30 min	SAR must be averaged over the whole body mass.
Reference level (whole body exposure)	$S_{\mathrm{inc}} = 10$ W/m^2	30 min	S_{inc} must be averaged over the whole-body space.

new guidelines are largely the same as those from 1998. The 2020 ICNIRP limits have already been adopted in several national regulations, and the Council Recommendation as well as the EMF Directive are expected to be updated based on the new guidelines in the coming years. Radio equipment and devices for 6G will need to comply with the same EMF requirements as the previous generations of mobile technologies.

In the 2020 ICNIRP guidelines [42], the basic restrictions, which are metrics evaluated inside body tissues, are specified in terms of the absorbed power density and whole-body SAR for local exposure and whole-body exposure, respectively, above 6 GHz. A more practical way to demonstrate EMF compliance in free space is to use the so-called reference levels, which are specified in terms of incident power density. The EMF limits above 6 GHz specified in the 2020 ICNIRP guidelines are shown in Table 7. Note that EMF exposure limits are time-averaged. Compliance with EMF limits can be shown using either basic restrictions or the reference levels. Basic restrictions are typically used to demonstrate compliance in the reactive near field of the antennas. Compliance should be determined for both local exposure limits and whole-body exposure limits, while UEs are usually exempt from whole-body exposure assessments by applying low-power exemption criteria [125].

To assess the conformity with the requirements related to EMF exposure, products are tested according to relevant EMF standards. For example, the international standard IEC 62232 [126] specifies methods and procedures to determine EMF compliance boundaries, i.e., exclusion zones, of the BSs. The international standards for assessing absorbed power density and incident power density for the UEs are addressed in the IEC/IEEE 63195 series [127], [128], [129], [130]. With this in mind, we analyze the EIRP levels of sub-THz systems and compare them with sub-6 GHz and FR2 systems.

Implications on sub-THz BSs: In [9], to achieve 10–100 Gbps data rates in the downlink at a distance around 80 m, sub-THz BSs with 512 transmit antennas should provide EIRP levels of 55.6–65.6 dBm. Assuming a time-division duplex downlink duty cycle of 75%, the EIRP levels of such sub-THz BSs are similar to those of existing micro cell and street coverage deployments, resulting in maximum compliance distances in the range of 1.5–4.7 m for theoretical maximum exposure conditions. When establishing EMF compliance boundaries according to the actual maximum condition [126], a power reduction factor should be introduced to account for the effects of beam scanning on the time-averaged EIRP. For a typical FR2 BS, this value is ≤ 0.14 [131], [132]. If the same factor is applied at sub-THz frequencies, the resulting compliance distance is reduced to 0.6–1.7 m, comparable to that of today's FR2 BSs.

Implications on sub-THz UEs: Compliance with the EMF limit constrains the transmit power levels of the UEs. References [133] and [134] investigated the implications of the EMF limits on maximum transmit power and EIRP levels of UEs above 6 GHz at the beginning of the 5G rollout. In [134], the maximum transmit power and EIRP levels for different sizes of antenna array configurations were analyzed up to 100 GHz using incident power density. Similar studies are needed for sub-THz UEs as input for link budget studies, uplink coverage analysis, and 6G systematization. If a device can transmit on different bands simultaneously, e.g., above and below 6 GHz, the cumulative EMF exposure for all the bands needs to be addressed by compliance testing.

D. SECTION SUMMARY

The two key parameters for the sub-THz link budget are the transmit power and receiver NF. To address these, we analyzed the capabilities of key circuit technologies focusing on the PA P_{sat} and LNA NF in Section IV-A. If only one technology is used for the entire RF front end, InP can give superior performance compared with the silicon-based technologies, providing around 29 dBm P_{sat} and 3.1 dB NF at 140 GHz. However, given the current performance of

different technologies, it is challenging to find a good techno-economical compromise to achieve the best PA NF and PA P_{sat} with the same technology. This increases the interest for the so-called heterogeneous integration, where multiple technologies can be integrated into the same package.

The RF components need to be then mapped to a realistic implementation of a multi-antenna transmitter. Different transceiver architectures are possible at sub-THz frequencies, e.g., fully digital, hybrid partially-connected, or hybrid fully-connected. However, based on the analysis presented in Section IV-B, there is no one-fits-all solution. Depending on the use cases (maximum array size, bandwidth, number of UEs, and others), one or the other may be more suitable. Nevertheless, the most critical aspect is to properly dimension the selected architecture based on the target link budget. Optimizing the number of RF front ends and the maximum PA output power accordingly has a huge impact on the overall energy efficiency. When carefully dimensioning the components and architecture, the specific energy consumption can be reduced to 0.2 nJ/bit for a large hotspot and 0.03 nJ/bit for a small one.

While the performance of the components limits the achievable transmit power, from another point of view, the maximum time-averaged power and EIRP are also constrained for the UE due to the EMF exposure limits. As for the BSs, the compliance distances are similar to those of today's FR2 BSs. These aspects are described in Section IV-C. Accordingly, the actual operation principles of future sub-THz systems must be taken into account when defining the parameters for the link budget and specifying transmitters for proper use, while also dimensioning the system for optimized energy efficiency in different scenarios.

V. PHY ENABLERS

The key challenges of operating at sub-THz frequencies are the increased effect of PN, reduced PA efficiency, and power consumption of the data converters, which all affect the system's throughput and coverage. In this section, we study suitable waveforms and modulations to compensate for these effects. We also present a fully digital MIMO system based on 1-bit ADCs/DACs to enable truly massive antenna arrays in the sub-THz range. In addition, we describe a ML-based context-aware receiver for PN compensation. Lastly, we study energy-efficient network deployments with hybrid beamforming in terms of throughput and energy efficiency.

A. WAVEFORMS AND MODULATIONS

In this section, we explore strategies to mitigate the challenges posed by the increased effect of PN and decreased PA efficiency in the sub-THz band through the selection of suitable waveforms and modulations. First, we study how well the current 5G NR waveforms are suited for sub-THz communications and propose evolutionary changes to the waveform selection and numerology. Then, we introduce novel PN-robust constellations, ZXM, and PCs to mitigate the challenges of sub-THz frequencies.

1) EVOLUTION OF 5G NR WAVEFORMS AND NUMEROLOGY

The current 5G NR specifications do not cover operation at sub-THz frequencies. Here, we discuss the changes needed in the 5G NR numerology, such as the SCS and CP length to support communications in the sub-THz band. We also address the performance differences between the waveforms already standardized for NR, namely cyclic prefix-orthogonal frequency-division multiplexing (CP-OFDM) and DFT-s-OFDM, in the presence of known hardware limitations specific for the sub-THz frequencies. This contribution addresses the challenges of *RF power consumption and complexity* as well as *hardware impairments* described in Sections II-B and II-C, respectively.

5G NR has been designed for scaled numerology, where the bandwidth and the frame structure (including the CP) scale according to the SCS as defined in Rel-15 [135]. This allows for straightforward and flexible alignment of different numerologies in both the time and frequency domains while enabling 5G operation in various scenarios. The current 3GPP numerology supports bands below 7.125 GHz (FR1) and up to 71 GHz (FR2-1 and FR2-2). For FR2-2, only a mandatory SCS of 120 kHz is specified, and 480 kHz and 960 kHz are optionally supported [1, Table V.3.5-1]. Considering the available bandwidth in the lower sub-THz frequencies, the potential bands in this region include the W-band, i.e., 75–110 GHz, and the D-band, i.e., 110–170 GHz [136]. The largest available bandwidth is in the D-band, spanning a total of 12.9 GHz within the 151.1–164 GHz range. With 264 physical resource blocks and 4096 inverse fast Fourier transform size, a SCS of 3840 kHz is capable of providing the occupied channel bandwidth of 12.17 GHz that fits the largest available band of 12.9 GHz in the D-band. However, the wider the SCS is, the shorter the symbols are in the time domain. This may not be a problem in terms of inter-symbol interference (ISI) since narrow beams lead to significantly reduced delay spreads. On the other hand, an insufficient CP may affect the beam-based transmission, especially if the beam switching delay is comparable to the CP length. Furthermore, increasing the SCS can significantly affect the system's design, leading to shorter scheduling periods and degraded coverage of the control channel [137].

CP-OFDM and DFT-s-OFDM are similarly affected by the PN distortion due to their orthogonal multicarrier nature. The PN is a major impairment at sub-THz bands since it increases by 6 dB when the carrier frequency is double using a frequency multiplier [138]. Hence, the current maximum supported SCS of 120 kHz may not be sufficient to mitigate the PN. Furthermore, the supported waveforms, namely CP-OFDM and DFT-s-OFDM, respond distinctly to different PTRS designs and PN compensation techniques. With this in mind, choosing the waveform and numerology is

challenging, especially with effective PN mitigation methods. In addition, 5G PTRS designs are also different between CP-OFDM and DFT-s-OFDM, where the former inserts the PTRS in the frequency domain and the latter in the time domain.

Besides the PN, a major drawback requiring consideration at sub-THz frequencies is the decreased PA efficiency at higher carrier frequencies. For instance, [139, Section 6.1.9.1] showed that the output power of the PAs degrades approximately by 20 dB/decade. This creates a strong demand for waveforms and modulations capable of achieving extremely low PAPR, allowing a higher average output power at the BS and UE. Consequently, the transmit power reaches its maximum level, impacting the coverage of the system. In this respect, CP-OFDM has larger PAPR than DFT-s-OFDM [138], especially with lower modulation orders, which motivates the deployment of DFT-s-OFDM in downlink and uplink for sub-THz communications. Depending on the modulation order, CP-OFDM demands an additional 3–5 dB output power back-off, implying that DFT-s-OFDM yields improved coverage [137].

In addition to CP-OFDM and DFT-s-OFDM, there are a plethora of candidate modulation schemes for the sub-THz band, including SC modulations and orthogonal time frequency space (OTFS). The properties of SC modulations at sub-THz frequencies have been studied extensively [140], and a comparison of single carrier with frequency-domain equalization (SC-FDE) with CP-OFDM and DFT-s-OFDM in the presence of hardware impairments can be found in [141]. As stated in this paper, a sub-THz system applying SC-FDE alone provides several advantages, such as high spectral efficiency, low PAPR, robustness to PN, and good tolerance toward ADC quantization, but inherently lacks frequency-domain multiplexing capability. In OTFS, the signal is represented in the so-called delay-Doppler domain [142]. The performance of OTFS under high Doppler effects is studied in [143]. Moreover, a comparison of CP-OFDM, DFT-s-OFDM, and OTFS according to the 5G NR numerology is given in [144], where the improved performance of OTFS in certain cases comes at the cost of increased equalization complexity [140].

The performance of CP-OFDM and DFT-s-OFDM is evaluated through link-level simulations, where the carrier frequencies are 140 and 300 GHz, the modulation is 64-QAM, and the SCSs are 120 kHz, 960 kHz, and 1920 kHz. For the PN model, we use the Hexa-X model given in [52]. The output power of the waveforms is modeled by compensating the DFT-s-OFDM SNR following the required output back-off model in [137]. In Figure 20, we observe that DFT-s-OFDM outperforms CP-OFDM in both carrier frequencies, with more considerable gains at 300 GHz. In this context, DFT-s-OFDM is capable of providing more output power and handles the PN more effectively. In addition, we note that the SCS of 960 kHz outperforms 1920 kHz for the 140 GHz carrier. The main reason is that

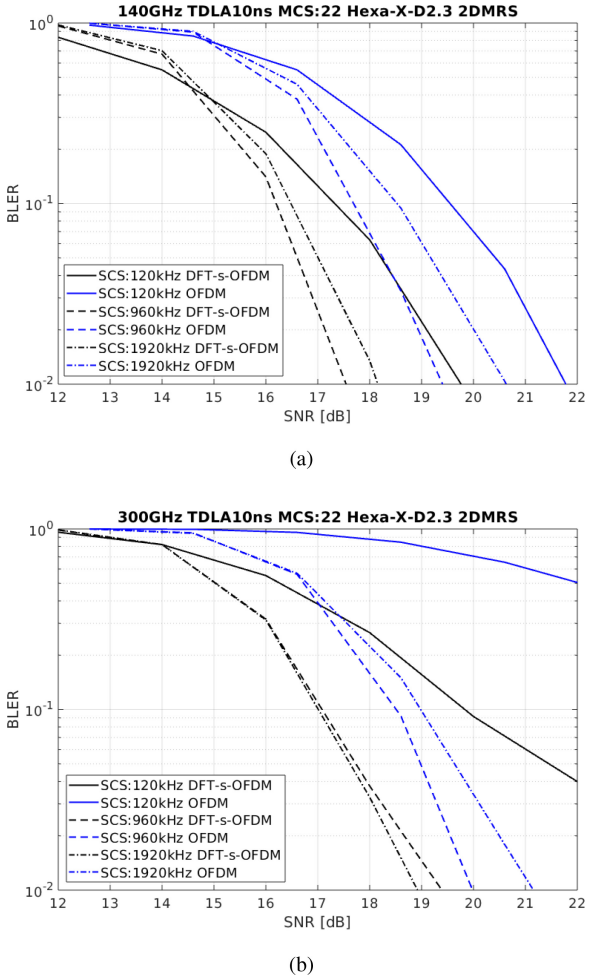

FIGURE 20. [Section V-A.1] Performance of CP-OFDM and DFT-s-OFDM, with 64-QAM, PN, and different SCSs [87]: (a) 140 GHz carrier; (b) 300 GHz carrier.

the CP starts to fall short on the highest SCS setting. In 300 GHz, the inter-carrier interference (ICI) introduced by PN affects the performance of 960 kHz SCS, while the larger 1920 kHz SCS suffers from the shortness of the CP, thus providing almost equal results.

The above discussion shows that, in addition to CP-OFDM, it would be very beneficial to support DFT-s-OFDM also for the downlink in sub-THz communications. DFT-s-OFDM yields better link performance under PN with minor modifications to the PTRS design of Rel-15. The DFT-s-OFDM waveform can also enable better coverage as it provides larger PA output power than CP-OFDM, especially with low-order modulations. For the overall numerology, it is also shown that SCSs of 960 kHz and 1920 kHz can provide a good baseline for sub-THz communications, allowing Tbps rates by supporting large bandwidths, and providing necessary enhancement in the PN mitigation for both CP-OFDM and DFT-s-OFDM waveforms. Although 3840 kHz SCS provides widest contiguous bandwidth still available in the W-band and D-band, insufficiently short CP may become a problem. Hence, a more conservative value of 960 kHz should be taken as a starting point for the

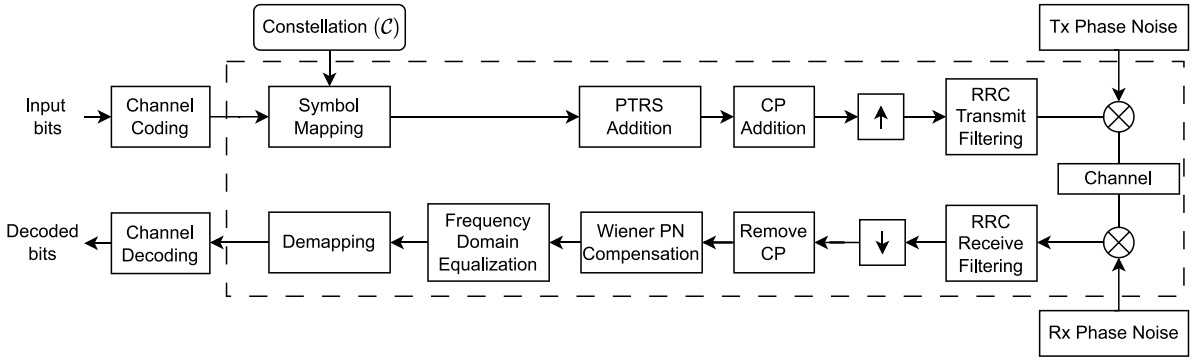

FIGURE 21. [Section V-A.2] End-to-end system model for the SC-FDE transceiver [145], [146].

first efforts to design a system's numerology for sub-THz communications.

2) PN-ROBUST CONSTELLATIONS UNDER PAPR CONSTRAINTS

PN becomes a major concern in the sub-THz range as described in Section II-C. The residual PN after compensation poses a major challenge for wideband sub-THz transmissions and some measures at the receiver will also be discussed in Section V-C. Different modulation constellations exhibit different robustness against the PN, especially to the residual or Gaussian PN. Furthermore, as described in Section II-B, the limited output power of integrated PAs imposes constraints on the achievable range of sub-THz communications. With this in mind, we focus on designing modulation constellations tailored for SC transmissions that are robust against residual PN, possess low PAPR, and are thus well-suited for sub-THz communications [145], [146]. This contribution addresses the challenges of *RF hardware consumption and complexity* as well as *hardware impairments* described in Sections II-B and II-C, respectively.

We assume a conventional SC-FDE transceiver as depicted in Figure 21, where both the transmitter and receiver are impaired by PN. The channel-coded data bits are first mapped to the modulation symbols based on a specific constellation design. After this mapping, the PTRSs required for PN compensation, along with CPs, are added to the signal. Following this, the generated signal is up-sampled and band-limited by the root-raised-cosine filter. At the receiver side, the PN-impacted signal is filtered and down-sampled. Subsequently, the channel distortion and PN, mainly the correlated Wiener PN part, are removed. The signal is then demapped and channel decoded to get the estimates of the transmitted data bits.

Following the system model depicted in Figure 21, we employ an end-to-end learning method, which uses large-scale back-propagation of gradients enabled by ML frameworks to shape the constellation to be robust to PN and possess a certain PAPR level. We use a trainable constellation, which can be modeled by a set of 2^K trainable complex weights $\tilde{\mathcal{C}}$, where K is the number of bits. The constellation $\mathcal{C}$ is defined as [147], [148]

$$\mathcal{C} = \frac{\tilde{\mathcal{C}} - \frac{1}{2^K}\sum_{c_i \in \tilde{\mathcal{C}}} c_i}{\sqrt{\frac{1}{2^K}|\tilde{\mathcal{C}} - \frac{1}{2^K}\sum_{c_i \in \tilde{\mathcal{C}}} c_i|^2}}. \tag{8}$$

Note that $\mathcal{C}$ is centered to avoid a center shift from the origin and normalized to have unit energy. The bit labeling is set by the binary value of the index of each element in $\mathcal{C}$. The bit-to-symbol mapping is performed as in standard constellations and thus no additional complexity is introduced at the transmitter. Furthermore, this enables the optimization of the constellation points and the corresponding bit labels. Throughout the training, the constellation points will reposition in the IQ plane to reach the optimization criteria. We formulate the constellation shaping problem as a constrained optimization problem that minimizes the binary cross entropy (BCE) loss between the transmitted bits and the soft estimates from the conventional additive white Gaussian noise (AWGN) optimal demapper, while constrained under a given PAPR target ϵ_P. The solution utilizes the augmented Lagrangian technique in solving such problems, which allows to reformulate the BCE loss and the PAPR constraint as a differentiable loss function. With the augmented Lagrangian, the constrained optimization problem is solved through a sequence of unconstrained problems via stochastic gradient descent. Then, the gradients are computed and back propagated through the system with respect to the constellation. Note that channel coding (5G NR LDPC) is not applied in the training phase but in the evaluation only.

Figure 22, depicts the simulation performance results under an AWGN channel condition reflecting a perfect equalization, since the focus is on the PN and PAPR. For comparison, we also show the BLER and PAPR performance of conventional rectangular 64-QAM and circular 64-amplitude and phase-shift keying (APSK) used in digital video broadcasting and satellite standard (DVB-S2) by European Telecommunications Standards Institute systems. It is evident that the waveforms employing the designed constellations comply with the target PAPR while delivering better BLER performance compared with the baselines.

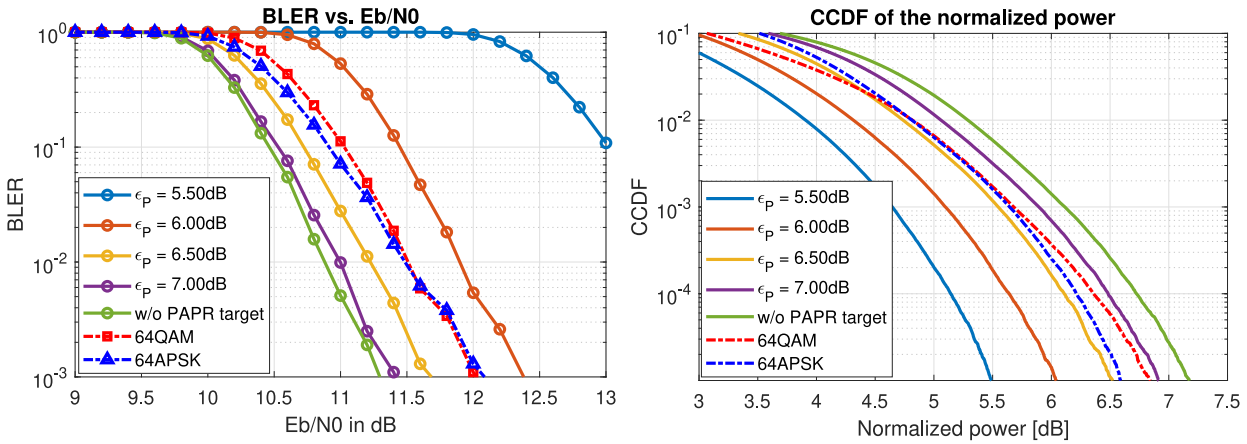

FIGURE 22. [Section V-A.2] block error rate (BLER) performance (left) and cumulative CDF (right) of the normalized power of the learned constellations [145].

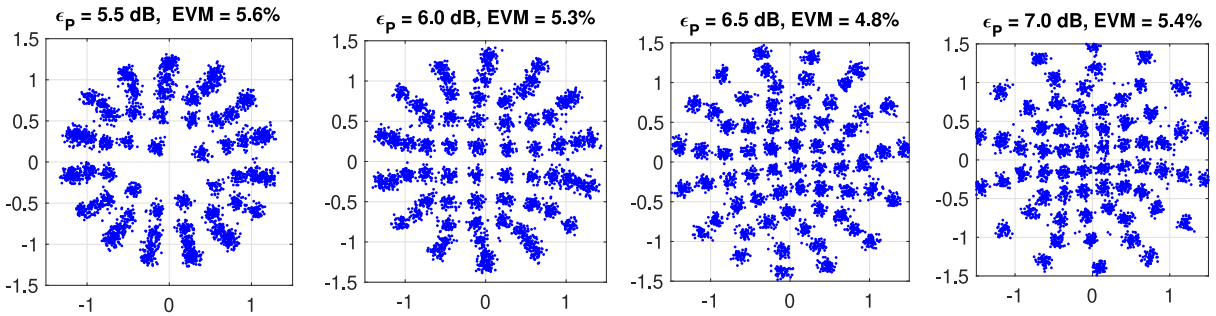

FIGURE 23. [Section V-A.2] Received signals in the proof-of-concept setup using the learned constellations for different ϵ_P targets [149].

Furthermore, it can be seen that, when the PAPR target is stricter, the price to pay is in the BLER performance [145].

The feasibility and performance of the designed constellations are further validated by transmitting test vectors, modulated using these constellation patterns, through a hardware system operating at sub-THz frequencies. This setup includes real-world practical sub-THz hardware, especially RF interference cancellation components tailored for operation in the D-band at 144 GHz, with a transmission bandwidth of up to 5 GHz [149]. The over-the-air transmitted signal is captured and processed offline applying the steps outlined in Figure 21. The results are depicted in Figure 23. The error vector magnitude (EVM) value for all the transmissions utilizing the designed constellations is well below 6% and the coded BER is smaller than 2×10^{-7} for the considered measurement duration.

3) ZERO-CROSSING MODULATION

The ADC challenge mentioned in Section II-B.1 and its implications require to rethink modulation design. Achieving minimum power consumption of the ADC involves minimizing the number of ADC bits to 1 bit. Even for SC schemes, adopting a 1-bit ADC limits known modulation schemes such as QAM that encode information in the amplitude of the signal. A 1-bit ADC operates by comparing the signal to a zero threshold and, thus, detects the temporal positions of crossings of the threshold, i.e., the zero-crossings.

This feature opens another opportunity: since only the zero-crossings are observable, the information is no longer encoded in the amplitude but in the time domain. This shift from amplitude to time domain is also advantageous to modern nm-scale CMOS digital circuits, where time-domain resolution is becoming superior to amplitude resolution, as less and less voltage headroom is available [150]. ZXM is a modulation scheme specifically designed for 1-bit quantization [151]. This modulation scheme employs faster-than-Nyquist (FTN) signaling at the transmitter, meaning transmitting M_{Tx} symbols within one Nyquist interval, as well as oversampling at the receiver, resulting in multiple samples per Nyquist period. runlength-limited (RLL) sequences are employed to manage the potential issue of ISI arising from FTN signaling and ensure effective communication. Originally designed for hard drives, these sequences play a crucial role in controlling ISI and ensure no more than one zero crossing occurs per Nyquist interval. A sketch of a ZXM signal is depicted in Figure 24. This contribution addresses the challenge of *RF power consumption and complexity (data converters)* described in Section II-B.1.

Aspects of the ZXM have been explored in various studies. Reference [152] evaluated the theoretical basics

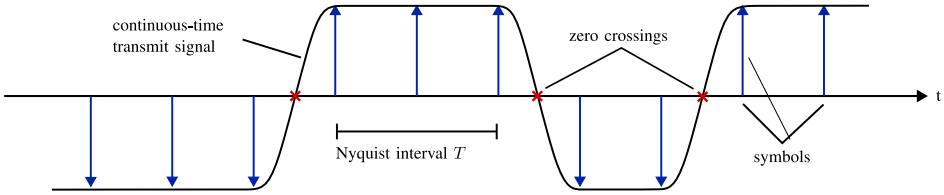

Faster-than-Nyquist (FTN) signaling
transmit M_{Tx} symbols per T (here $M_{\mathrm{Tx}} = 2$)

Runlength-limited (RLL) sequences
same amplitude for certain number of consecutive symbols

FIGURE 24. [Section V-A.3] Overview of ZXM.

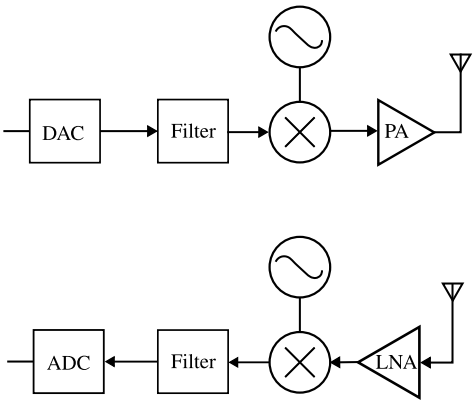

FIGURE 25. [Section V-A.3] Structure of typical transmit (top) and receive (bottom) RF front ends.

including achievable rates of ZXM, while [153] discussed practical implementation aspects including RLL encoding and decoding. Special care needs to be dedicated to channel estimation in ZXM systems, as conventional channel estimation algorithms are unsuitable due to the coarse quantization of the receive signal. Insights into estimation in ZXM systems were provided in works such as [154], where low-complexity timing and phase estimation algorithms are explored, and [155] where the tracking of PN under 1-bit quantization is considered. In the following, we concentrate on the energy efficiency of ZXM and compare it with the spectrally efficient QAM in the context of SC transmission. The analysis of the multi-carrier setting will be the subject of future work.

Evaluating the power consumption of ZXM and QAM transceivers requires a closer examination of the primary consumers in the RF front end. In Figure 25, the key components of a standard RF front end are considered with the assumption that filters and antennas work as passive components. The RF front-end components exhibit distinct dependencies on the system parameters, influencing their power consumption characteristics. For instance, the efficiency of the PA decreases with the carrier frequency f_{c} and its power consumption scales directly with the transmit power P_{T}. On the other hand, the power consumption of the LNA is dependent on the bandwidth B and the required gain G_{LNA}. Furthermore, the power requirements of the DAC and the ADC are influenced by their resolution b in bits and the system's bandwidth B. In contrast to these components, the power consumption of the mixer P_{Mix} and the LO P_{LO} exhibit a relatively constant power consumption but remain dependent on the carrier frequency f_{c} for which they are designed. Understanding these nuanced dependencies is crucial for comparing the power consumption of systems using different modulation schemes. The details are discussed in [156] for generalized linear amplitude modulations and in [157] for practical modulation schemes.

Following the analysis in [156] and [157], we obtain the expressions in (9)–(10) at the bottom of the page for the power consumption of the receiver, where Υ is the PAPR, and b_{ADC} and b_{DAC} denote the resolution of the ADC and DAC, respectively. The constants in (9) and (10) are given as $c_{\mathrm{DAC,stat}} = 1.5 \times 10^{-5}\,\mathrm{W}$ [158], $c_{\mathrm{DAC,dyn}} = 9 \times 10^{-12}\mathrm{Ws}$ [158], $c_{\mathrm{PA}} = 4.32 \times 10^{-5}\,\mathrm{Hz}^{-0.5}$ [156], and $c_{\mathrm{ADC}} = 0.67 \times 10^{-15}\,\mathrm{Ws}$, where $f_b = 560\,\mathrm{MHz}$ [49]. As there are no general expressions for the power consumption of the mixer and the LO, we are referring to literature based measurements in the sub-THz regime. Assuming a carrier frequency of $f_{\mathrm{c}} = 120$ GHz we can use the measurements from [159] and [160] for the LO and the mixer, i.e., $P_{\mathrm{LO}} = 44$ mW and $P_{\mathrm{Mix}} = 8$ mW. To compare the power consumption of ZXM and QAM, we minimize the energy per bit of both modulation schemes for a given data rate R. Then, we optimize over the bandwidth B and the transmit

$$P_{\mathrm{Tx}} \approx \underbrace{2c_{\mathrm{DAC,stat}}(2^{b_{\mathrm{DAC}}} - 1) \quad + 2c_{\mathrm{DAC,dyn}}\, b_{\mathrm{DAC}} B}_{\mathrm{DAC}} + \underbrace{c_{\mathrm{PA}} P_{\mathrm{T}} \sqrt{f_{\mathrm{c}}}\, \Upsilon}_{\mathrm{PA}} + P_{\mathrm{LO}} + P_{\mathrm{Mix}}, \tag{9}$$

$$P_{\mathrm{Rx}} \approx \underbrace{\frac{G_{\mathrm{LNA}} B N_0}{(N_{\mathrm{LNA}} - 1)\mathrm{FOM}_{\mathrm{LNA}}}}_{\mathrm{LNA}} + \underbrace{2c_{\mathrm{ADC}}\, 2^{b_{\mathrm{ADC}}} B \sqrt{1 + \left(\frac{B}{f_b}\right)^2}}_{\mathrm{ADC}} + P_{\mathrm{LO}} + P_{\mathrm{Mix}} \tag{10}$$

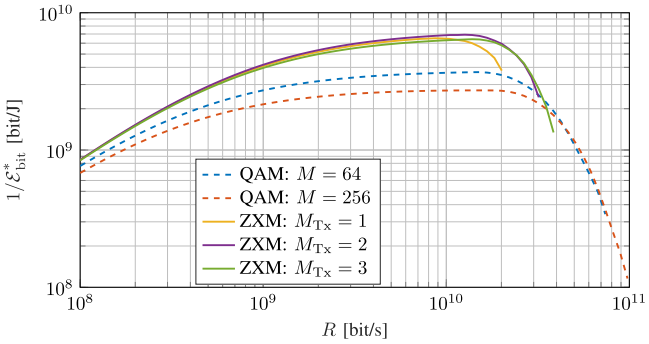

FIGURE 26. [Section V-A.3] Comparison of energy efficiency of ZXM and QAM. M describes the modulation order of QAM, while M_{Tx} describes the FTN signaling factor for ZXM. Parameters: path loss exponent $\beta = 2$, distance $d = 20$ m, antenna gain $G_{\text{Rx}} = G_{\text{Tx}} = 6$ dB, maximum transmit power $P_{\max} = 10$ W, maximum bandwidth $B_{\max} = 7$ GHz, receiver noise factor $F = 10$, $b_{\text{DAC}} = b_{\text{ADC}}$, $G_{\text{LNA}} = 15$ dB [163], $N_{\text{LNA}} = 5$ dB [163], $\text{FOM}_{\text{LNA}} = 10^{-7}$ [164].

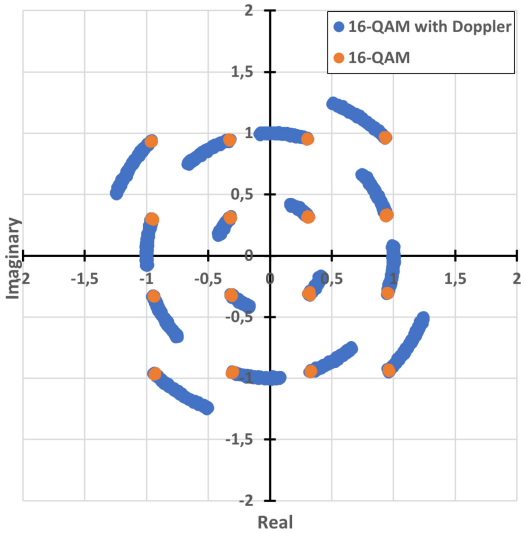

FIGURE 27. [Section V-A.4] Effect of phase rotation induced by the Doppler shift on a classical 16-QAM constellation.

power P_{T} and, hence, the SNR. This optimization problem is formally denoted by

$$\underset{B,P_{\text{T}}}{\text{minimize}} \quad \mathcal{E}_{\text{bit}} = \frac{P_{\text{Tx}} + P_{\text{Rx}}}{R} \tag{11a}$$

$$\text{s.t.} \quad R = B\,S \tag{11b}$$

$$0 \le P_{\text{T}} \le P_{\max} \tag{11c}$$

$$0 \le B \le B_{\max}, \tag{11d}$$

where $B_{\max}$ is the maximum available bandwidth, $P_{\max}$ is the maximum allowed transmit power, and S is the spectral efficiency. The spectral efficiency of QAM is calculated by analytical methods for AWGN channel. Assuming hard demapping for minimal ADC resolution, we set the ADC resolution for each the in-phase and quadrature phase to $b_{\text{ADC}} = \log_2(\sqrt{M})$ for QAM, where M describes the constellation size. In contrast, the spectral efficiency of ZXM cannot be evaluated analytically due to the nonlinear 1-bit quantization. Consequently, we rely on results from [161], where the spectral efficiency of ZXM is determined through a numerically evaluated auxiliary channel lower bound [162].

Furthermore, the frequency-dependent path loss is considered to achieve realistic results. To establish a baseline, isotropic antennas are often employed, although path loss heavily relies on the actual antenna design. We turn to the well-known standard path loss model represented by

$$P_{\text{Loss}} = \frac{P_{\text{T}}}{P_{\text{R}}} = \frac{1}{G_{\text{Rx}} G_{\text{Tx}}} \left(\frac{4\pi d}{\lambda}\right)^{\beta}, \tag{12}$$

where d denotes the distance between the transmitter and receiver, $\beta > 0$ stands for the path loss exponent (typically $2 \le \beta \le 4$ for outdoor environments), $\lambda = \frac{c}{f_{\text{c}}}$ represents the wavelength, where c is the speed of light, and G_{Tx} and G_{Rx} denote the antenna gains of the transmit and receive antennas, respectively. Further, we consider a receiver noise factor F that realistically enhances the noise level in the receiver and consider the PAPR for each configuration of ZXM and QAM. Solving the resulting optimization problem in (11) using (9)–(10) and (12) results in the energy efficiencies displayed in Figure 26. It is observed that ZXM has significantly better energy efficiency in higher data rates, thus making it suitable for sub-THz communications.

4) POLAR CONSTELLATIONS

For over 20 years, OFDM has become established in various standards such as 5G, WiFi, and DVB-T. The success of this multi-carrier waveform is linked to its: i) robustness to frequency selective channels, ii) spectral confinement, iii) frequency access flexibility, and iv) compatibility with MIMO systems. At high frequencies such as sub-THz, OFDM can still be used, but conventional M-QAM constellations are not optimal for withstanding the PN generated by oscillators or Doppler shift [165], [166], [167]. Doppler shift arises from relative motion between the transmitter and receiver, and can also result from frequency mismatches between their LOs. Doppler shift introduces a frequency offset that leads to a time-varying phase rotation of the constellation points, causing a degradation in the data detection performance. Figure 27 illustrates this phenomenon in a classical 16-QAM constellation. With this in mind, we propose a new modulation scheme, referred to as PC, to overcome the phase rotation induced by the Doppler shift. PCs map each symbol with $s(i) = a_i e^{j\theta_i}$, which allows infinite combinations of amplitude a_i and phase θ_i in polar coordinates. The general idea is to provide a distinct amplitude for each constellation point, thus enabling phase-invariant constellation points and robustness to common phase error (CPE). This contribution addresses the challenge of *hardware impairments* described in Section II-C.

A compromise must be found between robustness to the Doppler shift and AWGN. To solve these issues, we present two solutions: 16-Spiral and 16-PC. In 16-Spiral, each constellation point has its own amplitude as depicted in Figure 28. 16-Spiral is highly robust to the Doppler shift, but it is limited by the interference power among the OFDM

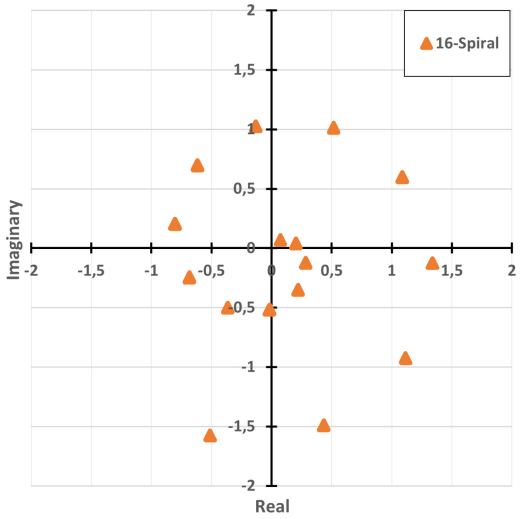

FIGURE 28. [Section V-A.4] Illustration of 16-Spiral.

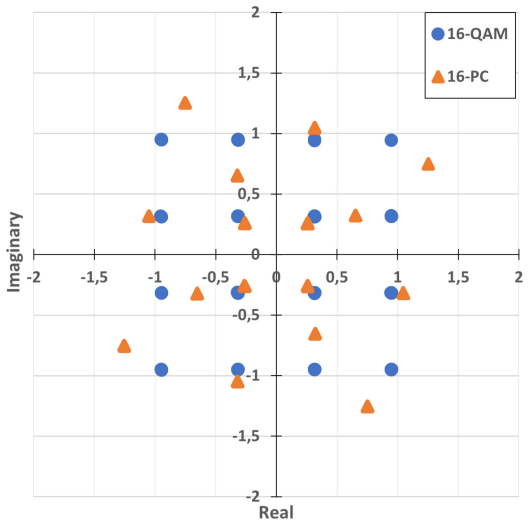

FIGURE 29. [Section V-A.4] Comparison between 16-PC and classical 16-QAM.

subcarriers. Furthermore, as illustrated in Figure 29, 16-PC is similar to 16-QAM in terms of coordinates of the constellation points, which ensures robustness to AWGN and a limited sturdiness to phase variations equivalent to one quadrant, i.e., $\pm\pi/4$. For spiral constellations, a scrambling operation is applied before OFDM to reduce the PAPR due to polar coordinate asymmetry. To do so, we generate a pseudo-random sequence by shifting the registers as illustrated in Figure 30. This dual operation has to be carried out at the receiver side without impacting the performance with low complexity.

At the multi-carrier receiver (OFDM-type), one processing must be included to evaluate the CPE. By measuring the amplitude of the received point, it is possible to estimate the transmitted point and thus calculate the phase difference between the transmitted and received points, which corresponds to the CPE. The average over all useful subcarriers

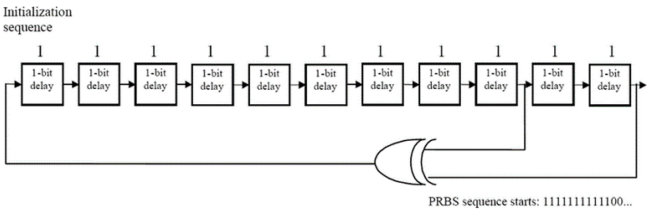

FIGURE 30. [Section V-A.4] Example of a random sequence generator.

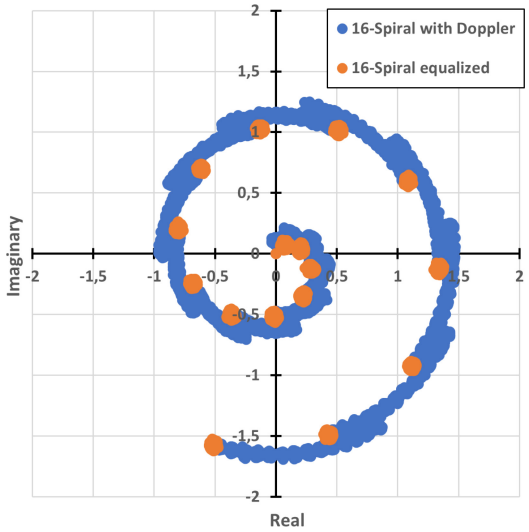

FIGURE 31. [Section V-A.4] 16-Spiral with Doppler shift and 16-Spiral equalized.

gives an accurate estimate of the CPE, defined as

$$\Delta\theta = \frac{1}{N_c}\sum_{i=1}^{N_c}\Delta\theta_i, \tag{13}$$

where N_c is the number of OFDM subcarriers used to estimate the phase variations and $\Delta\theta_i$ indicates the phase error between the transmitted and received OFDM signal in the i-th subcarrier. With PCs, the phase error estimation does not require any additional pilots; this corresponds to so-called blind estimation. Figure 31 illustrates the effect of phase error on a 16-Spiral constellation and the result of the equalization of the same constellation at the receiver side. Variations in the CPE from one OFDM symbol to another are directly linked to the Doppler shift, so it is possible to evaluate the main component of this Doppler shift and make a correction in the time domain, thus reducing the interference between subcarriers and improving the system's performance.

Figure 32 illustrates the block diagram for evaluating the proposed PCs with OFDM waveform. For this simulation, we adopted 5G's LDPC encoder, OFDM waveform with 2048 subcarriers and 15 kHz of SCS, and the previously described CPE detector. Moreover, the Doppler shift is generated in the time domain and appended to the channel as $e^{-2j\pi\upsilon_l t}$, where $\upsilon_l = f_c v/c$ represents the Doppler frequency, f_c is the carrier frequency, v the UE's mobility, and c the speed of light. Figure 33 illustrates the performance

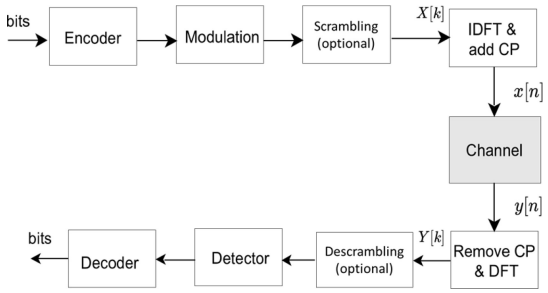

FIGURE 32. [Section V-A.4] Simulation chain for evaluating PCs.

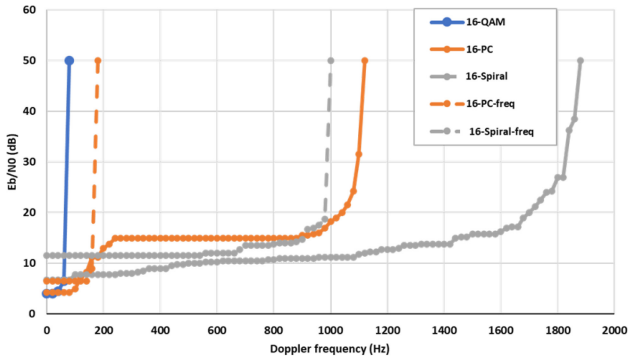

FIGURE 33. [Section V-A.4] Comparison of different constellations with respect to Doppler shift for a BER of 5×10^{-5} [87].

of 16-QAM, 16-PC, and 16-Spiral with frequency or time equalization for the PCs and applying Doppler shift variation. Here, 16-PC-freq corresponds to 16-PC equalized in frequency by the factor defined in (13). The performance is assessed through E_b/N_0 measurements for a given Doppler shift to achieve a target BER of 5×10^{-5} after LDPC decoding (8192 bits, coding rate 0.5). The results show the benefits of time-corrected Doppler shift, both in terms of the E_b/N_0 required to achieve a target BER of 5×10^{-5}, and in terms of Doppler robustness limits. Especially, 16-Spiral leads to the best Doppler performance with significant gains compared with the classical 16-QAM.

B. MASSIVE MIMO WITH 1-BIT DATA CONVERTERS

The implementation of truly massive antenna arrays suitable for sub-THz communications requires radical simplifications in terms of RF architecture. To enable communications in the low mmWave spectrum (up to 52.6 GHz), 5G NR systems have initially adopted hybrid analog-digital arrays [138], [168], obtained by severely reducing the number of RF front ends with respect to the number of antennas [169]. This approach, however, results in limited spatial multiplexing and does not scale well at higher frequencies and wider bandwidths due to the complexity of the additional analog circuitry and the resource-intensive beam management schemes required [170].

To enable versatile wideband beamforming and extensive spatial multiplexing, it is crucial to adopt fully digital architectures consistent with the original idea of massive MIMO systems [171], [172], [173]. Sacrificing the resolution of the ADCs/DACs is inevitable when operating with large bandwidths and massive antenna arrays, since the power consumption of each ADC/DAC increases at least linearly with the sampling rate and exponentially with the number of resolution bits [47], [48], [174]. Remarkably, despite the added quantization distortion, fully digital massive MIMO systems equipped with 3- to 5-bit ADCs/DACs can nearly match the performance of their unquantized versions [48], [175]. In addition, fully digital arrays with lower-resolution data converters (even as low as 1 bit) can vastly outperform hybrid analog-digital architectures in terms of beamforming flexibility and spectral/energy efficiency [50].

1-bit ADCs/DACs are especially appealing thanks to their minimal power consumption [47], [176]. Therefore, they can be easily deployed in very large numbers to create massive arrays at the transmitter, receiver, or both, which are essential for operating at sub-THz frequencies. 1-bit ADCs/DACs relax the requirements for high-cost RF components such as highly linear amplifiers and automatic gain controls, and enable very high energy efficiency since the power amplifiers at the transmitter side can operate without back-off. Consequently, the inherent performance degradation caused by the 1-bit quantization can be mitigated by incorporating highly cost-effective antennas and RF front ends. Additionally, combining 1-bit ADCs/DACs with the short wavelength in the sub-THz band enables the development of compact and energy-efficient massive MIMO arrays, which can also be deployed at the UE side (for example, on cars and unmanned aerial vehicles). Lastly, adopting 1-bit ADCs/DACs allows to drastically reduce the volume of raw data exchanged between the radio unit and the baseband processing unit [48], [174], [177].

Over the past decade, massive MIMO systems with low-resolution and 1-bit data converters have garnered significant attention in terms of performance analysis [47], [48], [50], [51], [175], [176], [178], [179], channel estimation [47], [180], [181], [182], [183], [184], [185], data detection [180], [181], [184], [186], [187], [188], [189], [190], and precoding design [170], [174], [177], [191], [192], [193]. In the literature, coarse quantization is generally assumed at the BS, i.e., either at the transmitter or receiver. The extreme case in which both the transmitter and receiver have fully digital massive MIMO arrays and 1-bit ADCs/DACs is analyzed in [194]. Integrating 1-bit ADCs and DACs yields a fully digital system with minimum RF power consumption, complexity, and cost. While systems using slightly higher-resolution data converters (e.g., with 2–5 bits) can offer better performance in terms of spectral efficiency, they also introduce higher power consumption and hardware complexity, which limits their scalability. In contrast, 1-bit ADCs/DACs represent an extremely practical solution that strikes an ideal balance between performance, energy efficiency, and implementation feasibility, particularly at sub-THz frequencies. Their binary nature simplifies circuit

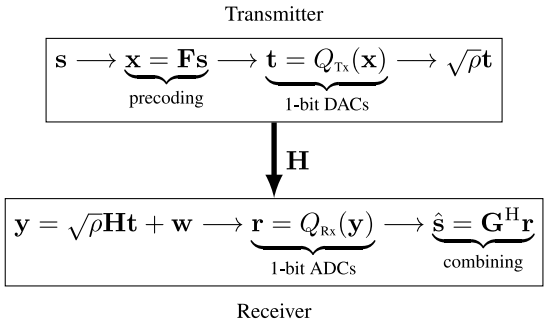

FIGURE 34. [Section V-B] Diagram of the considered massive MIMO system with 1-bit ADCs/DACs [194].

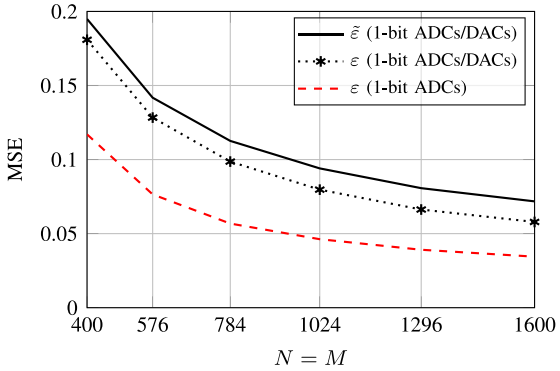

FIGURE 35. [Section V-B] MSE for 1-bit ADCs/DACs and 1-bit ADCs against number of transmit/receive antennas, with $K = 16$ and $\rho = 10$ dB [194].

design, minimizes raw data exchange, and facilitates ultra-fast and low-power processing, features that are essential for enabling affordable, compact, and high-performance massive MIMO deployments. Given these premises, we focus on 1-bit data converters in the following. This contribution addresses the challenge of *RF power consumption and complexity (data converters)* described in Section II-B.1.

Consider the point-to-point MIMO system illustrated in Figure 34, where a N_{Tx}-antenna transmitter with 1-bit DACs transmits K data streams to a N_{Rx}-antenna receiver with 1-bit ADCs, where the number of data streams is constrained as $K \leq \min(N_{\text{Tx}}, N_{\text{Rx}})$. Define the 1-bit quantization function $Q_{\text{B}}(\mathbf{a}) = \sqrt{\frac{\eta_{\text{B}}}{2}}(\text{sgn}(\text{Re}[\mathbf{a}]) + j\,\text{sgn}(\text{Im}[\mathbf{a}]))$ for a given input $\mathbf{a}$, with $\text{B} = \text{Tx}$ for the transmitter and $\text{B} = \text{Rx}$ for the receiver. The transmitter sends the data symbol vector $\mathbf{s} \in \mathbb{C}^{K\times 1}$. Adopting a quantized linear precoding strategy, $\mathbf{s}$ is precoded as

$$\mathbf{x} = \mathbf{F}\mathbf{s} \in \mathbb{C}^{N_{\text{Tx}}\times 1}, \tag{14}$$

where $\mathbf{F} \in \mathbb{C}^{N_{\text{Tx}}\times K}$ denotes the linear precoder. After the 1-bit DACs, the analog signal

$$\mathbf{t} = Q_{\text{Tx}}(\mathbf{x}) \in \mathbb{C}^{N_{\text{Tx}}\times 1} \tag{15}$$

is obtained, which is transmitted over the channel $\mathbf{H} \in \mathbb{C}^{N_{\text{Rx}}\times N_{\text{Tx}}}$ with transmit power ρ. The signal at the receiver is

$$\mathbf{y} = \sqrt{\rho}\mathbf{H}\mathbf{t} + \mathbf{w} \in \mathbb{C}^{N_{\text{Rx}}\times 1}, \tag{16}$$

where $\mathbf{w} \sim \mathcal{CN}(\mathbf{0}, \mathbf{I}_{N_{\text{Rx}}})$ is a vector of AWGN. After the 1-bit ADCs, the digital signal

$$\mathbf{r} = Q_{\text{Rx}}(\mathbf{y}) \in \mathbb{C}^{N_{\text{Rx}}\times 1} \tag{17}$$

is obtained. Finally, the receiver derives a soft estimate of $\mathbf{s}$ as

$$\hat{\mathbf{s}} = \mathbf{G}^{\text{H}}\mathbf{r} \in \mathbb{C}^{K\times 1}, \tag{18}$$

where $\mathbf{G} \in \mathbb{C}^{N_{\text{Rx}}\times K}$ denotes the linear combiner.

In [194], the relation between the transmitted data symbol vector $\mathbf{s}$ and the soft estimate $\hat{\mathbf{s}}$ is characterized using the Bussgang decomposition, which is used to reformulate each quantization step as a linear function with the same first- and second-order statistics [195]. Assuming $\mathbf{s} \sim \mathcal{CN}(\mathbf{0}, \mathbf{I}_K)$ and perfect channel state information, the mean squared error (MSE) between the transmitted data symbol vector and its soft estimate, defined as $\varepsilon = \frac{1}{K}\mathbb{E}_{\mathbf{s},\mathbf{w}}[\|\mathbf{s} - \hat{\mathbf{s}}\|^2]$, is analyzed. Moreover, a tractable approximation of the above MSE is derived along with the combining strategy that minimizes it. This approximation, which is denoted by $\widetilde{\varepsilon}$ in the following, behaves as an upper bound and its accuracy increases with the number of transmit antennas.

Figure 35 illustrates the MSE as a function of the number of transmit/receive antennas. The considered massive MIMO system with 1-bit ADCs/DACs achieves very low values of the MSE when truly massive antenna arrays are deployed at both the transmitter and receiver. Notably, its MSE is less than twice that of an equivalent system with and 1-bit ADCs and full-resolution DACs, where the latter is achieved at the cost of significantly higher RF power consumption and complexity at the transmitter. Considering non-Gaussian data symbols, Figure 36 depicts the soft-estimated symbols with 16-PSK assuming different numbers of transmit/receive antennas. Increasing the number of antennas significantly reduces the spread of the soft-estimated symbols around the corresponding transmitted data symbols, resulting in a better SER performance. Considering that no coding is applied, a reasonable SER in the order of 10^{-2} is attained even with $N_{\text{Tx}} = N_{\text{Rx}} = 400$, whereas an impressive SER in the order of 10^{-4} is attained when $N_{\text{Tx}} = N_{\text{Rx}} = 1600$.

C. ML-BASED CONTEXT-AWARE RECEIVER FOR PN COMPENSATION

Transmitting at sub-THz frequencies poses major challenges due to the signal distortion caused by hardware impairments, e.g., PA nonlinearity [196] and oscillator PN [197]. These distortions disrupt the orthogonal reception of the DFT-s-OFDM signals, which is a candidate waveform for higher frequencies, leading to ICI in the received signals. The legacy strategies of PN mitigation in 5G systems involve estimating the PN from transmitted PTRS and compensating for the CPE, which is the average PN across a symbol. However, the residual ICI remains due to PN variations across symbols, degrading the receiver's performance. Fully compensating

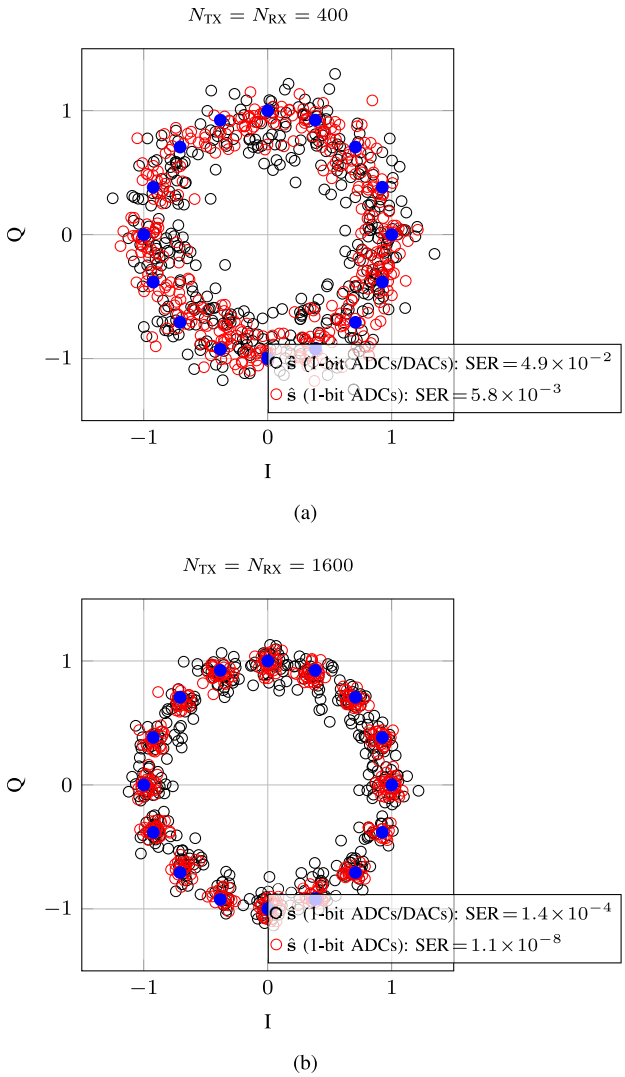

FIGURE 36. [Section V-B] Soft-estimated symbols for 1-bit ADCs/DACs and 1-bit ADCs, with 16-PSK, $K = 8$, $\rho = 10$ dB [194]: (a) $N_{Tx} = N_{Rx} = 400$; (b) $N_{Tx} = N_{Rx} = 1600$. The solid blue marks represent the transmitted data symbols.

for PN is often impractical or requires a high density of PTRS. In this regard, the residual ICI is still present even after the compensation, altering the noise distribution of the equalized signal at the receiver, which deviates from the uncorrelated AWGN typically assumed in the legacy receivers. This discrepancy degrades soft bit computation and reduces the efficiency of soft decoding algorithms, e.g., the ones for LDPC decoding. To this end, we present an ML-based context-aware receiver specifically tailored for DFT-s-OFDM transmissions, which enhances soft bit computation in the presence of PN [197]. This contribution addresses the challenge of *hardware impairments* described in Section II-C.

The architecture of the proposed ML-based context-aware receiver is presented in Figure 37. The ML-based context-aware receiver consists of an fully connected neural network (FCNN) that: (1) receives the real and imaginary parts of the equalized symbols together with the contextual information representation; and (2) computes soft inputs to the decoder by extracting the contextual information from the empirical distribution of the distortions using a convolutional neural network (CNN). The FCNN consists of a series of matrix-vector multiplications and additions with a nonlinear function applied between each multiplication. Each network layer undergoes a linear transformation followed by a bias addition (also called translation). In the hidden layers, this translation is followed by a nonlinear rectified linear unit activation function. The weights and biases are optimized through gradient-based learning using training data, which includes the equalized symbols derived from the equalizer for each DFT-s-OFDM symbol and their corresponding transmitted bits. The FCNN operates on a per-subcarrier basis, producing log-likelihood ratio values corresponding to different bits as outputs. Consequently, the FCNN has two input neurons and the number of output neurons corresponds to the number of bits given by $\log_2(M)$, where M represents the constellation size.

To enhance the per-subcarrier FCNN processing, the context-aware soft demapper incorporates a contextual representation module—specifically, a CNN—that provides information about the receiver's operating conditions. For instance, the per-subcarrier FCNN can be informed whether the current slot is significantly impaired by PN or follows an AWGN profile. In the context-aware receiver, the FCNN's input features are expanded by three additional dimensions derived from the CNN's output, which acts as a hyperparameter and connects to the FCNN. The CNN's input consists of a two-dimensional normalized histogram of equalized symbols received across all the subcarriers within a transmission slot. The histogram's size is chosen as a power of 2—specifically, a 32×32 image—to enable efficient implementation. The CNN operates only once per prediction interval (one slot), meaning that, although its forward pass is computationally more complex than the FCNN's, its overall contribution to complexity remains minimal. Both the CNN and FCNN are trained end-to-end with gradients backpropagated through both networks during each mini-batch processing step. This approach ensures an efficient contextual representation for each slot.

Figure 38 depicts the BLER obtained with the proposed ML-based context-aware receiver (with PN) and with the legacy receiver (with and without PN). The simulations consider a carrier frequency of 100 GHz, SCS of 960 kHz, bandwidth of 1.5 GHz. The transmitted signals are 64-QAM modulated, the "clustered delay line A" channel model is considered for evaluations, and the UE speed is assumed to be 3 km/h. The results confirm that the proposed ML-based context-aware receiver can partially compensate for the impact of the PN and reduce the BLER below 0.1, while the legacy receiver fails to reach this reliability level even at higher SNR. We conclude this section by noting that the methods presented here and in Section V-A2 are just two illustrative examples of the potential of ML-based

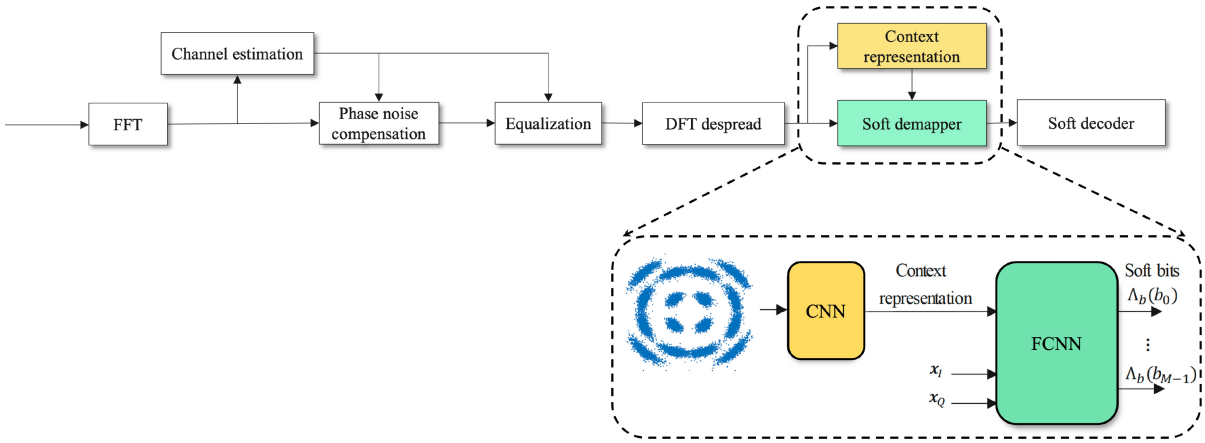

FIGURE 37. [Section V-C] ML-based context-aware receiver architecture for PN compensation.

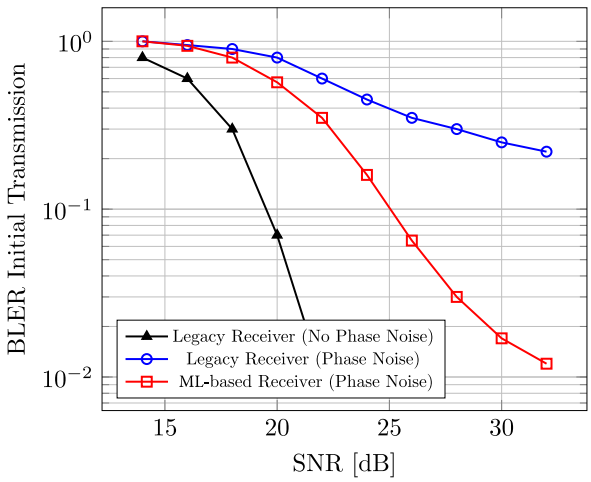

FIGURE 38. [Section V-C] BLER performance of the ML-based context-aware receiver and the legacy receiver in the presence of PN [197].

approaches to address specific sub-THz challenges. For a broader overview of this topic, we refer to [18], [32]; for a comprehensive perspective from the Hexa-X-II project on radio interfaces driven by artificial intelligence, we refer to [198].

D. ENERGY-EFFICIENT NETWORK DEPLOYMENT

In contrast to mmWave and sub-6 GHz systems, the transmit power of sub-THz systems may increase to guarantee coverage and high throughput. However, the achievable output power of PA devices is low and inefficient, and hence the overall energy efficiency of deployed systems becomes a major concern. Recently, multiple studies addressed this is issue by proposing new circuit design, waveform and modulation schemes, and transceiver architectures, as presented in Sections IV, V-A.1, and V-A.2. In this section, we analyze the impact of different hybrid beamforming configurations on the throughput and energy efficiency. This contribution addresses the challenge of *RF power consumption and complexity (energy-efficient network deployment)* described in Section II-B.2.

The potential to improve energy efficiency can be leveraged through the use case requirements, the appropriate hybrid beamforming architecture, and the number of BSs. For instance, increasing the number of BSs and reducing the inter-BS distance lower the required transmit power and thus the power consumption per BS, which is not entirely offset by the increased number of BSs. In addition, the flexible management of resources and MIMO systems allows to maximize the spectral efficiency for different conditions (i.e., varying number of UEs and data rate requirements). In this regard, we address the trade-off of spectral and energy efficiency of hybrid beamforming at the BSs. System-level simulations are used to evaluate coverage and throughput of an indoor network deployment varying the number of BSs and the number of UEs. The energy efficiency is assessed through a refined power consumption model based on [53].

Figure 39 depicts the 30 $\times$ 60 m indoor area used in the system-level simulations, as similarly used in [118]. This area can represent, e.g., a shopping mall, a conference room, or an office. The BSs are distributed evenly along the widest walls 4 m above the ground and the antennas point toward the inside of the area. We consider four deployment scenarios with 4 and 8 BSs serving simultaneously 8 or 16 randomly distributed UEs. The throughput is obtained by evaluating the signal-to-interference-plus-noise ratio and varying the transmit power P_{T} of the BS. At each BS, we assume a uniform planar array with ideal beams selected from a predefined grid of beams. For the channel model, we consider the modified 3GPP model adapted to 140 GHz obtained in [118]. Lastly, the carrier frequency is $f_{\mathrm{c}} = 144$ GHz and the bandwidth is $B \approx 5$ GHz.

Figure 40 depicts the simulated CDFs of the throughput, with 8 and 16 UEs, 4 and 8 BSs, and $P_{\mathrm{T}} \in \{17, 23, 29, 35\}$ dBm. With 8 UEs, Figure 40(a) shows that the deployment of 8 BSs and $P_{\mathrm{T}} = 17$ dBm per BS (dashed red line) provides similar coverage and throughput as the deployment of 4 BSs and $P_{\mathrm{T}} = 29$ dBm (solid blue

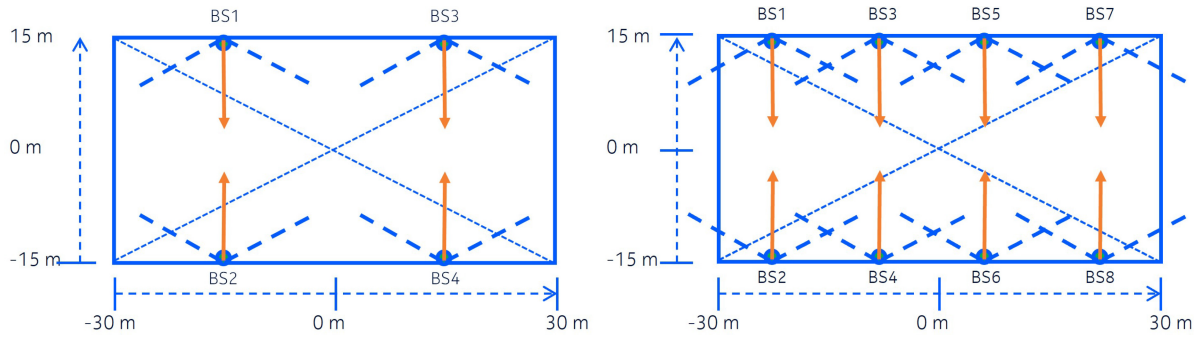

FIGURE 39. [Section V-D] Indoor scenario with 4 (left) and 8 (right) BSs used for assessment [81].

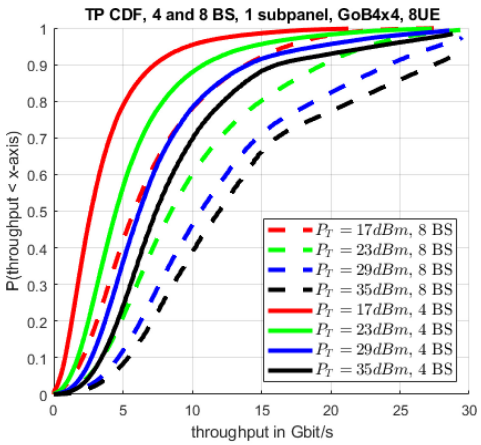

(a)

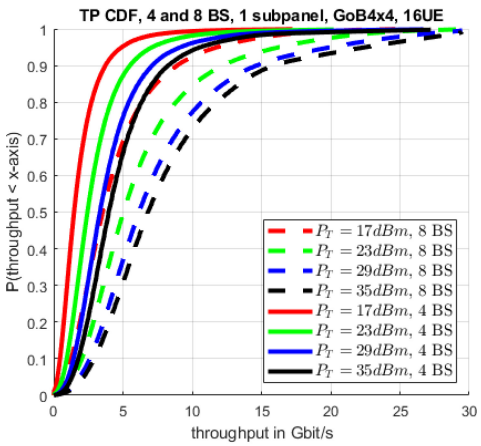

(b)

FIGURE 40. [Section V-D] Throughput CDFs within the simulation area varying the BS transmit power (P_T) [81]: (a) 8 UEs; (b) 16 UEs.

line). This behavior is more prominent in Figure 40(b) as the number of UEs increases to 16. In this scenario, the deployment of 4 BSs and $P_T = 35$ dBm (solid black line) has a comparable performance as the one with 8 BSs and $P_T = 17$ dBm. The difference in transmit power per BS between the deployments of 4 BSs and 8 BSs is 12 dB for 8 UEs and 18 dB for 16 UEs. Taking into account twice the number of BSs, there is still a benefit of 9 dB and 15 dB for the 8-BS deployment. Furthermore, a high-level power consumption analysis can be performed in terms of the PAs. If we assume an optimistic PA efficiency of 10%, the additional power consumption of 4 BSs is roughly 27 W higher than the power consumption of 8 BSs serving the 8-UE, obtained as

$$17 \text{ dBm} \Rightarrow 50 \text{ mW}, \ 8 \times 50 \text{ mW}/0.1 = 4 \text{ W},$$
$$29 \text{ dBm} \Rightarrow 794 \text{ mW}, \ 4 \times 794 \text{ mW}/0.1 = 31.7 \text{ W}.$$

For 16-UE, the difference increases approximately to 122 W, obtained as

$$17 \text{ dBm} \Rightarrow 50 \text{ mW}, \ 8 \times 50 \text{ mW}/0.1 = 4 \text{ W},$$
$$35 \text{ dBm} \Rightarrow 3.16 \text{ W}, \ 4 \times 3.16 \text{ W}/0.1 = 126 \text{ W}.$$

These high-level considerations show that a proper network deployment can substantially decrease the power consumption. For an accurate analysis, further factors need to be considered such as RF front ends, ADCs/DACs, up- and down-converters, and baseband processing. To assess this trade-off, a detailed power consumption model was proposed in [87], which for the analog parts relies on published power consumption data of existing sub-THz devices. The baseband processing power consumption is modeled with a detailed analysis of computational complexity and taking into account the intrinsic efficiency of latest application-specific integrated circuit technologies. Hence by applying this model, the total power consumption of the RF parts at the transmitter side in the 8-BS scenario is about 87% lower compared with the 4-BS scenario. Although the power consumption of the other system parts increases, the 8-BS scenario can still save about 45% of the power. The presented example focuses on optimizing fixed deployments for a given area. Future work will extend the insights from optimized static deployments to dynamic scenarios, enabling adaptations such as switching BSs on and off in response to changes in the number of UEs, UE distribution, and traffic demand. These additional opportunities for reducing the power consumption have not been explicitly considered and will require scheduler optimization to fully exploit the possible configuration options.

E. SECTION SUMMARY

We studied the evolution of 5G NR waveforms and numerology toward the sub-THz frequency band in Section V-A.1. With suitable SCS and waveform selection, the impact of PN and decreased PA efficiency can be mitigated, making efficient operation in the sub-THz band possible. We also explored the potential of new modulations for the sub-THz band. In this regard, we proposed PN-robust constellation designs under PAPR constraints and a practical sub-THz hardware setup in Section V-A.2. This framework offers flexibility in balancing decoding performance and PAPR based on the system's requirements. Future work should study beamforming and array PN effects in MIMO settings, along with other RF impairments such as IQ imbalance, mutual coupling, and quantization. Furthermore, ZXM discussed in Section V-A.3 exhibits significantly higher energy efficiency than QAM when considering the power consumption of the RF front end. However, this advantage comes at the cost of a reduced peak data rate, which makes ZXM suitable for scenarios where energy efficiency is prioritized over peak data rate. Lastly, we presented PCs in Section V-A.4 as an alternative to the QAM constellations classically used with OFDM. 16-PC is close to 16-QAM in terms of robustness to AWGN and admits twice the Doppler shift, whereas 16-Spiral offers very high robustness to the Doppler shift. Ultimately, both evolutionary and revolutionary waveforms and modulations presented in Section V-A can be utilized for sub-THz communications, with the choice depending on the specific performance targets and constraints. To this end, their performance should be assessed using the channel models described in Section III-B.

Massive MIMO will be a cornerstone of future wireless generations, and sub-THz communications will require simplifying MIMO architectures by reducing the resolution of the ADCs/DACs. In this context, 1-bit ADCs/DACs offer several advantages in terms of RF cost, power consumption, and complexity, as described in Section V-B. While this paper primarily centers on 1-bit data converters due to their unique advantages, slightly higher resolutions (e.g., 2–5 bits) also hold significant potential for sub-THz systems, offering a broader design space with trade-offs between performance, energy efficiency, and implementation feasibility. Future work should focus on the practical implementation of low-resolution and 1-bit massive MIMO systems, incorporating real-world RF hardware and channels for comprehensive testing and validation, and also address the out-of-band emissions caused by 1-bit DACs. Furthermore, ML-based methods have great potential to compensate for the impact of hardware impairments in sub-THz communications. The ML-based context-aware receiver presented in Section V-C opens opportunities to relax the requirements on the oscillator's PN at the expense of some extra baseband signal processing, and also showed performance gains for compensating the nonlinearity of the PA. This method can potentially compensate for the impact of other hardware impairments, such as oscillator PN, PA nonlinearity, and ADC/DAC quantization distortion provided that the ML model is trained with the appropriate data. The performance gains under such conditions should be verified in future work. Lastly, to achieve a specific throughput and coverage within a deployment scenario, arrangements with different numbers of BSs and hybrid beamforming schemes can be applied, as shown in Section V-D. In addition to using efficient individual components, energy-efficient network deployments also need to consider the way of dimensioning and installing the network elements. In future work, accurate models for power consumption and system's throughput evaluation should be used to properly characterize all the involved trade-offs.

VI. SUB-THZ JCAS

JCAS is emerging as a fundamental component of 6G wireless systems, integrating communication and sensing functionalities into a single cohesive system [199]. This integration enables devices and networks to transfer data while concurrently perceiving the surrounding environment (e.g., connected devices and passive objects). Such dual functionality is anticipated to significantly enhance the efficiency and capability of wireless systems and to enable novel applications (e.g., autonomous driving, smart cities) that require high data rates and high localization accuracy [23].

Within the JCAS framework, sensing can be categorized into localization and radar-like sensing [200]. Other definitions such as sensing the environment and the channel exist but are out of the scope of this section. Localization requires a connected device and a single or multiple anchors. Hence. trilateration, triangulation, or hybrid localization (i.e., using both range and angle measurements) can be performed by using the geometric parameters (e.g., range and angle) estimated from the signal. Radar-like sensing senses passive objects by extracting information from the reflected signal (e.g., by using a dual-functional radar-communication BS). Specifically, monostatic sensing involves co-located transmitters and receivers, while bistatic separates transmitter and receiver, enabling more flexible deployment and enhanced spatial coverage. Multistatic sensing involves multiple nodes acting as transmitters and/or receivers, which improves detection capabilities and robustness against obstacles [201]. Figure 41 illustrates the various localization and sensing techniques.

The integration of communication and sensing in JCAS is classified into two main levels: loose and tight integration. Loose integration involves sharing some of the hardware components between the communication and sensing operations but allows them to operate independently. This approach offers simplicity and ease of implementation. In contrast, tight integration involves a deeper fusion of communication and sensing, intertwining both functionalities at a fundamental level, including shared signal processing and joint optimization. This level of integration promises maximum efficiency and performance enhancement but requires a more complex system design [201].

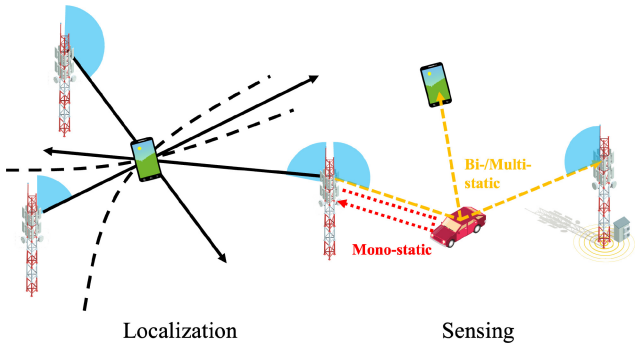

FIGURE 41. [Section VI] Illustration of localization and radar-like sensing.

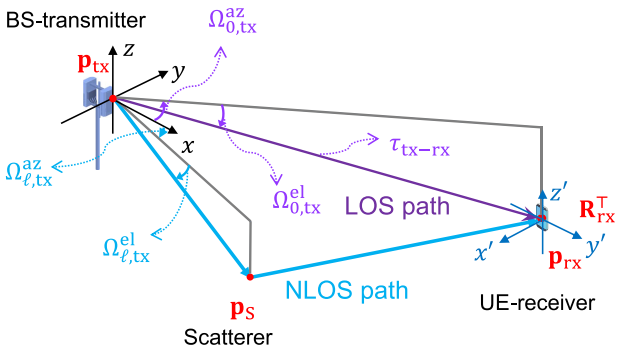

FIGURE 42. [Section VI-A.1] Illustration of the state parameters and geometry parameters. Based on the AoD and AoA (not visualized) estimations at the BS (downlink scenario) and the UE, together with the delay estimations of the LoS path and NLoS path, the positions of the UE and the scattering point can be estimated.

Sub-THz frequencies play a particularly significant role in JCAS. For sensing, sub-THz waves offer finer delay resolution due to their higher bandwidth. These are crucial for applications requiring high levels of accuracy, such as detailed industrial inspections or advanced medical imaging. For communications, sensing at sub-THz frequencies can optimize the communication path by identifying the optimal transmission route and avoiding obstacles, thus enhancing the reliability and performance of the system. Consequently, the dual-functional property of the JCAS system has garnered a lot of attention in sub-THz bands. In this regard, this section provides an overview of the fundamentals of sub-THz JCAS, then examines the power consumption aspects, and discusses contemporary challenges along with their potential solutions.

A. FUNDAMENTALS OF SUB-THZ JCAS

In this section, we describe the fundamentals of sub-THz JCAS, covering the geometric channel model, key features, and sensing key performance indicators (KPIs). It is worth noting that both communication and sensing services operate within the same physical environment and thus should share a common channel model. However, the stochastic channel models proposed by the communication community often fail to capture the geometric and temporal correlations that are essential for sensing. As a result, the sensing community has introduced its own geometric channel models. This divergence highlights the need for the JCAS community to develop a unified channel model that reconciles the needs of both communication and sensing domains.

1) JCAS GEOMETRIC CHANNEL MODEL

A typical JCAS system model considers a transmitter, a receiver, and $L-1$ scatterers located at p_{tx}, p_{rx}, and $p_{\text{S}} = [p_1, \ldots, p_{L-1}]$, respectively, as shown in Figure 42. For bistatic sensing and localization, we consider a channel model similar to (2) with an extra emphasis on the geometric nature of the channel parameters. Hence, we assume the channel $\boldsymbol{H}(t,f)$ constitutes the summation over the L channels including: the LoS channel, i.e., channel between p_{tx} and p_{rx}; and the $L-1$ NLoS channels, i.e., channels between p_{tx}, the $L-1$ scatterers p_{S}, and p_{rx}. In addition, we assume that all the NLoS paths are single-bounce reflections. Then, the geometric channel parameters are τ_ℓ, υ_ℓ, $\boldsymbol{\Omega}^{\text{tx}}_\ell = (\Omega^{\text{tx}}_{\ell,\text{az}}, \Omega^{\text{tx}}_{\ell,\text{el}})$, and $\boldsymbol{\Omega}^{\text{rx}}_\ell = (\Omega^{\text{rx}}_{\ell,\text{az}}, \Omega^{\text{rx}}_{\ell,\text{el}})$, which respectively correspond to the delay, Doppler, AoD, and AoA of the ℓ-th path, and the subscript notations "az" and "el" denote azimuth and elevation angles, respectively. Also, $\ell = 0$ denotes the LoS path. The channel delay, also known as time of arrival (ToA), is modeled as

$$\tau_\ell = \begin{cases} \frac{d_{\text{tx-rx}}}{c} + \delta, & \ell = 0 \\ \frac{d_{\text{tx-}\ell}}{c} + \frac{d_{\ell\text{-rx}}}{c} + \delta, & \ell \geq 1, \end{cases} \tag{19}$$

where $d_{\text{tx-rx}} = \|p_{\text{rx}} - p_{\text{tx}}\|$ is the distance between the transmitter and the receiver, $d_{\text{tx-}\ell} = \|p_\ell - p_{\text{tx}}\|$ is the distance between the transmitter and the ℓ-th scatterer, $d_{\ell\text{-rx}} = \|p_{\text{rx}} - p_\ell\|$ is the distance between the ℓ-th scatterer and the receiver, and δ is the clock offset between the transmitter and the receiver. Likewise, the Doppler frequency shifts are modeled as follows

$$\upsilon_\ell = \begin{cases} f\left(\frac{\boldsymbol{v}^{\top}_{\text{tx-rx}} p_{\text{tx-rx}}}{d_{\text{tx-rx}} c} + \delta_f\right), & \ell = 0 \\ f\left(\frac{\boldsymbol{v}^{\top}_{\text{tx-}\ell} p_{\text{tx-}\ell}}{d_{\text{tx-}\ell} c} + \frac{\boldsymbol{v}^{\top}_{\ell\text{-rx}} p_{\ell\text{-rx}}}{d_{\ell\text{-rx}} c} + \delta_f\right), & \ell \geq 1, \end{cases} \tag{20}$$

where $\boldsymbol{v}_{\text{tx-rx}} = \boldsymbol{v}_{\text{rx}} - \boldsymbol{v}_{\text{tx}}$, $\boldsymbol{v}_{\text{tx-}\ell} = \boldsymbol{v}_\ell - \boldsymbol{v}_{\text{tx}}$, $\boldsymbol{v}_{\ell\text{-rx}} = \boldsymbol{v}_{\text{rx}} - \boldsymbol{v}_\ell$, $p_{\text{tx-rx}} = p_{\text{rx}} - p_{\text{tx}}$, $p_{\text{tx-}\ell} = p_\ell - p_{\text{tx}}$, $p_{\ell\text{-rx}} = p_{\text{rx}} - p_\ell$, and δ_f is the carrier frequency offset (CFO) between the transmitter and the receiver. Here, $\boldsymbol{v}_{\text{tx}}$, $\boldsymbol{v}_{\text{rx}}$, and $\boldsymbol{v}_\ell$ are the velocities of the transmitter, receiver, and the ℓ-th scatterer, respectively. Lastly, the AoD and AoA pairs are defined as follows

$$\Omega^{g}_{\ell,\text{az}} = \arctan\left(\frac{[\boldsymbol{R}^{\top}_g p_{g\text{-}\ell}]_2}{[\boldsymbol{R}^{\top}_g p_{g\text{-}\ell}]_1}\right), \tag{21}$$

$$\Omega^{g}_{\ell,\text{el}} = \arcsin\left(\frac{[\boldsymbol{R}^{\top}_g p_{g\text{-}\ell}]_3}{d_{g\text{-}\ell}}\right), \tag{22}$$

where $g \in \{\text{tx}, \text{rx}\}$ and $\boldsymbol{R}^{\top}_g \in \text{SO}(3)$ is the 3D rotation matrix of the transmitter or receiver that rotates the vectors from the global coordinate system to their local coordinates. SO(3) is the special orthogonal group that comprises the set of all

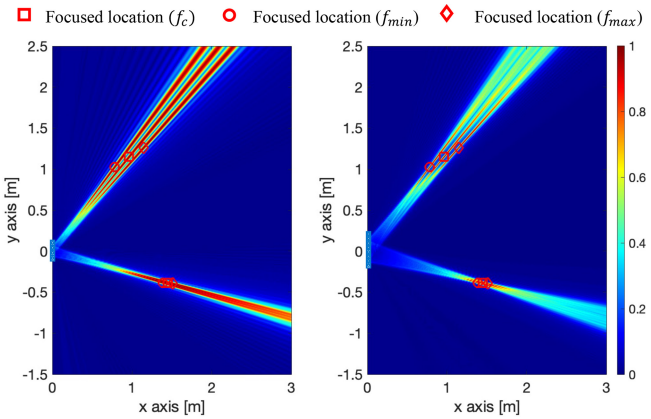

FIGURE 43. [Section VI-A2] Illustration of the near-field features for arrays with different numbers of antennas (128 antennas in the left figure and 256 antennas in the right figure), with $f_c = 140$ GHz, $f_{\min} = 135$ GHz, and $f_{\max} = 145$ GHz. With an increased number of antennas, the beam squint effect becomes beam misfocusing [203].

rotation matrices in a 3D space. A detailed geometric model can be found in [23], [202].

In this system model, the localization goal is to estimate the UE's state $s_g = [p_g^\top, \boldsymbol{v}_g^\top, \boldsymbol{R}_g^\top, \delta, \delta_f]^\top$, whether it is the transmitter or the receiver. The bistatic sensing also estimates the states of the passive objects $s_S = [p_S^\top, \boldsymbol{v}_S^\top]^\top$, based on the received signals at the receiver. Note that passive objects do not involve clock offsets or CFOs; however, other parameters such as radar cross-section, shape, or size of an extended target can be considered. Monostatic sensing follows a similar channel model with some modifications. For instance, the AoA and AoD are identical, as the transmitter and receiver are located in the same place. Additionally, no clock offset or CFO is present, as the transmitter and receiver share the same LO.

2) SUB-THZ JCAS FEATURES

Channel model: Due to the high attenuation of sub-THz signals, the channel becomes sparse and more geometric. Specifically, the channel model in (2) consists of fewer paths, and the angle tuple $\boldsymbol{\Omega}_\ell^g$, delay τ_l, and Doppler υ_l are more deterministic, as shown in the previous section, which is suitable for model-based channel parameter extraction and sensing algorithm design.

Near-field channels: To combat high signal propagation loss, large antenna arrays (in terms of wavelength) are adopted, resulting in near-field operating scenarios [204]. Despite a more complex channel model, curvature of arrival information based on a spherical model can be utilized for accurate localization and sensing [203].

Beam squint effect: Due to the frequency-independent phase shifters and the high bandwidth in the sub-THz band, the beams are focused in different directions/locations in the far-/near-field scenarios, which is called the beam squint effect, shown in Figure 43. While the beam squint effect degrades the array gain, it can contribute to the fast near-field beam training [205].

Hardware impairments: Hardware impairments are present in all communication systems, but they are more pronounced in sub-THz JCAS systems. There is a higher requirement and expectation for sensing accuracy in these systems compared with lower-frequency systems. As a result, biases and uncertainties caused by hardware-induced model mismatches need to be minimized. Additionally, sub-THz systems face significant impairments such as PN, JCAS inefficiencies, and array-related issues (e.g., mutual coupling and antenna gain error) [206]. While these impairments may have a limited impact on communication, they substantially degrade sensing performance.

THz imaging: Terahertz time-domain spectroscopy can extract spectral information to identify material types and shapes using amplitude-based, phase-based, or combined techniques, providing unique features for the high-frequency communication signals [207]. Due to the low scattering property, the signal waveforms traversed or reflected from objects can be exploited to produce high-contrast images. Several sub-THz imaging applications have been studied, such as automotive applications [208] and security body scanning [209].

Sub-THz molecular sensing: Beyond geometric sensing and positioning, sub-THz frequencies are also well-suited for molecular sensing due to their ability to interact with the unique rotational signatures of gas molecules. Unlike lower-frequency microwave signals, sub-THz waves can resolve dense molecular absorption patterns, enabling the identification and quantification of specific gases through their spectral fingerprints [210]. This capability has been applied in environmental monitoring, where pollutants such as nitriles exhibit strong, distinguishable absorption features [210]. The relatively long wavelengths (1–3 mm) in this band also experience low scattering from small particles, improving measurement reliability in practical settings. In biomedical contexts, sub-THz waves offer both high contrast and deep tissue penetration. For example, passive sensing in the 80–100 GHz range has been used to detect changes in skin water content, which may indicate specific medical conditions [211]. Higher-frequency setups (e.g., 220–330 GHz) have also demonstrated the ability to detect vapor-phase biomarkers at low concentrations [212]. These examples highlight the versatility of sub-THz sensing beyond positioning, especially in scenarios where non-contact, high-specificity detection is required.

3) SENSING KPIs

While there are no specific KPIs tailored exclusively for sub-THz JCAS, understanding and optimizing these sensing metrics are fundamental for advancing the capabilities and the reliability of future sub-THz JCAS systems. These metrics encompass accuracy, resolution, coverage, efficiency, stability, and scalability. Accuracy reflects the degree of precision in sensing measurements, ensuring that data collected from the environment aligns closely with ground truth values. Resolution denotes the system's ability to

differentiate between closely spaced objects, which is crucial for detailed spatial or temporal analysis. Coverage indicates the extent of the effective sensing area, influencing its overall utility in diverse environments. Efficiency encompass energy efficiency, resource efficiency, and deployment efficiency. Energy efficiency measures the energy consumption of the sensing components relative to their performance, being essential for prolonging the system's lifespan and reducing operational costs. Reusing resources such as time and bandwidth for both communication and sensing purposes can lead to high resource efficiency. Likewise, optimizing the deployment of BSs to serve both communication and sensing purposes leads to deployment efficiency. Due to the critical role of power efficiency in sub-THz JCAS, a dedicated discussion is provided in the next section. Stability assesses the system's ability to maintain consistent and reliable sensing performance over time, which is essential for long-term deployment in dynamic environments. Finally, scalability evaluates the system's capacity to adapt and expand its sensing capabilities to accommodate growing demands or changes in deployment scenarios [202], [213].

B. SUB-THZ JCAS POWER CONSUMPTION

With the shift toward sub-THz frequencies, energy efficiency becomes crucial for sustaining battery life in resource-limited devices while also reducing the environmental impact [214]. Hence, there is a need to develop power allocation solutions for JCAS that maximize sensing performance while maintaining a desired communication quality. Currently, there is no standard figure of merit that reflects the power consumption related to JCAS. For communication, the consumption factor (CF) is defined as the ratio between the maximum data rate and the total power consumption [214]. For sensing, we use a similar approach and define the CF as the ratio between a specific sensing parameter performance achieved over a period of time (application-dependent unit "A") and the power consumed during that period (expressed in W). For communication, the specific performance "A" can be the number of bits transferred. For sensing, positioning, and JCAS, "A" can include metrics such as range and angle accuracy, target detection probability, correct classification rate, radar mutual information, and Fisher information. To illustrate this concept, we conduct an analysis to examine the behavior of the CF when transitioning from mmWave operating at 28 GHz to sub-THz operating at 140 GHz carrier frequencies. To quantify this change, we evaluate the CF using "A", defined as the Fisher information, which measures the accuracy of time or range via ToA and angular accuracy through AoA. The results indicate that transitioning from mmWave to sub-THz leads to a higher CF for the same SNR, implying increased sensing or ToA and AoA accuracy. However, achieving high SNR levels requires significantly greater power consumption, while accuracy improvements become marginal. As shown in Figure 44, there is a threshold where the mmWave CF surpasses the sub-THz CF, highlighting an efficiency trade-off in the power consumption. Therefore, instead of pushing for extremely high SNR, finding a balance between power and performance of "A" is essential for energy-efficient JCAS.

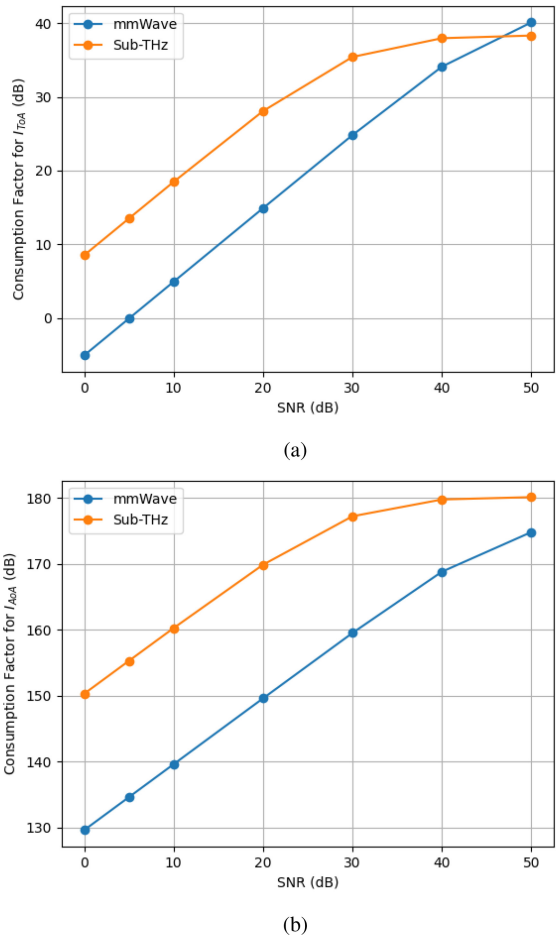

FIGURE 44. [Section VI-B] Increased consumption factor using Fisher information for (a) ToA and (b) AoA.

C. SUB-THZ JCAS CHALLENGES AND SOLUTIONS

Developing JCAS systems in the sub-THz range presents a series of formidable challenges as well as possible innovative solutions, as summarized in the following.

Hardware limitations: The performance of available components, i.e., amplifiers, antennas, and mixers, often falls short in terms of power output, sensitivity, and NF. Researchers are countering these limitations by exploring new materials such as graphene, which enhances the performance of electronic components. Additionally, SiGe technology [215] is being used to improve the efficiency of amplifiers and oscillators at these higher frequencies.

Waveforms and modulations: OFDM-based multi-carrier waveform has been widely adopted in communication systems. However, OFDM is very complex to implement in the sub-THz band, and it results in the PAPR problem [207]. In addition to the SC modulation and on-off keying modes provided in the sub-THz standard [216], other waveform

designs (e.g., DFT-s-OFDM and discrete Fourier transform-spread-orthogonal time frequency space) are also effective in sub-THz systems [217], bringing new opportunities for localization and sensing tasks.

Signal attenuation: Sub-THz waves experience significant atmospheric absorption and rain fading, which drastically reduces their effective range. To mitigate this phenomenon, highly directional antennas can be utilized to focus energy more efficiently. However, dedicated access point deployment is required to ensure the JCAS performance within the service area. More advanced array shapes rather than planner arrays can also be considered to improve coverage [218].

Beam optimization: A large antenna array with high beamforming gain is another way to mitigate signal attenuation. However, extremely precise beam steering and alignment are necessary to maintain stable connections, as small alignment errors can result in substantial communication disruptions. This problem is further exacerbated when operating under high-mobility scenarios. Advanced beamforming techniques (e.g., adaptive width beamforming or ML-based beam design) can be employed to address this issue [31]. Additionally, location and map information can speed up the beam training process by optimizing the codebook with a limited area. Likewise, having knowledge about the velocity of the UE, through sensing, can mitigate beam misalignment due to high mobility.

System deployment: Layout (i.e., BS placement) optimization in sub-THz systems is critical due to the sensitivity of high-frequency signals to path loss and atmospheric absorption. These blockages (e.g., obstacles and human bodies) can reduce the effectiveness of the LoS path, affecting both communication coverage and sensing accuracy. Strategic placement and alignment of antennas optimize LoS paths and incorporate advanced materials for improved performance. Additionally, new enablers such as RIS can be deployed at low cost, enhancing both communication and sensing capabilities in sub-THz systems.

Sensing algorithms: Due to the new features introduced in the sub-THz system and the coexistence of communication and sensing signals, sophisticated signal processing techniques and advanced coding strategies can be employed to distinguish between different types of signals and effectively extract sensing information, thus, optimizing the use of the frequency spectrum. Additionally, feature extractions and classification algorithms are also needed for sensing purposes [24].

Security and privacy: The high sensing resolution, positioning accuracy, and imaging granularity of sub-THz systems have raised important security and privacy concerns. For instance, sub-THz systems can be exploited to monitor human activity or track individuals without consent, posing risks of unauthorized surveillance and data misuse [219]. As emphasized in [220], the ability of next-generation wireless systems to infer location and behavioral patterns with sub-meter accuracy can be abused to violate user privacy. These concerns call for early attention to regulatory frameworks and the development of privacy-preserving mechanisms tailored for high-resolution sensing technologies.

Regulations and standards: The use of sub-THz frequencies is crucial yet complex, affecting the uniform deployment of technology. To navigate these regulatory challenges, international collaboration among regulatory bodies and stakeholders is needed (e.g., the IEEE 802.15 standardization project [221]). This collaboration aims to develop universal standards and protocols that ensure compatibility and interoperability across different technologies and regions, facilitating the compliant and efficient deployment of sub-THz systems.

D. SECTION SUMMARY

The future direction of sub-THz JCAS systems is characterized by enhancements in channel models, estimation algorithms, and optimization strategies crucial for 6G wireless systems. Advanced channel models will increasingly account for complex sub-THz propagation characteristics like severe path loss and atmospheric absorption, improving the accuracy and reliability of system's designs. In parallel, estimation algorithms are evolving, focusing on robust 3D position and orientation estimation techniques that are essential for high-precision applications such as autonomous driving and industrial IoT. Additionally, optimization efforts are concentrating on refining offline designs and online adjustments to resource allocation and beamforming, particularly through the use of RIS. These advancements aim to achieve higher data rates, enhanced localization accuracy, and efficient and energy-aware operations in the challenging sub-THz spectrum for next-generation wireless systems.

VII. CONCLUSION

In this section, we outline key topics not covered in this work and provide some concluding remarks.

A. RELATED TOPICS BEYOND THE SCOPE OF THIS WORK

Here, we briefly highlight additional topics relevant to sub-THz communications but beyond the scope of this work: channel estimation, satellite communications, physical-layer security, and medium access control (MAC) protocols.

Channel estimation: Channel estimation in the sub-THz band is particularly challenging due to the reduced coherence time at higher frequencies [173, Rem. 2.1], which requires frequent pilot transmissions. To mitigate the resulting overhead, several works have leveraged the inherent sparsity of sub-THz channels while accounting for wideband effects. For instance, [222] proposed a three-stage wideband sparse channel estimation scheme comprising coarse angle estimation, angle refinement, and delay/gain extraction. Furthermore, [223] introduced a wideband sparse channel estimation method tailored for SC systems, effectively addressing beam squint, multipath

fading, and molecular absorption. Different ML-based techniques have also been proposed in this context [24]. To mitigate the increasing hardware impairments at sub-THz frequencies, [224] proposed a nonlinear channel estimation framework that models the distortion effects using Gaussian process regression while simultaneously exploiting the inherent sparsity of the channels. In addition, the near-field effects commonly encountered at sub-THz frequencies introduce new challenges, as angle estimation alone is no longer sufficient, as well as opportunities, as the distance information can be leveraged for more accurate channel estimation and localization [225], [226]. These considerations are essential for developing efficient and scalable channel estimation methods in future sub-THz systems.

Other MIMO enablers: MIMO technologies beyond traditional massive MIMO can further enhance spectral efficiency, coverage, and robustness in sub-THz communications by dynamically shaping the propagation environment. In this context, RISs act as programmable metasurfaces that manipulate EM waves to improve signal quality, extend coverage, and overcome blockages without the need for active power amplification [17]. However, the practical implementation of RIS-aided sub-THz communications requires addressing several critical hardware and signal processing challenges [227]. On the other hand, fluid antenna systems consist of software-controllable antenna structures that can alter their shape and position to reconfigure the gain, radiation pattern, operating frequency, and other characteristics [228]. Fluid antennas represent a promising solution for enhancing sub-THz communications due to their ability to adapt in real time to changing channel conditions, offering additional spatial diversity and interference mitigation capabilities without significantly increasing hardware complexity [229]. The ability of fluid antennas to operate over different frequencies is particularly valuable, as it enables the reuse of the same hardware across a wider range of frequency bands. Lastly, the emerging concept of holographic MIMO, which integrates a very large number of small antennas or reflective elements into a compact space to realize a spatially continuous aperture, is especially well-suited for the sub-THz band due to the significantly reduced antenna size [230]. The control and optimization of these MIMO enablers (especially RISs) introduce additional challenges (e.g., in terms of channel estimation and signaling), which constitute active research areas on their own.

Satellite communications: Sub-THz links hold significant potential for satellite communications thanks to their highly directional beams, which enable focused transmission between satellites and ground stations. This precision enhances data rates and security by minimizing interference. However, these benefits come with downsides: the extremely narrow beams require precise beam alignment and tracking, increasing the system's complexity and susceptibility to misalignment caused by satellite motion or atmospheric disturbances. For ground-to-satellite sub-THz links, very large aperture antennas are necessary to compensate for the severe free-space path loss over long distances and atmospheric attenuation, in addition to molecular absorption losses and noise [231]. Such links are particularly viable with low Earth orbit satellites, whose range is typically limited to a few hundred km. In satellite-to-satellite links, the dense deployment of modern satellite constellations calls for careful management of cross-link interference, both within the same constellation and across different ones [232], [233]. Furthermore, airplane-to-satellite sub-THz links may represent a valuable alternative to conventional airplane-to-ground connections because the atmospheric losses are considerably lower in these aerial paths [234], [235].

Physical-layer security: Physical-layer security in sub-THz communications capitalizes on the highly directional beams and strong path loss inherent to high-frequency transmissions, which naturally reduce the likelihood of unintended signal interception and thereby enhance confidentiality [236]. Nevertheless, LoS transmissions remain susceptible to interception. Possible physical-layer attacks in THz scenarios and their countermeasures were reviewed in [237], with focus on massive IoT applications. To further mitigate eavesdropping threats, recent studies have highlighted the benefits of advanced beamforming techniques and the use of RISs, which can dynamically shape the radiation pattern to further limit signal leakage toward unintended directions [238], [239]. Additionally, near-field propagation (commonly encountered at sub-THz frequencies) offers enhanced protection against information leakage in the same angular direction as the intended transmission [240]. Its effectiveness can be further improved by injecting artificial noise, particularly when the eavesdropper is located closer to the BS than the legitimate UE [241].

MAC protocols: Sub-THz communications introduce unique challenges at the MAC layer, requiring a rethinking of conventional protocol designs. First of all, the use of highly directional beams may lead to the so-called deafness phenomenon, where nodes not currently aligned through the correct beams may be unaware of ongoing transmissions. This renders traditional contention-based schemes such as carrier sense multiple access ineffective, calling for novel MAC protocols tailored for highly directional beams [242]. Additionally, sub-THz links are vulnerable to dynamic blockages, necessitating rapid link recovery and robust beam tracking mechanisms. These challenges are exacerbated by ultra-high data rates and stringent latency constraints, which require efficient scheduling and retransmission strategies [6]. To address these issues, recent works have proposed intelligent and adaptive MAC designs. For instance, [243] introduced an ML-based MAC framework to improve UE association, resource allocation, and mobility management while maximizing the system's reliability. This and other MAC approaches, such as those surveyed in [32], highlight a trend toward context-aware, ML-driven MAC protocols specific for the highly directional, fast-varying nature of sub-THz wireless systems.

B. SUMMARY AND FUTURE WORK

Although the FR3 band has gained renewed attention for the initial 6G rollout, the sub-THz spectrum remains highly significant for the long-term evolution of 6G and future wireless generations. In this paper, we presented the holistic perspective on sub-THz communications developed within the European 6G flagship project Hexa-X-II, along with the technical contributions and key findings that have shaped this perspective. We tackled the fundamental PHY challenges of sub-THz communications, i.e., understanding and modeling of radio propagation, RF power consumption and complexity, and hardware impairments. To achieve this, we presented several results across three core areas, i.e., signal propagation and channel modeling, RF transceiver design, and PHY enablers, offering useful insights into the development of sub-THz systems. Lastly, we provided an overview of sub-THz JCAS, emphasizing it as one of the most promising applications in the sub-THz range.

Our results suggest that sub-THz channel measurements and modeling should be customized to align with the specific characteristics of each use case and deployment scenario. Additionally, heterogeneous integration of multiple integrated circuit technologies in sub-THz RF transceiver design offers a promising techno-economical trade-off for addressing RF power consumption and hardware impairments. In terms of PHY enablers, both evolutionary and revolutionary waveforms and modulations can be effective at sub-THz frequencies, whereas low-complexity massive MIMO and energy-efficient network deployments are crucial for reducing RF power consumption, complexity, and cost. Moreover, ML-based methods show great potential in compensating for sub-THz hardware impairments. Lastly, exploiting sub-THz frequencies in JCAS enables both high-precision sensing and high-quality communications, which can further benefit from leveraging near-field and beam squint effects.

Future work should focus on the joint optimization of the proposed waveforms, modulations, and massive MIMO configurations under the developed sub-THz channel, RF power consumption, and hardware impairment models. This comprehensive approach will allow to derive optimized setups tailored to specific communication/sensing use cases and deployment scenarios, each defined by distinct performance targets and constraints. Furthermore, experimental validation through testbeds should be pursued to assess the practical feasibility of the proposed models and techniques. Such validation will help bridge the gap between theoretical analysis and real-world implementation, paving the way for robust and scalable sub-THz systems in future wireless generations.

ACRONYMS

3D	3-dimensional
3GPP	Third-Generation Partnership Project
5G	fifth-generation
6G	sixth-generation
ADC	analog-to-digital converter
AoA	angle of arrival
AoD	angle of departure
APSK	amplitude and phase-shift keying
ASA	azimuth spread of arrival angle
AWG	arbitrary waveform generator
AWGN	additive white Gaussian noise
BCE	binary cross entropy
BER	bit error rate
BLER	block error rate
BS	base station
CDF	cumulative distribution function
CF	consumption factor
CFO	carrier frequency offset
CMOS	complementary metal-oxide-semiconductor
CNN	convolutional neural network
COTS	commercial off-the-shelf
CP	cyclic prefix
CP-OFDM	cyclic prefix-orthogonal frequency-division multiplexing
CPE	common phase error
DAC	digital-to-analog converter
DFT-s-OFDM	discrete Fourier transform-spread-orthogonal frequency-division multiplexing
DSP	digital signal processing
EIRP	effective isotropic radiated power
EM	electromagnetic
EMF	electromagnetic field
EVM	error vector magnitude
FCNN	fully connected neural network
FTN	faster-than-Nyquist
FTR	fluctuating two-ray
GaAs	gallium arsenide
GaN	gallium nitride
i.i.d.	independent and identically distributed
ICI	inter-carrier interference
ICNIRP	International Commission on Non-Ionizing Radiation Protection
IF	intermediate frequency
InP	indium phosphide
IoT	Internet of Things
IQ	in-phase and quadrature
ISI	inter-symbol interference
ITU	International Telecommunication Union
ITU-R	ITU Radiocommunication Sector
JCAS	joint communications and sensing
KED	knife edge diffraction
KPI	key performance indicator
LDPC	low-density parity check
LNA	low-noise amplifier
LO	local oscillator
LoS	line-of-sight
MAC	medium access control
MIMO	multiple-input multiple-output
ML	machine learning

mmWave	millimeter-wave
MPC	multipath component
MRT	maximum ratio transmission
MSE	mean squared error
MUT	material under test
NF	noise figure
NLoS	non-line-of-sight
NR	New Radio
OFDM	orthogonal frequency-division multiplexing
OTFS	orthogonal time frequency space
PA	power amplifier
PADP	power-angular delay profile
PAPR	peak-to-average power ratio
PC	polar constellation
PDP	power delay profile
PHY	physical-layer
PLL	phase-locked loop
PN	phase noise
PPS	pulse per second
PSK	phase-shift keying
PTRS	phase tracking reference signals
QAM	quadrature amplitude modulation
RF	radio-frequency
RIS	reconfigurable intelligent surface
RLL	runlength-limited
RoF	radio-over-fiber
S-V	Saleh-Valenzuela
SAR	specific absorption rate
SC	single-carrier
SC-FDE	single carrier with frequency-domain equalization
SCS	subcarrier spacing
SER	symbol error rate
SiGe	silicon-germanium
SNR	signal-to-noise ratio
ToA	time of arrival
UAV	unmanned aerial vehicle
UE	user equipment
VNA	vector network analyzer
ZXM	zero-crossing modulation

ACKNOWLEDGMENT

The authors thank the anonymous reviewers for their constructive comments, which helped improve the quality and completeness of this work.

REFERENCES

[1] *NR; User Equipment (UE) Radio Transmission and Reception; Part 1: Range 1 Standalone*, 3GPP Standard 38.101-1, 2024.
[2] *NR; User Equipment (UE) Radio Transmission and Reception; Part 2: Range 2 Standalone*, 3GPP Standard 38.101-2, 2024.
[3] *Study on the 7 to 24 GHz Frequency Range for NR*, 3GPP Standard 38.820, 2021.
[4] N. Rajatheva et al. "White paper on broadband connectivity in 6G." 2020. [Online]. Available: https://oulurepo.oulu.fi/handle/10024/36799
[5] C.-X. Wang et al., "On the road to 6G: Visions, requirements, key technologies, and testbeds," *IEEE Commun. Surveys Tuts.*, vol. 25, no. 2, pp. 905–974, 2nd Quart., 2023.
[6] N. H. Mahmood, I. Atzeni, E. A. Jorswieck, and O. L. A. López, "Ultra-reliable low-latency communications: Foundations, enablers, system design, and evolution towards 6G," *Found. Trends Commun. Inf. Theory*, vol. 20, nos. 5–6, pp. 512–747, 2023.
[7] H. Pennanen, T. Hänninen, O. Tervo, A. Tölli, and M. Latva-Aho, "6G: The intelligent network of everything," *IEEE Access*, vol. 13, pp. 1319–1421, 2025.
[8] *World Radiocommunication Conference 2023 (WRC-23) Final Acts*, ITU, Geneva, Switzerland, 2024.
[9] K. Rikkinen, P. Kyösti, M. E. Leinonen, M. Berg, and A. Parssinen, "THz radio communication: Link budget analysis toward 6G," *IEEE Wireless Commun. Mag.*, vol. 58, no. 11, pp. 22–27, Nov. 2020.
[10] V. Petrov, T. Kurner, and I. Hosako, "IEEE 802.15.3d: First standardization efforts for sub-terahertz band communications toward 6G," *IEEE Commun. Mag.*, vol. 58, no. 11, pp. 28–33, Nov. 2020.
[11] A. Faisal, H. Sarieddeen, H. Dahrouj, T. Y. Al-Naffouri, and M.-S. Alouini, "Ultramassive MIMO systems at terahertz bands: Prospects and challenges," *IEEE Veh. Technol. Mag.*, vol. 15, no. 4, pp. 33–42, Dec. 2020.
[12] C. Castro, R. Elschner, T. Merkle, C. Schubert, and R. Freund, "Experimental demonstrations of high-capacity THz-wireless transmission systems for beyond 5G," *IEEE Commun. Mag.*, vol. 58, no. 11, pp. 41–47, Nov. 2020.
[13] C.-X. Wang, J. Wang, S. Hu, Z. H. Jiang, J. Tao, and F. Yan, "Key technologies in 6G terahertz wireless communication systems: A survey," *IEEE Veh. Technol. Mag.*, vol. 16, no. 4, pp. 27–37, Dec. 2021.
[14] S. Liu, X. Yu, R. Guo, Y. Tang, and Z. Zhao, "THz channel modeling: Consolidating the road to THz communications," *China Commun.*, vol. 18, no. 5, pp. 33–49, 2021.
[15] Z. Chen et al., "Terahertz wireless communications for 2030 and beyond: A cutting-edge frontier," *IEEE Commun. Mag.*, vol. 59, no. 11, pp. 66–72, Nov. 2021.
[16] J. F. Buckwalter et al., "Fundamental limits of high-efficiency silicon and compound semiconductor power amplifiers in 100-300 GHz bands," *ITU J. Future Evol. Technol.*, vol. 2, no. 7, pp. 39–50, 2021.
[17] H. Sarieddeen, M.-S. Alouini, and T. Y. Al-Naffouri, "An overview of signal processing techniques for terahertz communications," *Proc. IEEE*, vol. 109, no. 10, pp. 1628–1665, Oct. 2021.
[18] A.-A. A. Boulogeorgos et al., "Machine learning: A catalyst for THz wireless networks," *Front. Commun. Netw.*, vol. 2, Sep. 2021, Art. no. 704546.
[19] X.-X. Yin, A. Baghai-Wadji, and Y. Zhang, "A biomedical perspective in terahertz nano-communications—A review," *IEEE Sensors J.*, vol. 22, no. 10, pp. 9215–9227, Mar. 2022.
[20] H.-J. Song and N. Lee, "Terahertz communications: Challenges in the next decade," *IEEE Trans. THz. Sci. Technol.*, vol. 12, no. 2, pp. 105–117, Mar. 2022.
[21] D. Serghiou, M. Khalily, T. W. C. Brown, and R. Tafazolli, "Terahertz channel propagation phenomena, measurement techniques and modeling for 6G wireless communication applications: A survey, open challenges and future research directions," *IEEE Commun. Surveys Tuts.*, vol. 24, no. 4, pp. 1957–1996, 4th Quart., 2022.
[22] C. Han et al., "Terahertz wireless channels: A holistic survey on measurement, modeling, and analysis," *IEEE Commun. Surveys Tuts.*, vol. 24, no. 3, pp. 1670–1707, 3rd Quart., 2022.
[23] H. Chen, H. Sarieddeen, T. Ballal, H. Wymeersch, M.-S. Alouini, and T. Y. Al-Naffouri, "A tutorial on terahertz-band localization for 6G communication systems," *IEEE Commun. Surveys Tuts.*, vol. 24, no. 3, pp. 1780–1815, 3rd Quart., 2022.
[24] S. Helal, H. Sarieddeen, H. Dahrouj, T. Y. Al-Naffouri, and M.-S. Alouini, "Signal processing and machine learning techniques for terahertz sensing: An overview," *IEEE Signal Process. Mag.*, vol. 39, no. 5, pp. 42–62, Sep. 2022.
[25] C. Chaccour, M. N. Soorki, W. Saad, M. Bennis, P. Popovski, and M. Debbah, "Seven defining features of terahertz (THz) wireless systems: A fellowship of communication and sensing," *IEEE Commun. Surveys Tuts.*, vol. 24, no. 2, pp. 967–993, 2nd Quart., 2022.
[26] M. M. Azari, S. Solanki, S. Chatzinotas, and M. Bennis, "THz-empowered UAVs in 6G: Opportunities, challenges, and trade-offs," *IEEE Wireless Commun. Mag.*, vol. 60, no. 5, pp. 24–30, May 2022.

[27] I. F. Akyildiz, C. Han, Z. Hu, S. Nie, and J. M. Jornet, "Terahertz band communication: An old problem revisited and research directions for the next decade," *IEEE Trans. Commun.*, vol. 70, no. 6, pp. 4250–4285, Jun. 2022.

[28] O. A. Amodu, C. Jarray, S. A. Busari, and M. Othman, "THz-enabled UAV communications: Motivations, results, applications, challenges, and future considerations," *Ad Hoc Netw.*, vol. 140, Mar. 2023, Art. no. 103073.

[29] J. C. Balzer et al., "THz systems exploiting photonics and communications technologies," *IEEE J. Microw.*, vol. 3, no. 1, pp. 268–288, Jan. 2023.

[30] Y. Huang, Y. Shen, and J. Wang, "From terahertz imaging to terahertz wireless communications," *Engineering*, vol. 22, pp. 106–124, Mar. 2023.

[31] M. Q. Khan, A. Gaber, P. Schulz, and G. Fettweis, "Machine learning for millimeter wave and terahertz beam management: A survey and open challenges," *IEEE Access*, vol. 11, pp. 11880–11902, 2023.

[32] M. Jaber and J.-Y. Pyun, "Terahertz meets AI: The state of the art," *Sensors*, vol. 23, no. 11, p. 5034, 2023.

[33] K. Rasilainen, T. D. Phan, M. Berg, A. Pärssinen, and P. J. Soh, "Hardware aspects of sub-THz antennas and reconfigurable intelligent surfaces for 6G communications," *IEEE J. Sel. Areas Commun.*, vol. 41, no. 8, pp. 2530–2546, Aug. 2023.

[34] N. U. Saqib, M. S. Haroon, H. Y. Lee, K. Park, H.-G. Song, and S.-W. Jeon, "THz communications: A key enabler for future cellular networks," *IEEE Access*, vol. 11, pp. 117474–117493, 2023.

[35] A. Shafie, N. Yang, C. Han, J. M. Jornet, M. Juntti, and T. Kürner, "Terahertz communications for 6G and beyond wireless networks: Challenges, key advancements, and opportunities," *IEEE Netw.*, vol. 37, no. 3, pp. 162–169, May/Jun. 2023.

[36] W. K. Alsaedi, H. Ahmadi, Z. Khan, and D. Grace, "Spectrum options and allocations for 6G: A regulatory and standardization review," *IEEE Open J. Commun. Soc.*, vol. 4, pp. 1787–1812, 2023.

[37] F. Sheikh et al., "THz measurements, antennas, and simulations: From the past to the future," *IEEE J. Microw.*, vol. 3, no. 1, pp. 289–304, Jan. 2023.

[38] W. Jiang et al., "Terahertz communications and sensing for 6G and beyond: A comprehensive review," *IEEE Commun. Surveys Tuts.*, vol. 26, no. 4, pp. 2326–2381, 4th Quart., 2024.

[39] J. M. Jornet et al., "The evolution of applications, hardware design, and channel modeling for terahertz (THz) band communications and sensing: Ready for 6G?" *Proc. IEEE*, early access, Jul. 1, 2024, doi: 10.1109/JPROC.2024.3412828.

[40] A. O. Amodu et al., "Technical advancements toward RIS-assisted NTN-based THz communication for 6G and beyond," *IEEE Access*, vol. 12, pp. 183153–183181, 2024.

[41] S. Thomas, J. S. Virdi, A. Babakhani, and I. P. Roberts, "A survey on advancements in THz technology for 6G: Systems, circuits, antennas, and experiments," *IEEE Open J. Commun. Soc.*, vol. 6, pp. 1998–2016, 2025.

[42] International Commission on Non-Ionizing Radiation Protection, "Guidelines for limiting exposure to electromagnetic fields (100 kHz to 300 GHz)," *Health Phys.*, vol. 118, no. 5, pp. 483–524, 2020.

[43] P. Kyästi et al., *WINNER II Channel Models*. Hoboken, NJ, USA: Wiley, 2008.

[44] T. S. Rappaport, G. R. MacCartney, M. K. Samimi, and S. Sun, "Wideband millimeter-wave propagation measurements and channel models for future wireless communication system design," *IEEE Trans. Commun.*, vol. 63, no. 9, pp. 3029–3056, Sep. 2015.

[45] "Study on channel model for frequencies from 0.5 to 100 GHz," 3GPP, Sophia Antipolis, France, Rep. 38.901, 2024.

[46] "Effects of building materials and structures on radiowave propagation above about 100 MHz," ITU, Geneva, Switzerland, ITU-Recommendation P.2040-3, 2023.

[47] Y. Li, C. Tao, G. Seco-Granados, A. Mezghani, A. L. Swindlehurst, and L. Liu, "Channel estimation and performance analysis of one-bit massive MIMO systems," *IEEE Trans. Signal Process.*, vol. 65, no. 15, pp. 4075–4089, Aug. 2017.

[48] S. Jacobsson, G. Durisi, M. Coldrey, U. Gustavsson, and C. Studer, "Throughput analysis of massive MIMO uplink with low-resolution ADCs," *IEEE Trans. Wireless Commun.*, vol. 16, no. 6, pp. 1304–1309, Jun. 2017.

[49] B. Murmann. "ADC performance survey 1997–2024." 2024. [Online]. Available: https://github.com/bmurmann/ADC-survey

[50] K. Roth, H. Pirzadeh, A. L. Swindlehurst, and J. Nossek, "A comparison of hybrid beamforming and digital beamforming with low-resolution ADCs for multiple users and imperfect CSI," *IEEE J. Sel. Topics Signal Process.*, vol. 12, no. 3, pp. 484–498, Jun. 2018.

[51] I. Atzeni, A. Tölli, and G. Durisi, "Low-resolution massive MIMO under hardware power consumption constraints," in *Proc. Asilomar Conf. Signals Syst. Comput. (ASILOMAR)*, 2021, pp. 1–8.

[52] Hexa-X. "Deliverable D2.3: Radio models and enabling techniques towards ultra-high data rate links and capacity in 6G." 2023. [Online]. Available: https://hexa-x.eu/wp-content/uploads/2023/04/Hexa-X-D2_3_v1.0.pdf

[53] H. Halbauer and T. Wild, "Towards power efficient 6G sub-THz transmission," in *Proc. Eur. Conf. Netw. Commun. (EuCNC) 6G Summit*, 2021, pp. 25–30.

[54] H. Wang et al., *Power Amplifiers Performance Survey 2000-Present*, Georgia Tech Electron. Micro-Syst. Lab., Atlanta, GA, USA, 2022.

[55] A. Prata, S. C. Pires, M. Acar, A. S. R. Oliveira, and N. B. Carvalho, "Towards circulator-free multi antenna transmitters for 5G," in *Proc. IEEE MTT-S Int. Microw. Symp. (IMS)*, 2017, pp. 1–8.

[56] P. Rodríguez-Vázquez, M. E. Leinonen, J. Grzyb, N. Tervo, A. Parssinen, and U. R. Pfeiffer, "Signal-processing challenges in leveraging 100 gb/s wireless THz," in *Proc. 2nd 6G Wireless Summit (6G SUMMIT)*, 2020, pp. 1–5.

[57] F. Sheikh, R. Nagisetty, T. Karnik, and D. Kehlet, "2.5-D and 3-D heterogeneous integration: Emerging applications," *IEEE Solid-State Circuits Mag.*, vol. 13, no. 4, pp. 77–87, Feb. 2021.

[58] M. Sarajlić et al., "Waveforms for sub-THz 6G: Design guidelines," in *Proc. Eur. Conf. Netw. Commun. (EuCNC) 6G Summit*, 2023, pp. 1–7.

[59] S. Ju, Y. Xing, O. Kanhere, and T. S. Rappaport, "Millimeter wave and sub-terahertz spatial statistical channel model for an indoor office building," *IEEE J. Sel. Areas Commun.*, vol. 39, no. 6, pp. 1561–1575, Jun. 2021.

[60] N. A. Abbasi et al., "Double-directional channel measurements for urban THz microcellular communications in a street canyon," in *Proc. IEEE Int. Conf. Commun. (ICC)*, 2022, pp. 1–8.

[61] T. Doeker, C. Herold, J. M. Eckhardt, and T. Kürner, "Eavesdropping measurements for applications in office environments at low THz frequencies," *IEEE Trans. Microw. Theory Techn.*, vol. 71, no. 6, pp. 2748–2757, Jun. 2023.

[62] Y. Chen, Y. Li, C. Han, Z. Yu, and G. Wang, "Channel measurement and ray-tracing-statistical hybrid modeling for low-terahertz indoor communications," *IEEE Trans. Wireless Commun.*, vol. 20, no. 12, pp. 8163–8176, Dec. 2021.

[63] S. L. H. Nguyen, J. Järveläinen, A. Karttunen, K. Haneda, and J. Putkonen, "Comparing radio propagation channels between 28 and 140 GHz bands in a shopping mall," in *Proc. Eur. Conf. Antennas Propag. (EuCAP)*, 2018, pp. 1–5.

[64] M. F. D. Guzman, M. Hassan, and K. Haneda, "Uncertainty of millimeter-wave channel sounder due to integration of frequency converters," in *Proc. IEEE Int. Symp. Wireless Commun. Syst. (ISWCS)*, 2021, pp. 6504–6519.

[65] P. Zhang et al., "A modular COTS-based high-efficient sub-THz channel sounder and experimental validations," in *Proc. Eur. Conf. Antennas Propag. (EuCAP)*, 2024, pp. 1–8.

[66] N. A. Abbasi et al., "THz band channel measurements and statistical modeling for urban D2D environments," *IEEE Trans. Wireless Commun.*, vol. 22, no. 3, pp. 1466–1479, Mar. 2023.

[67] Y. Lyu, A. W. Mbugua, Z. Yuan, K. Olesen, and W. Fan, "Design and validation of a multilink phase-compensated long-range ultrawideband VNA-based channel sounder," *IEEE Trans. Microw. Theory Techn.*, vol. 70, no. 10, pp. 4528–4543, Oct. 2022.

[68] S. Rey, J. M. Eckhardt, B. Peng, K. Guan, and T. Kurner, "Channel sounding techniques for applications in THz communications: A first correlation based channel sounder for ultra-wideband dynamic channel measurements at 300 GHz," in *Proc. Int. Congr. Ultra Mod. Telecommun. Control Syst. Workshops (ICUMT)*, 2017, pp. 1–8.

[69] J. Lee, J.-J. Park, K.-W. Kim, M.-D. Kim, and H. K. Kwon, "159-GHz propagation measurement and analysis in urban microcellular environment for 6G," *IEEE Wireless Commun. Lett.*, vol. 12, no. 2, pp. 277–281, Feb. 2023.

[70] A. Al-jzari, J. Hu, and S. Salous, "Millimeter-wave and sub-THz channel measurements and characterization analysis in a street canyon scenario," in *Proc. Eur. Conf. Antennas Propag. (EuCAP)*, 2024, pp. 1–9.

[71] J.-M. Conrat, M. Aliouane, J.-C. Cousin, and X. Begaud, "Material permittivity and conductivity estimation from 2 to 260 GHz and extension of the ITU-R P.2040 model at frequency above 100 GHz," in *Proc. IEEE Int. Symp. Pers. Indoor Mobile Radio Commun. (PIMRC)*, 2024, p. 12.

[72] J.-M. Conrat, M. Aliouane, J.-C. Cousin, and X. Begaud, "Building material permittivity and conductivity estimation from 2 to 260 GHz," in *Proc. Eur. Microw. Conf. (EuMC)*, 2024, pp. 1–8.

[73] J. Pascual-García et al., "On the importance of diffuse scattering model parameterization in indoor wireless channels at mm-Wave frequencies," *IEEE Access*, vol. 4, pp. 688–701, 2016.

[74] P. Xie, K. Guan, D. He, H. Yi, J. Dou, and Z. Zhong, "Terahertz wave propagation characteristics on rough surfaces based on full-wave simulations," *Radio Sci.*, vol. 57, no. 6, pp. 1–16, 2022.

[75] S. Bakirtzis, T. Hashimoto, and C. D. Sarris, "FDTD-based diffuse scattering and transmission models for ray tracing of millimeter-wave communication systems," *IEEE Trans. Antennas Propag.*, vol. 69, no. 6, pp. 3389–3398, Jun. 2021.

[76] C. Jansen et al., "Diffuse scattering from rough surfaces in THz communication channels," *IEEE Trans. Thz. Sci. Technol.*, vol. 1, no. 2, pp. 462–472, Nov. 2011.

[77] J. Kokkoniemi, V. Petrov, D. Moltchanov, J. Lehtomaeki, Y. Koucheryavy, and M. Juntti, "Wideband terahertz band reflection and diffuse scattering measurements for beyond 5G indoor wireless networks," in *Proc. Eur. Wireless Conf. (EW)*, 2016, pp. 1–8.

[78] J. Ma, R. Shrestha, W. Zhang, L. Moeller, and D. M. Mittleman, "Terahertz wireless links using diffuse scattering from rough surfaces," *IEEE Trans. Thz. Sci. Technol.*, vol. 9, no. 5, pp. 463–470, Sep. 2019.

[79] M. Alissa, B. Friederich, F. Sheikh, A. Czylwik, and T. Kaiser, "Experimental investigation of terahertz scattering: A study of non-gaussianity and lateral roughness influence," *IEEE Access*, vol. 8, pp. 170672–170680, 2020.

[80] J.-M. Conrat, J.-C. Cousin, and X. Begaud, "Impact of rough building material surfaces on reflection coefficients from 5 GHz to 260 GHz," in *Proc. Eur. Conf. Antennas Propag. (EuCAP)*, 2025, pp. 1–8.

[81] Hexa-X-II. "Deliverable D4.3: Early results of 6G radio key enablers." 2024. [Online]. Available: https://hexa-x-ii.eu/wp-content/uploads/2024/04/Hexa-X-II_D4_3_v1.0_final.pdf

[82] P. Zhang et al., "Measurement-based characterization of D-band human body shadowing," in *Proc. Eur. Conf. Antennas Propag. (EuCAP)*, 2023, pp. 1–9.

[83] P. Kyösti, N. Tervo, M. Berg, M. E. Leinonen, K. Nevala, and A. Pärssinen, "Measured blockage effect of a finger and similar small objects at 300 GHz," in *Proc. Eur. Conf. Antennas Propag. (EuCAP)*, 2021, pp. 1–7.

[84] C. B. Findik, P. Zhang, V. Hovinen, M. E. Leinonen, A. Pärssinen, and P. Kyösti, "Dual-polarized diffraction measurements and modeling at D-Band frequencies," in *Proc. Eur. Conf. Antennas Propag. (EuCAP)*, 2024, pp. 1–9.

[85] M. F. de Guzman, K. Haneda, and P. Kyösti. "Measurement-based MIMO channel model at 140 GHz." 2023. [Online]. Available: https://doi.org/10.5281/zenodo.7640353

[86] M. F. D. Guzman and K. Haneda, "Analysis of wave-interacting objects in indoor and outdoor environments at 142 GHz," *IEEE Trans. Antennas Propag.*, vol. 71, no. 12, pp. 9838–9848, Dec. 2023.

[87] Hexa-X-II. "Deliverable D4.5: Final results of 6G radio key enablers." 2025. [Online]. Available: https://hexa-x-ii.eu/wp-content/uploads/2025/03/Hexa-X-II_D4_5_v1_edit.pdf

[88] S. Das, P. Zhang, and P. Kyösti. "Wideband near-field extension for the 3GPP geometry based stochastic channel model." 2025. [Online]. Available: https://doi.org/10.5281/zenodo.14843297

[89] P. Zhang et al., "Understanding sub-terahertz radio channels: Impact of beamforming on wireless system design," *IEEE Veh. Technol. Mag.*, early access.

[90] S. Priebe, M. Kannicht, M. Jacob, and T. Kurner, "Ultra broadband indoor channel measurements and calibrated ray tracing propagation modeling at THz frequencies," *J. Commun. Netw.*, vol. 15, no. 6, pp. 547–558, 2013.

[91] "Guidelines for evaluation of radio interface technologies for IMT-2020," ITU, Geneva, Switzerland, Rep. M.2412-0, 2017.

[92] METIS, "Deliverable D1.4: METIS channel models," European Union, Brussels, Belgium, document ICT-317669-METIS/D1.4, 2015.

[93] J. C. Lagarias, J. A. Reeds, M. H. Wright, and P. E. Wright, "Convergence properties of the Nelder–Mead simplex method in low dimensions," *SIAM J. Optim.*, vol. 9, no. 1, pp. 112–147, 1998.

[94] M. F. de Guzman and K. Haneda, "3GPP-like channel model at sub-terahertz: Improved cluster generation and experimental verification," *IEEE Trans. Antennas Propag.*, early access, May 1, 2025, doi: 10.1109/TAP.2025.3564506.

[95] J. Ye, S. Dang, G. Ma, O. Amin, B. Shihada, and M.-S. Alouini, "On outage performance of terahertz wireless communication systems," *IEEE Trans. Commun.*, vol. 70, no. 1, pp. 649–663, May 2022.

[96] J. Fu, P. Juyal, and A. Zajić, "Generalized modeling and propagation characterization of THz wireless links in computer desktop environment," *Radio Sci.*, vol. 57, no. 4, pp. 1–26, 2022.

[97] H. Du et al., "Performance and optimization of reconfigurable intelligent surface aided THz communications," *IEEE Trans. Commun.*, vol. 70, no. 5, pp. 3575–3593, 2022.

[98] E. N. Papasotiriou, A.-A. A. Boulogeorgos, K. Haneda, M. F. de Guzman, and A. Alexiou, "An experimentally validated fading model for THz wireless systems," *Sci. Rep.*, vol. 11, no. 1, 2021, Art. no. 18717.

[99] P. Bhardwaj, E. S. Karnawat, and S. M. Zafaruddin, "An exact statistical representation of α-η-κ-μ fading model for THz wireless communication," in *Proc. IEEE Global Commun. Conf. (GLOBECOM)*, 2023, pp. 1–8.

[100] E. N. Papasotiriou, A.-A. A. Boulogeorgos, and A. Alexiou, "Outdoor THz fading modeling by means of Gaussian and gamma mixture distributions," *Sci. Rep.*, vol. 13, no. 1, p. 6385, 2023.

[101] T. R. R. Marins et al., "Fading evaluation in the mm-Wave band," *IEEE Trans. Commun.*, vol. 67, no. 12, pp. 8725–8738, Dec. 2019.

[102] M. D. Yacoub, "The κ–μ; distribution and the η–μ distribution," *IEEE Antennas Propag. Mag.*, vol. 49, no. 1, pp. 68–81, Feb. 2007.

[103] M. Milisic, M. Hamza, and M. Hadzialic, "Outage performance of L-branch maximal-ratio combiner for generalized κ–μ fading," in *Proc. IEEE Veh. Technol. Conf. (VTC)*, 2008, p. 6.

[104] K. P. Peppas, "Sum of nonidentical squared κ–μ variates and applications in the performance analysis of diversity receivers," *IEEE Trans. Veh. Technol.*, vol. 61, no. 1, pp. 413–419, Jan. 2012.

[105] O. Özdogan, E. Björnson, and E. G. Larsson, "Massive MIMO with spatially correlated Rician fading channels," *IEEE Trans. Commun.*, vol. 67, no. 5, pp. 3234–3250, May 2019.

[106] M. R. Bhatnagar, "On the sum of correlated squared κ–μ shadowed random variables and its application to performance analysis of MRC," *IEEE Trans. Veh. Technol.*, vol. 64, no. 6, pp. 2678–2684, Jun. 2015.

[107] M. T. Tania, M. Ibrahim, M. S. Hossen, A. S. M. Badrudduza, and M. K. Kundu, "Combined impacts of co-channel interference and correlation on secrecy performance over κ–μ shadowed fading channel," in *Proc. Int. Conf. Adv. Elect. Electron. Eng. (ICAEEE)*, 2022, pp. 1–6.

[108] F. D. A. García, F. R. A. Parente, M. D. Yacoub, and J. C. S. S. Filho, "Exact κ-μ sum statistics," *IEEE Wireless Commun. Lett.*, vol. 12, no. 7, pp. 1284–1288, Jun. 2023.

[109] G. R. D. L. Tejerina and I. Atzeni. "Sum of squared extended η-μ and κ-μ RVs: A new framework applied to FR3 and sub-THz systems." 2025. [Online]. Available: https://arxiv.org/pdf/2502.02092

[110] "The mathematical functions site." 2001. Accessed: Oct. 19, 2023. [Online]. Available: http://functions.wolfram.com/

[111] "Attenuation by atmospheric gases and related effects," ITU, Geneva, Switzerland, Rep. P.676-13, 2022.

[112] A. F. Molisch et al., "Properties of sub-THz propagation channels and their impact on system behavior: Channel measurements and transmission experiments," *IEEE Wireless Commun.*, vol. 31, no. 1, pp. 18–24, Feb. 2024.

[113] P. Rodriguez-Vazquez, J. Grzyb, B. Heinemann, and U. R. Pfeiffer, "A QPSK 110-Gb/s polarization-diversity MIMO wireless link with a 220â 255 GHz tunable LO in a SiGe HBT technology," *IEEE Trans. Microw. Theory Techn.*, vol. 68, no. 9, pp. 3834–3851, Sep. 2020.

[114] P. Sen, J. Siles, N. Thawdar, and J. M. Jornet, "Multi-kilometre and multi-gigabit-per-second sub-terahertz communications for wireless backhaul applications," *Nat. Electron.*, vol. 6, pp. 164–175, Feb. 2023.

[115] I. Abdo et al., "A bi-directional 300-GHz-band phased-array transceiver in 65-nm CMOS with outphasing transmitting mode and LO emission cancelation," *IEEE J. Solid-State Circuits*, vol. 57, no. 8, pp. 2292–2308, Aug. 2022.

[116] M. Tolstrup, *Indoor Radio Planning: A Practical Guide for 2G, 3G and 4G*. Hoboken, NJ, USA: Wiley, 2015.

[117] T. Tuovinen, N. Tervo, and A. Pärssinen, "Analyzing 5G RF system performance and relation to link budget for directive MIMO," *IEEE Trans. Antennas Propag.*, vol. 65, no. 12, pp. 6636–6645, Dec. 2017.

[118] Hexa-X. "Deliverable D2.2: Initial radio models and analysis towards ultra-high data rate links in 6G." 2021. [Online]. Available: https://hexa-x.eu/wp-content/uploads/2022/01/Hexa-X-D2_2.pdf

[119] P. Skrimponis et al., "Power consumption analysis for mobile mmwave and sub-THz receivers," in *Proc. 6G Wireless Summit (6G Summit)*, 2020, pp. 1–5.

[120] C. Desset, P. Wambacq, Y. Zhang, M. Ingels, and A. Bourdoux, "A flexible power model for mm-Wave and THz high-throughput communication systems," in *Proc. IEEE Int. Symp. Pers. Indoor Mobile Radio Commun. (PIMRC)*, 2020, pp. 1–6.

[121] C. Desset, N. Collaert, S. Sinha, and G. Gramegna, "InP/CMOS co-integration for energy efficient sub-THz communication systems," in *Proc. IEEE Global Commun. Conf. (GLOBECOM)*, 2021, p. 45.

[122] International Commission on Non-Ionizing Radiation Protection, "Guidelines for limiting exposure to time-varying electric, magnetic, and electromagnetic fields (up to 300 GHz)," *Health Phys.*, vol. 74, no. 4, pp. 494–522, 1998.

[123] *Council Recommendation of 12 July 1999 on the Limitation of Exposure of the General Public to Electromagnetic Fields (0 Hz to 300 GHz)*, Council Eur. Union, Brussels, Belgium, 1999.

[124] *On the Minimum Health and Safety Requirements Regarding the Exposure of Workers to the Risks Arising From Physical Agents (Electromagnetic Fields) (20th Individual Directive Within the Meaning of Article vol. 16, no. 1 of Directive 89/391/EEC) and Repealing Directive 2004/40/EC*, Eur. Agency, Paris, France, 2013.

[125] *Assessment of the Compliance of Low-Power Electronic and Electrical Equipment With the Basic Restrictions Related to Human Exposure to Electromagnetic Fields (10 MHz to 300 GHz)*, IEC Standard 62479, 2010.

[126] *Determination of RF Field Strength, Power Density and SAR in the Vicinity of Base Stations for the Purpose of Evaluating Human Exposure*, IEC Standard 62232, 2022.

[127] *Assessment of Power Density of Human Exposure to Radio Frequency Fields From Wireless Devices in Close Proximity to the Head and Body (Frequency Range of 6 GHz to 300 GHz)—Part 1: Measurement Procedure for Incident Power Density*, IEC/IEEE Standard 63195-1, 2022.

[128] *Assessment of Power Density of Human Exposure to Radio Frequency Fields From Wireless Devices in Close Proximity to the Head and Body (Frequency Range of 6 GHz to 300 GHz)—Part 2: Computational Procedure for Incident Power Density*, IEC/IEEE Standard 63195-2, 2022.

[129] *Assessment of Power Density of Human Exposure to Radio Frequency Fields From Wireless Devices in Close Proximity to the Head and Body (Frequency Range of 6 GHz to 300 GHz)—Part 3: Measurement Procedure for Absorbed Power Density*, IEC/IEEE Standard 63195-3, 2026.

[130] *Assessment of Power Density of Human Exposure to Radio Frequency Fields From Wireless Devices in Close Proximity to the Head and Body (Frequency Range of 6 GHz to 300 GHz)—Part 4: Computational Procedure for Absorbed Power Density*, IEC/IEEE Standard 63 195-4, 2026.

[131] B. Xu, D. A. Sanjurjo, D. Colombi, and C. Törnevik, "A Monte Carlo analysis of actual maximum exposure from a 5G millimeter-wave base station antenna for EMF compliance assessments," *Front. Public Health*, vol. 9, Jan. 2022, Art. no. 777759.

[132] B. Xu et al., "A summary of actual maximum approach studies on EMF compliance of 5G radio base stations," in *Proc. Eur. Conf. Antennas Propag. (EuCAP)*, 2022, pp. 483–524.

[133] B. Xu, K. Zhao, Z. Ying, D. Sjöberg, W. He, and S. He, "Analysis of impacts of expected RF EMF exposure restrictions on peak EIRP of 5G user equipment at 28 GHz and 39 GHz bands," *IEEE Access*, vol. 7, pp. 20996–21005, 2019.

[134] W. He, B. Xu, Y. Yao, D. Colombi, Z. Ying, and S. He, "Implications of incident power density limits on power and EIRP levels of 5G millimeter-wave user equipment," *IEEE Access*, vol. 8, pp. 148214–148225, 2020.

[135] "NR; physical channels and modulation," 3GPP, Sophia Antipolis, France, Rep. 38.211, 2024.

[136] Y. Xing and T. S. Rappaport, "Terahertz wireless communications: Cosharing for terrestrial and satellite systems above 100 GHz," *IEEE Commun. Lett.*, vol. 25, no. 10, pp. 3156–3160, Oct. 2021.

[137] O. Tervo, T. Levanen, K. Pajukoski, J. Hulkkonen, P. Wainio, and M. Valkama, "5G new radio evolution towards sub-THz communications," in *Proc. 6G Wireless Summit (6G Summit)*, 2020, pp. 1–8.

[138] E. Dahlman, S. Parkvall, and J. Skold, *5G NR: The Next Generation Wireless Access Technology*. New York, NY, USA: Academic, 2018.

[139] "Study on new radio (NR) access technology; RF and co-existence aspects," 3GPP, Sophia Antipolis, France, Rep. 38.803, 2022.

[140] S. Tarboush, H. Sarieddeen, M.-S. Alouini, and T. Y. Al-Naffouri, "Single- versus multicarrier terahertz-band communications: A comparative study," *IEEE Open J. Commun. Soc.*, vol. 3, pp. 1466–1486, 2022.

[141] L. H. Nguyen, V. Braun, H. Halbauer, and T. Wild, "Waveform comparison under hardware limitations for 6G sub-THz communications," in *Proc. IEEE Annu. Consum. Commun. Netw. Conf. (CCNC)*, 2022, pp. 1–6.

[142] R. Hadani and A. Monk. "OTFS: A new generation of modulation addressing the challenges of 5G." 2018. [Online]. Available: https://arxiv.org/abs/1802.02623

[143] Z. Wei et al., "Orthogonal time–frequency space modulation: A promising next-generation waveform," *IEEE Wireless Commun.*, vol. 28, no. 4, pp. 136–144, Aug. 2021.

[144] Y. Bello, S. Barnola, D. Demmer, and J.-B. Dore, "OTFS waveform with phase noise in sub-THz," in *Proc. IEEE Veh. Technol. Conf. (VTC)*, 2022, pp. 28–33.

[145] D. Marasinghe, L. H. Nguyen, J. Mohammadi, Y. Chen, T. Wild, and N. Rajatheva, "Constellation shaping under phase noise impairment for sub-THz communications," in *Proc. IEEE Int. Conf. Commun. (ICC)*, 2024, pp. 1–7.

[146] D. Marasinghe, L. H. Nguyen, J. Mohammadi, Y. Chen, T. Wild, and N. Rajatheva "Waveform learning under phase noise impairment for sub-THz communications," *IEEE Trans. Wireless Commun.*, vol. 73, no. 1, pp. 117–131, Jan. 2025.

[147] F. A. Aoudia and J. Hoydis, "End-to-end learning for OFDM: From neural receivers to pilotless communication," *IEEE Trans. Wireless Commun.*, vol. 21, no. 2, pp. 1049–1063, Jun. 2022.

[148] F. A. Aoudia and J. Hoydis, "Waveform learning for next-generation wireless communication systems," *IEEE Trans. Commun.*, vol. 70, no. 6, pp. 3804–3817, Jun. 2022.

[149] L. H. Nguyen, H. Heimpel, D. Marasinghe, H. Halbauer, and T. Wild, "Sub-THz waveform evaluation in the D-band: A proof of concept study," in *Proc. Eur. Conf. Netw. Commun. (EuCNC) 6G Summit*, 2024, pp. 18–20.

[150] S. Ziabakhsh, G. Gagnon, and G. W. Roberts, "The peak-SNR performances of voltage-mode versus time-mode circuits," *IEEE Trans. Circuits Syst. II, Exp. Briefs*, vol. 65, no. 12, pp. 1869–1873, Dec. 2018.

[151] G. Fettweis, M. Dörpinghaus, S. Bender, L. Landau, P. Neuhaus, and M. Schlüter, "Zero crossing modulation for communication with temporally oversampled 1-bit quantization," in *Proc. Asilomar Conf. Signals Syst. Comput. (ASILOMAR)*, 2019, pp. 207–214.

[152] L. T. Landau, M. Dörpinghaus, and G. P. Fettweis, "1-bit quantization and oversampling at the receiver: Sequence-based communication," *EURASIP J. Wireless Commun. Netw.*, vol. 2018, pp. 1–24, Apr. 2018.

[153] P. Neuhaus, M. Dörpinghaus, and G. Fettweis, "Zero-crossing modulation for wideband systems employing 1-bit quantization and temporal oversampling: Transceiver design and performance evaluation," *IEEE Open J. Commun. Soc.*, vol. 2, pp. 1915–1934, 2021.

[154] M. Schlüter, M. Dörpinghaus, and G. P. Fettweis, "Joint phase and timing estimation with 1-bit quantization and oversampling," *IEEE Trans. Commun.*, vol. 70, no. 1, pp. 71–86, Jan. 2022.

[155] F. Gast, S. Zeitz, M. Dörpinghaus, and G. P. Fettweis, "Comparing iterative and least-squares based phase noise tracking in receivers with 1-bit quantization and oversampling," in *Proc. IEEE Stat. Signal Process. Workshop (SSP)*, 2023, pp. 1–6.

[156] F. Gast, M. Dörpinghaus, P. Sen, A. Nimr, and G. P. Fettweis, "Hardware-aware energy efficiency optimization in wireless communications using a Gearbox-PHY," *IEEE Commun. Lett.*, vol. 28, no. 7, pp. 1584–1588, Jul. 2024.

[157] F. Gast, F. Roth, M. Dörpinghaus, P. Sen, S. Zeitz, and G. Fettweis, "Energy optimization using joint modulation scheme and front end adaptation—The Gearbox-PHY," in *Proc. IEEE Int. Symp. Wireless Commun. Syst. (ISWCS)*, 2024, pp. 103–108.

[158] S. Cui, A. J. Goldsmith, and A. Bahai, "Energy-constrained modulation optimization," *IEEE Trans. Wireless Commun.*, vol. 4, no. 5, pp. 2349–2360, Sep. 2005.

[159] S. Yang, "A high-linearity down-conversion mixer with modified transconductance stage about 120 GHz," *J. Infrared Mil. Thz. Waves*, vol. 43, nos. 3–4, pp. 272–281, 2022.

[160] S. Yang, "Two implementations of 120 GHz transformer cross-coupled oscillator based on cascode structure in 55 nm CMOS technology," *Microw. Opt. Technol. Lett.*, vol. 64, no. 12, pp. 2172–2178, 2022.

[161] F. Roth, M. Dörpinghaus, S. Zeitz, F. Gast, and G. P. Fettweis, "Why to use the phase in time-encoding modulation and its effect on the spectral efficiency," in *Proc. IEEE Int. Symp. Pers. Indoor Mobile Radio Commun. (PIMRC)*, 2024, pp. 1–8.

[162] D. Arnold, H.-A. Loeliger, P. Vontobel, A. Kavcic, and W. Zeng, "Simulation-based computation of information rates for channels with memory," *IEEE Trans. Inf. Theory*, vol. 52, no. 8, pp. 3498–3508, Aug. 2006.

[163] L. Belostotski and S. Jagtap, "Down with noise: An introduction to a low-noise amplifier survey," *IEEE Solid-State Circuits Mag.*, vol. 12, no. 2, pp. 23–29, Sep. 2020.

[164] A. Mezghani and J. A. Nossek, "Modeling and minimization of transceiver power consumption in wireless networks," in *Proc. Int. ITG Workshop Smart Antennas (WSA)*, 2011, pp. 1–8.

[165] T. H. Lee and A. Hajimiri, "Oscillator phase noise: A tutorial," *IEEE J. Solid-State Circuits*, vol. 35, no. 3, pp. 326–336, Mar. 2000.

[166] J. Stott. "The effects of phase noise in COFDM." 1998. [Online]. Available: https://tech.ebu.ch/docs/techreview/trev_276-stott.pdf

[167] W. R. D. Petrovic and G. Fettweis, "Common phase error due to phase noise in OFDM-estimation and suppression," in *Proc. IEEE Int. Symp. Pers. Indoor Mobile Radio Commun. (PIMRC)*, 2004, pp. 1–8.

[168] A. L. Swindlehurst, E. Ayanoglu, P. Heydari, and F. Capolino, "Millimeter-wave massive MIMO: The next wireless revolution?" *IEEE Commun. Mag.*, vol. 52, no. 9, pp. 56–62, Sep. 2014.

[169] R. W. Heath, N. González-Prelcic, S. Rangan, W. Roh, and A. M. Sayeed, "An overview of signal processing techniques for millimeter wave MIMO systems," *IEEE J. Sel. Topics Signal Process.*, vol. 10, no. 3, pp. 436–453, Apr. 2016.

[170] A. K. Saxena, I. Fijalkow, and A. L. Swindlehurst, "Analysis of one-bit quantized precoding for the multiuser massive MIMO downlink," *IEEE Trans. Signal Process.*, vol. 65, no. 17, pp. 4624–4634, Sep. 2017.

[171] T. L. Marzetta, "Noncooperative cellular wireless with unlimited numbers of base station antennas," *IEEE Trans. Wireless Commun.*, vol. 9, no. 11, pp. 3590–3600, Nov. 2010.

[172] L. Lu, G. Y. Li, A. L. Swindlehurst, A. Ashikhmin, and R. Zhang, "An overview of massive MIMO: Benefits and challenges," *IEEE J. Sel. Areas Commun.*, vol. 8, no. 5, pp. 742–758, Oct. 2014.

[173] E. Björnson, J. Hoydis, and L. Sanguinetti, "Massive MIMO networks: Spectral, energy, and hardware efficiency," *Found. Trends Signal Process.*, vol. 11, no. 3–4, pp. 154–655, 2017.

[174] S. Jacobsson, G. Durisi, M. Coldrey, T. Goldstein, and C. Studer, "Quantized precoding for massive MU-MIMO," *IEEE Trans. Commun.*, vol. 65, no. 11, pp. 4670–4684, Nov. 2017.

[175] C. Studer and G. Durisi, "Quantized massive MU-MIMO-OFDM uplink," *IEEE Trans. Commun.*, vol. 64, no. 6, pp. 2387–2399, Jun. 2016.

[176] C. Mollán, J. Choi, E. G. Larsson, and R. W. Heath, "Uplink performance of wideband massive MIMO with one-bit ADCs," *IEEE Trans. Wireless Commun.*, vol. 16, no. 1, pp. 87–100, Jan. 2017.

[177] S. Jacobsson, G. Durisi, M. Coldrey, and C. Studer, "Linear precoding with low-resolution DACs for massive MU-MIMO-OFDM downlink," *IEEE Trans. Wireless Commun.*, vol. 18, no. 3, pp. 1595–1609, Mar. 2019.

[178] J. Mo and R. W. Heath, "Capacity analysis of one-bit quantized MIMO systems with transmitter channel state information," *IEEE Trans. Signal Process.*, vol. 63, no. 20, pp. 5498–5512, Oct. 2015.

[179] M. Ma, N. T. Nguyen, I. Atzeni, and M. Juntti, "Analysis of oversampling in uplink massive MIMO-OFDM with low-resolution ADCs," in *Proc. IEEE Int. Workshop Signal Process. Adv. Wireless Commun. (SPAWC)*, 2023, pp. 1–8.

[180] J. Choi, J. Mo, and R. W. Heath, "Near maximum-likelihood detector and channel estimator for uplink multiuser massive MIMO systems with one-bit ADCs," *IEEE Trans. Commun.*, vol. 64, no. 5, pp. 2005–2018, May 2016.

[181] C.-K. Wen, C.-J. Wang, S. Jin, K.-K. Wong, and P. Ting, "Bayes-optimal joint channel-and-data estimation for massive MIMO with low-precision ADCs," *IEEE Trans. Signal Process.*, vol. 64, no. 10, pp. 2541–2556, May 2016.

[182] S. Rao, A. Mezghani, and A. L. Swindlehurst, "Channel estimation in one-bit massive MIMO systems: Angular versus unstructured models," *IEEE J. Sel. Topics Signal Process.*, vol. 13, no. 5, pp. 1017–1031, Sep. 2019.

[183] J. Mo, P. Schniter, and R. W. Heath, "Channel estimation in broadband millimeter wave MIMO systems with few-bit ADCs," *IEEE Trans. Signal Process.*, vol. 66, no. 5, pp. 1141–1154, Mar. 2018.

[184] I. Atzeni and A. Tölli, "Channel estimation and data detection analysis of massive MIMO with 1-bit ADCs," *IEEE Trans. Wireless Commun.*, vol. 21, no. 6, pp. 3850–3867, Jun. 2022.

[185] M. Ding, I. Atzeni, A. Tölli, and A. L. Swindlehurst, "On optimal MMSE channel estimation for one-bit quantized MIMO systems," *IEEE Trans. Signal Process.*, vol. 73, pp. 617–632, 2025.

[186] Y.-S. Jeon, N. Lee, S. Hong, and R. W. Heath, "One-bit sphere decoding for uplink massive MIMO systems with one-bit ADCs," *IEEE Trans. Wireless Commun.*, vol. 17, no. 7, pp. 4509–4521, Jul. 2018.

[187] I. Atzeni and A. Tölli, "Uplink data detection analysis of 1-bit quantized massive MIMO," in *Proc. IEEE Int. Workshop Signal Process. Adv. Wireless Commun. (SPAWC)*, 2021, pp. 1–5.

[188] A. Radbord, I. Atzeni, and A. Tölli, "Multi-user data detection in massive MIMO with 1-bit ADCs," in *Proc. IEEE Int. Conf. Acoust. Speech Signal Process. (ICASSP)*, 2023, pp. 1–8.

[189] A. Radbord, I. Atzeni, and A. Tölli, "Enhanced data detection for massive MIMO with 1-bit ADCs," in *Proc. Asilomar Conf. Signals Syst. Comput. (ASILOMAR)*, 2023, pp. 427–432.

[190] A. Radbord, I. Atzeni, and A. Tölli. "Enhanced uplink data detection for massive MIMO with 1-bit ADCs: Analysis and joint detection." 2024. [Online]. Available: https://arxiv.org/pdf/2312.04183v2

[191] H. Jedda, A. Mezghani, A. L. Swindlehurst, and J. Nossek, "Quantized constant envelope precoding with PSK and QAM signaling," *IEEE Trans. Wireless Commun.*, vol. 17, no. 12, pp. 8022–8034, Dec. 2018.

[192] A. Saxena, A. Mezghani, and R. W. Heath, "Linear CE and 1-bit quantized precoding with optimized dithering," *IEEE Open J. Signal Process.*, vol. 1, pp. 310–325, 2020.

[193] A. Li, C. Masouros, A. L. Swindlehurst, and W. Yu, "1-bit massive MIMO transmission: Embracing interference with symbol-level precoding," *IEEE Commun. Mag.*, vol. 59, no. 5, pp. 121–127, May 2021.

[194] I. Atzeni, A. Tölli, D. H. N. Nguyen, and A. L. Swindlehurst, "Doubly 1-bit quantized massive MIMO," in *Proc. Asilomar Conf. Signals Syst. Comput. (ASILOMAR)*, 2023, p. 12.

[195] J. J. Bussgang, "Crosscorrelation functions of amplitude-distorted Gaussian signals," Res. Lab. Electron., Massachusetts Inst. Technol., Cambridge, MA, USA, Rep. 216, 1952.

[196] H. Farhadi, J. Haraldson, and M. Sundberg, "A deep learning receiver for non-linear transmitter," *IEEE Access*, vol. 11, pp. 2796–2803, 2023.

[197] H. Farhadi and M. Sundberg, "Machine learning empowered context-aware receiver for high-band transmission," in *Proc. IEEE Global Commun. Conf. (GLOBECOM)*, 2020, pp. 1–8.

[198] H. Farhadi et al., "AI-driven air interface: Hexa-X-II view," *IEEE Commun. Mag.*, early access.

[199] F. Liu et al., "Integrated sensing and communications: Toward dual-functional wireless networks for 6G and beyond," *IEEE J. Sel. Areas Commun.*, vol. 40, no. 6, pp. 1728–1767, Jun. 2022.

[200] H. Wymeersch and G. Seco-Granados, "Radio localization and sensing—Part I: Fundamentals," *IEEE Commun. Lett.*, vol. 26, no. 12, pp. 2816–2820, Dec. 2022.

[201] H. Wymeersch et al., "Joint communication and sensing for 6G—A cross-layer perspective," in *Proc. IEEE Int. Symp. Joint Commun. Sens. (JC&S)*, 2024, pp. 1–8.

[202] H. Sallouha, S. Saleh, S. D. Bast, Z. Cui, S. Pollin, and H. Wymeersch, "On the ground and in the sky: A tutorial on radio localization in ground-air-space networks," *IEEE Commun. Surveys Tuts.*, vol. 27, no. 1, pp. 218–258, Feb. 2025.

[203] H. Chen et al., "6G localization and sensing in the near field: Features, opportunities, and challenges," *IEEE Wireless Commun.*, vol. 31, no. 4, pp. 260–267, Aug. 2024.

[204] H. Lu et al., "A tutorial on near-field XL-MIMO communications towards 6G," *IEEE Commun. Surveys Tuts.*, vol. 26, no. 4, pp. 2213–2257, 4th Quart., 2024.

[205] M. Cui, L. Dai, Z. Wang, S. Zhou, and N. Ge, "Near-field rainbow: Wideband beam training for XL-MIMO," *IEEE Trans. Wireless Commun.*, vol. 22, no. 6, pp. 3899–3912, Jun. 2023.

[206] H. Chen et al., "Modeling and analysis of OFDM-based 5G/6G localization under hardware impairments," *IEEE Trans. Wireless Commun.*, vol. 23, no. 7, pp. 7319–7333, Jul. 2024.

[207] H. Sarieddeen, N. Saeed, T. Y. Al-Naffouri, and M.-S. Alouini, "Next generation terahertz communications: A rendezvous of sensing, imaging, and localization," *IEEE Commun. Mag.*, vol. 58, no. 5, pp. 69–75, May 2020.

[208] L. Daniel and M. Gashinova, "Sub-THz radar imagery for automotive application," in *Proc. Eur. Radar Conf. (EuRAD)*, 2022, pp. 1–8.

[209] G. Tzydynzhapov, P. Gusikhin, V. Muravev, A. Dremin, Y. Nefyodov, and I. Kukushkin, "New real-time sub-terahertz security body scanner," *J. Infrared Mil. Thz. Waves*, vol. 41, no. 1, pp. 632–641, 2020.

[210] A. Abina, U. Puc, M. Jazbinšek, and A. Zidanšek, "Analytical gas sensing in the terahertz spectral range," *Micromachines*, vol. 14, no. 11, p. 1987, 2023.

[211] A. Y. Owda, N. Salmon, A. J. Casson, and M. Owda, "The reflectance of human skin in the millimeter-wave band," *Sensors*, vol. 20, no. 5, p. 1480, 2020.

[212] A. Passarelli et al., "Terahertz-wave absorption gas sensing for dimethyl sulfoxide," *Appl. Sci.*, vol. 12, no. 11, p. 5729, 2022.

[213] A. Behravan et al., "Positioning and sensing in 6G: Gaps, challenges, and opportunities," *IEEE Veh. Technol. Mag.*, vol. 18, no. 1, pp. 40–48, Mar. 2023.

[214] O. Kanhere, H. Poddar, Y. Xing, D. Shakya, S. Ju, and T. S. Rappaport, "A power efficiency metric for comparing energy consumption in future wireless networks in the millimeter-wave and terahertz bands," *IEEE Wireless Commun.*, vol. 29, no. 6, pp. 56–63, Dec. 2022.

[215] H. Aghasi, A. Cathelin, and E. Afshari, "A 0.92-THz SiGe power radiator based on a nonlinear theory for harmonic generation," *IEEE J. Solid-State Circuits*, vol. 52, no. 2, pp. 406–422, Feb. 2017.

[216] *IEEE Standard for High Data Rate Wireless Multi-Media Networks—Amendment 2: 100 Gb/s Wireless Switched Point-to-Point Physical Layer*, IEEE Standard 802.15.3d-2017, 2017.

[217] C. Han, Y. Wu, Z. Chen, Y. Chen, and G. Wang, "THz ISAC: A physical-layer perspective of terahertz integrated sensing and communication," *IEEE Wireless Commun. Mag.*, vol. 62, no. 2, pp. 102–108, Feb. 2024.

[218] P. Zheng, T. Ballal, H. Chen, H. Wymeersch, and T. Y. Al-Naffouri, "Coverage analysis of joint localization and communication in THz systems with 3-D arrays," *IEEE Trans. Wireless Commun.*, vol. 23, no. 5, pp. 5232–5247, May 2024.

[219] J. M. Jornet, E. W. Knightly, and D. M. Mittleman, "Wireless communications sensing and security above 100 GHz," *Nat. Commun.*, vol. 14, no. 1, p. 841, 2023.

[220] V.-L. Nguyen, R.-H. Hwang, B.-C. Cheng, Y.-D. Lin, and T. Q. Duong, "Understanding privacy risks of high-accuracy radio positioning and sensing in wireless networks," *IEEE Commun. Mag.*, vol. 62, no. 5, pp. 104–111, May 2024.

[221] W. Hedhly, O. Amin, B. Shihada, and M.-S. Alouini, "A power saving scheme for IEEE 802.15.3d THz wireless communication links," *IEEE Trans. Mobile Comput.*, vol. 22, no. 4, pp. 1912–1921, Apr. 2023.

[222] C. Wei et al., "Accurate wideband channel estimation for THz massive MIMO systems," *IEEE Commun. Lett.*, vol. 27, no. 1, pp. 293–297, Jan. 2023.

[223] E. Vlachos, A. Kaushik, Y. C. Eldar, and G. C. Alexandropoulos. "Time-domain channel estimation for extremely large MIMO THz communication systems under dual-wideband fading conditions." 2024. [Online]. Available: https://arxiv.org/pdf/2310.14745

[224] A. Arjas and I. Atzeni. "Nonlinear sparse Bayesian learning methods with application to massive MIMO channel estimation with hardware impairments." 2025. [Online]. Available: https://arxiv.org/pdf/2506.03775

[225] M. Cui and L. Dai, "Channel estimation for extremely large-scale MIMO: Far-field or near-field?" *IEEE Trans. Wireless Commun.*, vol. 70, no. 4, pp. 2663–2677, Apr. 2022.

[226] I. Gavras, I. Atzeni, and G. C. Alexandropoulos, "Near-field localization with 1-bit quantized hybrid A/D reception," in *Proc. IEEE Int. Conf. Acoust. Speech Signal Process. (ICASSP)*, 2024, pp. 1–8.

[227] G. C. Alexandropoulos et al., "Reconfigurable intelligent surfaces for THz: Hardware design and signal processing challenges," in *Proc. Eur. Conf. Antennas Propag. (EuCAP)*, 2024, pp. 1–8.

[228] W. K. New et al., "A tutorial on fluid antenna system for 6G networks: Encompassing communication theory, optimization methods and hardware designs," *IEEE Commun. Surveys Tuts.*, early access, Nov. 15, 2024, doi: 10.1109/COMST.2024.3498855.

[229] L. Tlebaldiyeva, S. Arzykulov, K. M. Rabie, X. Li, and G. Nauryzbayev, "Outage performance of fluid antenna system (FAS)-aided terahertz communication networks," in *Proc. IEEE Int. Conf. Commun. (ICC)*, 2023, pp. 1–8.

[230] Z. Wan, Z. Gao, F. Gao, M. D. Renzo, and M.-S. Alouini, "Terahertz massive MIMO with holographic reconfigurable intelligent surfaces," *IEEE Trans. Commun.*, vol. 69, no. 7, pp. 4732–4750, Jul. 2021.

[231] R. Kumar and S. Arnon, "SNR optimization for LEO satellite at sub-THz frequencies," *IEEE Trans. Antennas Propag.*, vol. 70, no. 6, pp. 4449–4458, Jun. 2022.

[232] S. Nie and I. F. Akyildiz, "Channel modeling and analysis of inter-small-satellite links in terahertz band space networks," *IEEE Trans. Commun.*, vol. 69, no. 12, pp. 8585–8599, Dec. 2021.

[233] S. A. Torrens, V. Petrov, and J. M. Jornet, "Modeling interference from millimeter wave and terahertz bands cross-links in low Earth orbit satellite networks for 6G and beyond," *IEEE J. Sel. Areas Commun.*, vol. 42, no. 5, pp. 1371–1386, May 2024.

[234] J. Kokkoniemi, J. M. Jornet, V. Petrov, Y. Koucheryavy, and M. Juntti, "Channel modeling and performance analysis of airplane-satellite terahertz band communications," *IEEE Trans. Veh. Technol.*, vol. 70, no. 3, pp. 2047–2061, Mar. 2021.

[235] J. Kokkoniemi, "Stochastic analysis of THz band satellite channels' quality," in *Proc. Eur. Conf. Antennas Propag. (EuCAP)*, 2025, pp. 12–17.

[236] W. Gao, C. Han, X. Lu, and Z. Chen, "On multiple-antenna techniques for physical-layer range security in the terahertz band," *IEEE Open J. Commun. Soc.*, vol. 5, pp. 3089–3103, 2024.

[237] V. Petrov et al., "Physical layer security for terahertz communications in massive IoT," in *Security and Privacy for 6G Massive IoT*. Hoboken, NJ, USA: Wiley, 2025.

[238] J. Qiao and M.-S. Alouini, "Secure transmission for intelligent reflecting surface-assisted mmWave and terahertz systems," *IEEE Wireless Commun. Lett.*, vol. 9, no. 10, pp. 1743–1747, Oct. 2020.

[239] J. Qiao, C. Zhang, A. Dong, J. Bian, and M.-S. Alouini, "Securing intelligent reflecting surface assisted terahertz systems," *IEEE Trans. Veh. Technol.*, vol. 71, no. 8, pp. 8519–8533, Aug. 2022.

[240] Z. Zhang, Y. Liu, Z. Wang, X. Mu, and J. Chen, "Physical layer security in near-field communications," *IEEE Trans. Veh. Technol.*, vol. 73, no. 7, pp. 10761–10766, Jul. 2024.

[241] Z. Tang et al. "Low complexity artificial noise aided beam focusing design in near-field terahertz communications." 2025. [Online]. Available: https://arxiv.org/pdf/2502.08967

[242] D. Morales and J. M. Jornet, "ADAPT: An adaptive directional antenna protocol for medium access control in terahertz communication networks," *Ad Hoc Netw.*, vol. 119, Aug. 2021, Art. no. 102540.

[243] A.-A. A. Boulogeorgos et al. "Artificial intelligence empowered multiple access for ultra reliable and low latency THz wireless networks." 2022. [Online]. Available: https://arxiv.org/pdf/2208.08039